WIND AND TOPOGRAPHIC EFFECTS ON THE
LABRADOR CURRENT AT CARSON CANYON

ERIC DOUGLAS KINSELLA

WIND AND TOPOGRAPHIC EFFECTS ON THE

LABRADOR CURRENT AT CARSON CANYON

BY

© Eric Douglas Kinsella, B. Sc.

A Thesis submitted in partial fulfillment

of the requirements for the degree of

Master of Science

Department of Physics

Memorial University of Newfoundland

June 1984

St. John's   Newfoundland

ABSTRACT

Carson Canyon is located on the eastern slope of the Grand Bank and is about 40 km wide, 80 km long, and 700 m deep where it intersects the shelf break (110 m). Data from June of 1980 and 1981 are interpreted in terms of steady and time-dependent (wind-driven) interactions of the Labrador Current with the canyon. The mean velocity field is estimated from direct measurements and the dynamic topography relative to 200 dbar. Up and downstream of the canyon, the flow was predominantly along-isobath with speeds of O (20 cm s^{-1}) near the shelf break 10 m above bottom, and 48 cm s^{-1} at the velocity axis over the 500 m isobath. A 20 m thick cold core of $\leqslant$ -1 °C water upstream of the canyon separated into inner and outer cold cores over the canyon axis, and coalesced to reform a single core downstream. The degree to which the canyon perturbed the mean flow changed with position both along and perpendicular to the canyon axis with along-isobath flow near the shelf break; cross-isobath flow on the upstream side and cross-canyon flow in the center; further off-shelf, the flow remained undisturbed by the canyon. Divergence of the mean flow in the vicinity of a secondary head on the upstream side is indicated by the measurements, implying steady upwelling. This is supported by a 0.9 cm s^{-1} residual, near-bottom flow toward the secondary head. A single upwelling event lasting 5 d was observed following 18 - 23 m s^{-1} southwesterly winds of about 0.5 d duration. Current reversal at the shelf break occurred soon after the high speed winds ceased, followed by abrupt temperature (2.8 °C) and salinity (1.2 ppt) increases up to 1 d later. At 167 m depth in the central canyon region, isohalines rose at rates of 0.2 - 0.5 cm s^{-1}. The reversal was baroclinic: the Labrador Current continued to flow southwestward.

but with reduced speeds; and the reversal itself was confined to a layer centered at about 130 m depth. The reversal and decreased upper-layer speeds probably arise from the barotropic response to a wind-induced decrease in sea surface slope: the upwelling represents the slower baroclinic response. Steady upwelling in the presence of a shelf-break jet in the upper layer is modeled using a two-layer system and a vertical wall at the shelf break. The model results differ from the usual (no jet) case: upwelling is suppressed by 26% at the coast, but extends to greater distances offshore.

ACKNOWLEDGEMENTS

TABLE OF CONTENTS

LIST OF FIGURES

LIST OF TABLES

CHAPTER 1   INTRODUCTION

This thesis constitutes the first description and analysis of physical oceanographic data from any of the submarine canyons that indent the southeastern edge of the Grand Bank of Newfoundland.

An outstanding feature of the dynamics is the presence of the Labrador Current: a strong, shelf-edge jet which flows with shallow water to its right and which is also a western boundary current. This thesis addresses two important aspects of canyon dynamics in the eastern Grand Bank region: the effect of abrupt topography on the mean flow of the Labrador Current, and the effects of impulsive wind forcing on the local circulation and cross-slope material fluxes. These processes are expected to be important to problems related to biological production and environmental problems related to the oil industry.

1.1 Physical description of the study area

The Grand Banks of Newfoundland (Figure 1.1) extend southeastward more than 445 km from the island of Newfoundland. The Grand Bank covers an area of about 25×10^5 km^2, is on average only 60 m deep, and is the largest bank in the world. The Flemish Cap lies to the east of the Grand Bank and is separated from it by the Flemish Pass. Carson Canyon is the northernmost of the canyons at the southeastern edge of the Grand Bank.

The bathymetry in the vicinity of Carson Canyon is shown in Figure 1.2. Carson Canyon is a U-shaped upslope of the 732 m isobath when viewed in vertical cross-section, and is approximately 10 km wide.
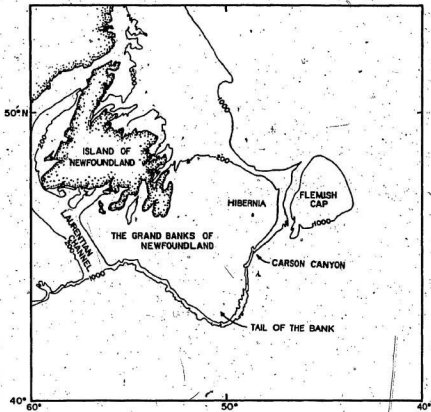
FIGURE 1.1: Location map showing Newfoundland the Grand Banks and Carson Canyon (depth in meters).
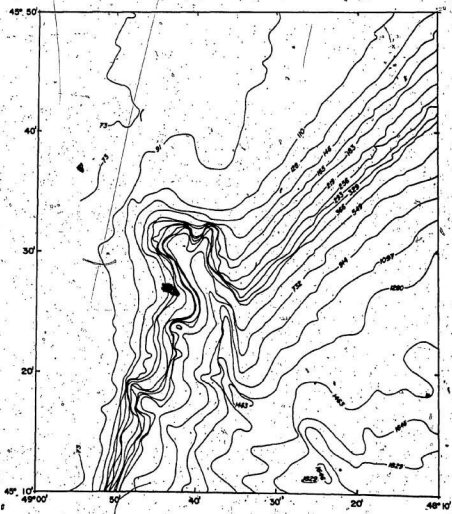
FIGURE 1.2: Detailed bathymetry of Carson Canyon (depth in meters).

The shelf break in the vicinity of Carson Canyon is identifiable as the 110 m isobath. The canyon head intrudes 20 km into the shelf. A distinctive feature is the presence of a "secondary head" on the northeast side of Carson Canyon.

1.2 Historical review

The eastern edge of the Grand Bank has been systematically surveyed by the U.S. Coast Guard since the sinking of the Titanic in 1912 as part of the International Ice Patrol (IIP) (e.g. Scobie, 1975). With few exceptions since 1913, stations have been occupied annually by the IIP during April and May along transects across the eastern margin of the Grand Bank.

In recognition of the significance of physical oceanographic processes to the fisheries on the Grand Bank, the Canadian government has supplemented the IIP transects since 1951 (in the months of June and July) as part of its contribution to ICNAF (International Commission for the Northwest Atlantic Fisheries). Russian fisheries oceanographers have also published reports on the data they have collected in the the Grand Bank area. The reader is referred to ICNAF Special Publication No. 10 (1975), Kudlo and Boystov (1978), and Kudlo, Burmakin and Sterkhov (1979) for summaries of the fisheries-related studies.

If the preeminence of the fishing industry could be said to be eclipsed in local current affairs, it would be due to the discovery of massive oil and natural gas reserves in the Hibernia field on the east side of the Bank (Figure 1.1). Hibernia is located on the shelf approximately 85 km due north of Carson Canyon. Existing physical oceanographic data for this region have been found inadequate to permit assessment of safety and

environmental factors. Data collected by the petroleum industry as part of their exploratory drilling operations are beginning to contribute to our understanding of the physical oceanography of this area as they become available in the public domain (e.g. Petrie, 1982; Petrie and Anderson, 1983).

1.2.1 Labrador Current studies

In this section, previous studies of the Labrador Current are reviewed with respect to the characteristics of the mean flow and its variability, with particular reference to possible wind-induced effects.

With regard to the mean flow, a pioneering study by Smith, Soule and Mosby (1937) established that the Labrador Current originates at the northern extremity of the Labrador shelf and is characterized by low temperatures (< 2 °C) and low salinities (< 34.3 ppt). An offshore branch passes over Carson Canyon as it flows southwards along the eastern margin of the Grand Bank, an inshore branch runs along the Newfoundland coast (Figure 1.1). From this point on, the term "Labrador Current" will refer only to the offshore branch unless otherwise stated.

The speed of the Labrador Current at the southeastern edge of the Grand Bank based on geostrophic calculations has been estimated to be about 30 cm s^{-1} (e.g. Hill, Jones, Ramster and Folkard, 1973). Hill et al. (1973) also report that the high speed core (> 20 cm s^{-1}) is about 30 km wide. In a recent summary of Grand Banks physical oceanography, Petrie and Anderson (1983) give 4.1×10^6 m^3 s^{-1} as the mean geostrophic transport of the offshore branch and a mean speed range of 20 to 60 m s^{-1} relative to 1000 dbar. A trend towards increased speeds during late spring and early summer has been observed by direct current

measurements (Hayes, 1984; Mountain, 1980), in apparent contradiction of observations of a decrease in the geostrophic mass transport over the same season (Hayes, 1984).

A current meter study was undertaken by Robe (1975), to test the validity of the 1000 m depth of zero motion assumption (used by the IIP since its inception) to compute geostrophic velocities. Two moorings, each with a single current meter 40 m above bottom, were deployed close to the 1000 m isobath; the first in April - May on the mid-eastern slope of the Grand Bank, and the second in May - June to the southeast. The flows at both meters are reported to be strongly rectified in the along-slope direction and an ≈ 5 cm s^{-1} southwestward residual drift was observed in both cases. It was concluded that the geostrophic values underestimate the speed by 10-30%.

Mountain (1980) presents results from a single mooring deployed in April-June, 190 km southwest of Carson Canyon on the southeastern slope at a depth of 490 m, with current meters at 110 m and 380 m. Mean speeds of 46 cm s^{-1} and 18 cm s^{-1} were reported for the upper and lower current meters respectively. The direction was toward the south, and there was a marked rectification of currents parallel to the isobaths intensifying with depth. Hill et al. (1973) discuss results from three current meters at unspecified depths on a single mooring in the Flemish Pass positioned on the west side of the velocity core of the Labrador Current in April. The current meter mooring was near the shelf break (bottom depth ≈130 m) and a residual southwestward (along-slope) flow of 18 cm s^{-1} was measured by all three current meters.

Several studies have discussed the variability of the Labrador Current. Hill et al. (1973) report a "sudden" reversal to a northeastward, 6 cm s^{-1}

drift which persisted to the end of the current meter record, a 5 day period. It was suggested that the observed flow reversal was likely due to an eastward shift in the position of the Labrador Current velocity core. The reversal occurred 4 days after a period of gale-force southeasterly winds.

Both wind stress and actual displacement of the position of the velocity core have also been proposed as being responsible for certain variations in the Labrador Current by Seaconsult (1978). A mooring positioned in the northern end of Flemish Pass at about 1000 m depth for 3 months, starting in mid-April, was recovered and then immediately redeployed for another 3 months at the southern end, also at about 1000 m depth. Based on current meter data collected from the four meters on the southern mooring (at depths of 168, 481, 781 and 961 m), it was suggested that meandering of the Labrador Current velocity core caused variations in the records, including variations that would otherwise appear to be a spring/summer seasonal change in the properties of the current. The records from the three current meters on the northern mooring (at depths of 467, 767, and 927 m) indicated reversed northeastward flow during the first 4 - 5 d segment of the data, followed by persistent southward flow. The northeastward flow was related to a series of low pressure storms centered to the northwest that caused strong (e.g. 18 m s^{-1}) along-shelf, southwesterly winds. Hayes (1984) combined geostrophic velocities derived from CTD (conductivity-temperature-depth profiler) data with the same current meter records. The region of reversed flow was shown to lie between two southward flowing branches of a "bifurcated" Labrador Current.

Hayes (1984) also suggested that baroclinically unstable waves cause

the > 2.5 d period, peak energy signals in the current meter spectra. The coherency between the velocity field and the wind stress calculated from the Fleet Numerical Oceanographic Central, Monterey California 12-hourly analysis wind field was examined. The only significant coherency was that between the north-south wind stress and the north-south velocity components in the spring for the current meter at 500 m for the 8 - 25 d band. The coherency peaked for a 15 d period and zero phase shift. The presence of significant energy at the inertial period suggested "the possibility of some mechanism for impulse storm forcing." (Hayes 1984, p. 9)

Mountain (1980) found that a low-frequency signal of 10 to 16 d period in the along-slope component at both 110 and 380 m was coherent with the along shelf wind stress (derived from 12-hourly wind values supplied by the U. S. Navy Fleet Numerical Weather Central). Maximum energies for the along-slope velocity and wind stress records were reported to lie in the 10-16 d band. The along-shelf, low frequency response of the instrument at 110 m lagged the wind stress by approximately one day and the lag was about two days for the current meter at 380 m. A 2 - 4 d periodicity was reported for the cross-stream component of velocity at both meters with the strongest signal at the upper meter. No current reversals were indicated by either meter, but near zero velocities were recorded by the lower meter on two separate occasions in April. Furthermore, the onset of reduced velocities often appeared to occur at, or subsequent to, times of maximum upstream wind stress.

Robe (1975) observed that the residual flow reversed direction towards the northeast with a speed of 1 cm s^{-1} for a period of 1 d at the northeastern mooring and with a speed of 2 cm s^{-1} for a 5 d period at

the southern mooring. It was reported that "no clear relationship" existed between the low frequency fluctuations and the surface wind field at either location.

Wind-driven currents on the Grand Bank may be substantial. Petrie (1982) discusses data from moorings situated on the shelf at the Hibernia site (Figure 1.1). Annual mean currents at Hibernia were estimated to be negligible. Current directions are evenly distributed around the entire compass. On the other hand, maximum residual currents in 1980, which were low-pass filtered to remove signals of periods < 1.9 d, reach 70 cm s^{-1} at mid-depths and 30 cm s^{-1} one-half meter off bottom, and were found to be correlated with the geostrophic wind. The interaction of strong wind-induced shelf currents with the Labrador Current, as opposed to the direct effects of wind on the Current itself, may be important, but has yet to be modeled.

1.2.2 Canyon studies

A particularly informative review of the recent literature on canyon dynamics is given by Huthnance (1981); see also Inman, Nordstrom and Flick (1976). Typically, one can expect to find significant up- and down-canyon motion, which is often perpendicular to the shelf break, even when the mean flow is along the shelf. Research into the circulation of shelves indented by canyons consistently indicates that canyons provide preferential and localized sources of intermediate depth water for the inner shelf. This upwelling can occur as a result of the effects of canyon topography on the mean circulation, or on wind or long period wave induced motion.

Freeland and Denman (1982) have shown that steady, topographically controlled upwelling at Spur Canyon off Vancouver Island is driven by an along-canyon pressure gradient associated with the geostrophic flow above the canyon. Mayer, Han and Hansen (1982) have determined that the pressure gradient due to the sea surface slope driving the geostrophic flow above the Hudson Shelf Valley is balanced by the pressure gradient associated with the density field at a level within the canyon called a 'horizon'. Below the horizon, the density variation results in a net pressure gradient which drives an along-axis, up-valley flow. Cannon (1972) reports the same phenomenon occurs within the Juan de Fuca Canyon off Vancouver Island. Seaward flow at the surface drives estuarine-like, shelfward currents in the submarine canyons of the Eurasian Basin according to Coachman and Barnes (1962).

Wang (1980) discusses a theoretical model for localized upwelling caused by the scattering of large scale continental shelf waves by a canyon in the near-shore region.

Amplified, wind-induced upwelling, was observed by Shaffer (1976) near a narrow, O(10 km) wide canyon off northwest Africa. Results from that area will be commented upon in further detail when an upwelling model for the Carson Canyon area is presented. Cannon (1972) suggests that strong along-slope wind stresses cause along-axis currents below the main thermocline in the Juan de Fuca Canyon. Mayer et al. (1982) have synthesized results by Hsueh (1980) and others to show how a wind-induced reversal (to a northeastward flow) of the mean current at the Hudson Shelf Valley is modified by friction so that up-valley flow develops parallel to the valley axis. Consistent with this result, Mayer, Moffeld and Leaman (1981) found signs of localized upwelling in the Hudson Shelf Val-

ley due to the occurrence of Hurricane Belle; currents within the canyon were shoreward and parallel to the valley axis. Localized upwelling on the equatorward side of a mesoscale canyon was found in a two-layer numerical model by Peffley and O'Brien (1976). These authors report that the model results are consistent with observations taken off the Oregon coast and that upwelling over the canyon persisted for at least 2.5 d after the upwelling-favorable wind stress stopped. An analytic solution was found by Killworth (1978) for the problem of the influence of stratification, and gradual along-shore variations of a vertical coastline over a flat bottom, on impulsive wind-forced upwelling. It was speculated that a fully three-dimensional upwelling/downwelling regime would leave residual upwelling on the equatorward side of a canyon. The effects due to the continental slope were not determined, and Killworth suggests that the solution to the upwelling problem for small cross-canyon scales (typically $\sim$ 10 km, which, by Figure 1.2, is about the same as that of Carson Canyon) is probably intractable analytically.

Studies of internal wave dynamics in Hudson Canyon by Gordon (1982), and by Hotchkiss and Wunsch (1982), and in a non-rotating experimental setup by Baines (1983) have shown that canyons trap internal gravity waves. Internal waves may have amplitudes several times those existing nearby but outside the canyon. The opposite may hold for baroclinic inertial oscillations. Mayer et al. (1981), while describing the presence of large amplitude inertial, baroclinic signals generated during the passage of Hurricane Belle in current meter records from the New England shelf, observed that, except near the surface, there was a negligible inertial signal registered by current meters at the same depths within the Hudson Shelf Valley.

1.3 Organization of the thesis

The thesis is organized into 7 chapters. This introduction forms the first chapter. Chapter 2 is a summary of the data sources and data processing methodology. The 1980 and 1981 data are presented in Chapters 3 and 4 respectively. The fifth chapter consists of a synthesis and interpretation of the data in terms of the steady-state dynamics at Carson Canyon. Wind-induced upwelling in the presence of the laterally-sheared Labrador Current is discussed in Chapter 6. The seventh chapter gives a summary and the conclusions of the thesis.

CHAPTER 2   DATA SOURCES AND METHODS

2.1 Field programs

Two research cruises to Carson Canyon were undertaken, one in June 1980 on GADUS ATLANTICA and a second in June 1981 on PANDORA II. Each cruise involved CTD surveys and deployment and recovery of moored current meters.

Time-series of temperature, salinity, current direction and speed, and, in certain cases, pressure, were obtained from the current meters. The CTD casts provided vertical profiles of temperature and salinity to a maximum depth of 500 m. Salinity for both the CTD's and the current meters was calculated by the formula given by Bennett (1976). Meteorological data and tidal height constituents were available from the drilling rigs at Hibernia (Figure 1.1). Surface pressure charts were used to analyze a storm which occurred over the Grand Bank in June of 1981. All of the software for current meter and CTD data analysis was developed as part of this thesis.

2.2 Processing of current meter records

Only Aanderaa RCM4 current meters were used in the field programs. Table 2.1 gives the manufacturer's specifications for these instruments.

Translation of the Aanderaa binary encoded current meter tapes onto 9 track magnetic tape in physical units was performed at the Bedford Institute of Oceanography (BIO). A first edit of the data was made at the time of translation at BIO. Standard deviations were calculated for the direction, rate, temperature and salinity records. BIO defined "bad"

records as those which were excessive in standard deviation: such records were "flagged" with a specific code. Flagged data were replaced by values which were calculated by averaging the two nearest neighbors.

TABLE 2.1 Aanderaa RCM4 current meter specifications

SENSOR	RANGE	ACCURACY	RESOLUTION	UNITS
Speed	2.5 to 250	2% or 1	Threshold 2.0	$cm\ s^{-1}$
Temp	-2.46 to 21.48	0.1	0.01	$°C$
Cond	0 to 77	0.2	0.07	$k\Omega^{-1}\ cm^{-1}$
Dir	1-360	5 to 7.5	0.35	degrees
Pres	0-650	6.5	0.65	dbar

1 dbar = 10 kPa.

After receipt of the data from BIO, magnetic deviation was added to the values of direction. The correction was +24.333 °T for the 1980 data and +23.5 °T for the 1981 data. The magnetic variation at Carson Canyon was derived by linear interpolation of isogonic lines from the Magnetic Variation Chart for the North Atlantic and Annual Rates of Change (British Navy) for epoch 1980.0.

In deriving velocity components from the current data, two coordinate systems were used. One system used only in figures of Appendices A and B, was aligned in terms of "U" and "V" components with U positive eastward and V positive northward. The second was formed by alignment with the bathymetry specific to each mooring location: the "u" component is positive pointing downstream along the isobath and the "i" component is then always positive in the local upslope direction.

2.2.1   Despiking

Editing of the current meter data was performed in 5 steps:

(1) "Differenced" time-series were created by subtracting a point from the next point in the sequence.

(2) Questionable values of the differenced series were identified as being among the 10% of the points with the highest standard deviations. As a further check, the programs used to perform this technique also rated the questionable values in terms of the sign of the value with respect to neighboring points. The extremum whose sign is opposite to that of both its neighbors is probably an isolated spike and is tentatively classified as "bad". The remainder are considered "suspect" to varying degrees.

(3) All questionable values were marked on printouts which listed all the records for each instrument. An attempt then was made to identify visually any patterns in the occurrence of questionable points. This identification was performed for patterns within a given time-series and for patterns among other time-series for each of the instruments. In several instances, an instrument would have a grouping of bad points for more than one parameter within the space of a few cycles. In these cases, many of the less suspect points were found to be present nearby as well. Such groupings were considered to be real, possibly the result of internal wave activity.

(4) Scatter plots of temperature & salinity, U & V and I & J component pairs also were employed to identify suspect values. Correlation between the points deemed to be bad or suspect using both methods was excellent.

(5) A visual inspection of the graph of each time-series was made. Bad points, it was perceived, consistently appeared as isolated spikes. Finally, bad values were replaced by the average of the two closest points.

In total, less than 0.5% of all the data recorded for any instrument were replaced.

2.2.2 Filtering

Low-pass filtering was applied to the temperature, salinity, U, V, I and J components of the despiked current meter records using moving average filters (Godin 1972, pp. 60-69) The first filter type employed on the despiked current meter data is called here the "first low-pass" (FLP) filter. A single filter is applied as three successive moving averages; in blocks of 6, 6 and 7 data points for the 1981 FLP filter and of 15, 15 and 17 points for the 1980 FLP filter. Different filters are required because of the change in the sample interval from 2 minutes in 1980 to 5 minutes in 1981. These FLP filters are symbolized (Godin 1972, p. 62) as $A_6 A_6 A_7$ and $A_{15} A_{15} A_{17}$ for the 1981 and 1980 cases respectively. Low-pass filtering reduces the variance of the time-series, and reduces the contribution by short period fluctuations to zero as long as the short period fluctuations sum to zero over the block of data being averaged. This demonstrates one reason why special care was taken to despike the data during editing because individual spikes bias the mean value of the slowly varying (i.e. low-passed) signal. The filter $A_n A_n A_{n+1}$ corresponds to a gain function (Godin 1972, p. 62):

$$\frac{1}{n^2(n+1)} \left[\frac{\sin^2(n\pi\sigma\Delta t)\sin((n+1)\pi\sigma\Delta t)}{\sin^3(\pi\sigma\Delta t)} \right]$$

multiplied into the spectrum of the record, where σ is the frequency and Δt is the sample period. The spectrum is reduced to zero for periods less than the "cut-off" period $(n \Delta t)$ determined by the operator with the smallest subscript, n. The period corresponding to the cut-off period for the FLP filters of 1980 (2 minute sample period) and 1981 (5 minute sample period) is then 30 minutes. Because the gain function is not perfectly sharp, there exists an "effective cut-off" period where the spectrum is reduced to $< .1\%$ of its initial value. The gains of the FLP operators $(A_6 A_6 A_7$ for 1981 and $A_{15} A_{15} A_{17}$ for 1980) are both 0.7% at the same effective cut-off period of 38 minutes. The FLP filter eliminates high frequency "noise" that may arise from internal waves.

A "second low-passed" (SLP) series was created by decimating the FLP series to a half hour sample period (by taking every 6th point in the smoothed records of 1981 and every 15th point for 1980) and then applying the $A_{24} A_{24} A_{25}$ set of moving averages. The cut-off period $(=24 \Delta t)$ is 12 hours. The effective cut-off period for the SLP filter with a half-hour sampling rate is 14.3 hours at which point the spectrum is reduced to 0.5% of its original value. Therefore the SLP filter eliminates the semidiurnal tide.

A "band-passed" (BP) series was created by subtracting the SLP series from the FLP series. The low and high effective cut-off periods then are respectively the same as the FLP (38 minutes) and SLP (14.3 hours) effective cut-off periods. Of course the FLP series first must be decimated to a half hour sample period and points removed from the beginning and end of the remainder so that the set of smoothed series are properly aligned before the BP series can be computed.

These low-pass filters are non-ideal in that significant attenuation

occurs at periods greater than the cut-off period. (see for example Walters and Heston (1982) for a comparison of the moving average with various other filters). Note that the -3 dB points (gain = 0.5) occur at 7.00×10^{-1} and 3.01×10^{-2} cph for the FLP and SLP filter respectively. Table 2.2. presents a list of the gain functions at selected frequencies.

TABLE 2.2 Gains of the filters used in this thesis

LABEL	FREQUENCY (cph)	$A_6^2 A_7$	$A_{15}^2 A_{17}$	$A_{24}^2 A_{25}$
M_2	8.05×10^{-2}	0.991	0.991	7.84×10^{-6}
Inertial	5.96×10^{-2}	0.995	0.995	3.72×10^{-2}
O_1	3.87×10^{-2}	0.998	0.998	3.05×10^{-1}
2 Day	2.08×10^{-2}	0.999	0.999	7.23×10^{-1}

2.2.3 Kinetic energy spectra

The despiked, unfiltered I and J component series were used to obtain the spectra. Kinetic energy (KE) spectra were formed by adding the spectral densities computed from the two components. Prior to computing the spectra, each set of I and J component time-series were truncated at 4096 points. After removing the average from each time-series, those with less than 4096 points were padded with zeros evenly to the beginning and end until each series was 4096 points long. The maximum proportion of zeros added was 13%. Then the Hanning window (Kanasewich, 1975) was applied to taper the endpoints and reduce side-

band leakage. Spectra were calculated via the fast Fourier transform using the program "SPECTRA" from the "Statistical Analysis System" (SAS) library. The spectral densities were corrected by dividing by a factor of 0.75 which is the ratio of the variance of the original data to that of the windowed data as given by

$$\lim_{\tau \to \infty} \frac{2}{\tau} \int_0^{\tau} \left[\frac{1}{2} + \frac{1}{2}\cos\frac{\pi t}{\tau} \right]^2 dt = 2 \times \frac{3}{8} = 0.75,$$

where τ is the period of the time-series (the factor of two in front of the integral arises because of the symmetry of the window). The corrected spectral densities of the I and J components for each instrument were then added together to form a KE spectrum.

2.3 Processing meteorological and tidal data

Wind and tidal data for 1980 and 1981 were obtained from drilling rigs stationed at Hibernia. Tidal height projections for Hibernia were performed at BIO.

The wind data were decomposed into northeasterly and southeasterly components aligned with the upstream shelf break orientation (45°T). The positive A (along-slope) component is the component of the wind which blows from the 45°T direction (northeasterly). The positive C (northwesterly) component is aligned 90° to the left of A.

Wind speed and direction records were edited by visual inspection of the data plots. Large, isolated spikes invariably were traced to obvious encoding errors. The anemometer used to obtain the 1980 records was 80 m above sea level. In 1981 the anemometer was positioned 76 m above sea level. Gill (1982, p. 29) supplies an example of wind speed

variation with height which shows a decrease in the speed at 80 m to that at the sea surface by a factor of 1.9. However, other factors, especially the stability of the air, are important in estimating wind speed and direction at the sea surface. Lacking a suitable technique for the calculation of the wind stress at Carson Canyon, a qualitative analysis of the geostrophic wind was performed on eight surface pressure charts (included in this thesis) from the Atmospheric Environment Service for June, 1981. These charts were also compared with surface pressure charts for the same period supplied by Nordco Ltd. of St. John's, Newfoundland.

2.4 Processing of CTD data

Table 2.3 gives the manufacturers' specifications for the CTD's used in the surveys of Carson Canyon. The 1980 CTD data were obtained using a Guildline Model 8707 Mk IV CTD. (see Table 2.3). Data were stored on cassettes and processed with a Hewlett-Packard 9825A Calculator. Salinity and density were computed using the Bennett (1976) formula. Bottle and thermometer data for salinity and temperature calibration checks were not available. Editing of the data was not feasible given the limitations imposed by the computer storage and hardware configurations.

Table 2.3 gives specifications for the Neil Brown Instruments Systems Mark IIIB CTD employed for the 1981 survey. DeYoung (1983) discusses the calibration data for this CTD for the same period. Maximum calibration errors are reported for salinity and temperature, which are respectively: 0.0011 ppt, 0.008 °C for the mean errors, and 0.012 ppt, 0.023 °C for the standard deviations. (Partly because no significant sensor drift was discovered during a factory calibration in 1982, the large values for the standard deviations are thought to be due to the calibration

technique. and not instrument error.) During a first pass through the data, a computer analysis package written in BASIC for the MINC 11/03 computer system automatically deleted all records that had a temperature < -2.0 °C or possessed pressure values lower than the preceding ones during the downcast. In this way the worst digitization errors and untrustworthy values (primarily caused by the research ship's roll) were immediately removed. The data were plotted (as temperature, salinity and density profiles) and spikes identified visually. Records considered bad were removed via screen editing of the data listings. This latter process was performed iteratively until the data were considered clean. All temperature, salinity and density sections were interpreted from data listings and contoured by hand. Temperature and salinity profiles were plotted by the MINC computer.

TABLE 2.3: Neil Brown MK IIIB (1981). (N.B.), and Guildline 8707. MK IV (1980). (GUILD). CTD specifications

INSTR	SENSOR	RANGE	ACCURACY	RESOLUTION	UNITS
N.B.	Pres	0-1600	0.8	0.024	dbar[†]
N.B.	Temp	-32 to 32	0.005	0.0005	°C
N.B.	Cond	1 to 65	0.005	0.001	$k\Omega^{-1} cm^{-1}$
GUILD	Pres	0-500	0.5	0.16	dbar[†]
GUILD	Temp	-2 to 30	0.005	0.0005	°C
GUILD	Sal	0.1 to 40	0.005	0.001	ppt

* Salinity is the conductivity ratio expressed in Equivalent Salinity - Accuracy specified includes linearity, resolution, repeatability and calibration uncertainty relative to standard seawater.

[†] 1 dbar = 10 kPa.

2.5 Dynamic height calculations

σ_t (sigma-t) values were used to calculate the dynamic topography of the 5 dbar surface with respect to 200 dbar. Using σ_t values here is considered to be acceptable since the effect of pressure on density in calculating the dynamic height incurs a relative error of only about 0.3% in the upper 200 meters (based on CTD data from Carson Canyon using standard tables from Knauss, 1978). It was necessary to compute the dynamic topography of the 5 dbar surface because CTD data were not recorded shallower than 5 m at some stations.

The level of no motion is assumed to be 200 m. This level was chosen for three reasons. One is for purposes of comparison with the results obtained by others in this area (e.g. Forrester and Benoit 1981, and Kudlo et al. 1979). Secondly, current meters used to study the Labrador Current substantiate the observation from IIP geostrophic calculations that the baroclinic, high speed velocity core of the Labrador Current is restricted to the top 200 m of the water column (Seaconsult, 1978). As well, Hayes (1984) states that the Labrador Current velocity core ($<$ 200 m depth) is "decoupled" from barotropic currents below because of incoherency between spectra computed from current meter time-series. Lastly, if a level of no motion had been chosen much deeper than 200 m, then more extensive extrapolation of the dynamic topography into shallower regions would have been necessary. Estimates for casts shallower than 200 m were made using the method of Reid and Mantyla (1976). Dynamic height was calculated to the maximum depth available and then added to the result extrapolated at the same depth from the two nearest in line and downslope neighbors. Some bias in the dynamic topography over

depths less than 200 m may exist because of uncertainties due to the application of the extrapolation technique. Another possible source of bias in the determination of dynamic topography which may be significant is that of positioning error.

2.6 Navigation

The accuracy of the dual-channel SATNAV system used for navigation on GADUS ATLANTICA in 1980 is discussed by Stansell (1976). An estimate for the accumulated error expected under normal circumstances for navigation by SATNAV on the Grand Bank is about 1-2 km. The cruise log for 1980 occasionally included addenda of changes in the ship's location during, or just following, a satellite update. A change in recorded position of 1.5 km was indicated in one case. Navigation in 1981 on PANDORA II was performed with Loran C, Decca and acoustic soundings of the bottom topography. Positions obtained in 1981 may be nearly as accurate as those of 1980 simply because, in 1981, much effort was taken to align the ship with the distinctive bathymetry of Carson Canyon. Nevertheless, positioning error due to navigation by bathymetry is difficult to evaluate, but clearly depends critically on the accuracy of the original bathymetric survey. The spacing of measurements on the hydrographic survey chart is ~2 km, which suggests possible errors of the order of 1 km. It is interesting to note in this respect that Shaffer (1976) reports an accuracy of ± 500 m off northwest Africa using only a bathymetric chart concurrently with acoustic soundings and the ship's speed and heading.

CHAPTER 3   1980 DATA

Current meter mooring and CTD positions for the 1980 cruise to Carson Canyon are shown in Figure 3.1. The moorings were located to the southwest (80-1) and northwest (80-2) of the canyon. The mooring information is listed in Table 3.1. Plots of those data which are discussed in the text are presented within this chapter; additional plots which are not discussed in detail may be found in Appendix A.

TABLE 3.1: 1980 Mooring Information

Mooring	80-1	80-2
Instrument	southwestern	northeastern
Instrument depth	120 m	164 m
Bottom depth	128 m	174 m
N. Latitude	45° 23.3′	45° 30.5′
W. Longitude	48° 46.6′	48° 38.1′
Deployed (GMT/date)	1430/1 June	2134/1 June
Recovered (GMT/date)	1818/6 June	1046/8 June
Sampling interval	2 min	2 min
Orientation	190 °T	225 °T
Comment	no salinity	no temperature and no salinity

↑ The orientation is the angle of the isobath at a given mooring in the downstream (v component of velocity) direction.
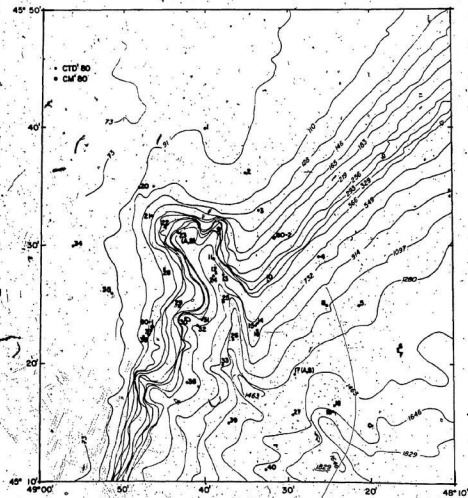
FIGURE 3.1: Current meter mooring (open circles) and CTD station (solid circles) locations for 1980 at Carson Canyon (depth in meters).

3.1   1980 Current meter records

Graphs of the FLP (first low-passed) and SLP (second low-passed) time-series of the I (cross-isobath) and J (along-isobath) components of velocity for the 1980 current meter data are given in Figures 3.2 and 3.3. Comparison of the two figures shows that the major source of variance is the semi-diurnal tide. This is also seen to be the case in the FLP and BP (band-passed) filtered temperature data from the southwestern current meter plotted in Figure 3.4 (the temperature sensor on the northeastern meter failed shortly after deployment). A 3 - 4 d period variation is also visually identifiable in the SLP series for the J component of both instruments. No current reversals are observed in the records for the along-shelf components.

Petrie (1982) compared the variability of the current regime on and off the shelf, by considering the ratio of the mean to the standard deviation of measured speeds filtered to remove the diurnal and semi-diurnal tide. Using Hibernia data, Petrie obtained ratios of 0.08 for meters at less than 100 m. and 0.53 for instruments between 100 and 200 m. Comparing these to the ratio of 4.7 as reported by Mountain (1980) for a current meter at 110 m depth, Petrie (1982) (and later, Petrie and Anderson, 1983) concluded that the mean flow dominates the dynamics on the eastern slope of the Grand Bank, but that the dynamics on the Bank are dominated by fluctuations, which probably are meteorologically forced. According to Muthence (1981, p.202), this result for the shelf regime is generally true for wide shelves at distances > 10 km from the shelf break. At Carson Canyon the SLP statistics in Table A1 of Appendix A yield ratios of 3.99 for the northeastern meter (mooring 80-2) and 3.88 for the southwestern meter (mooring 80-1). These values indicate that at the
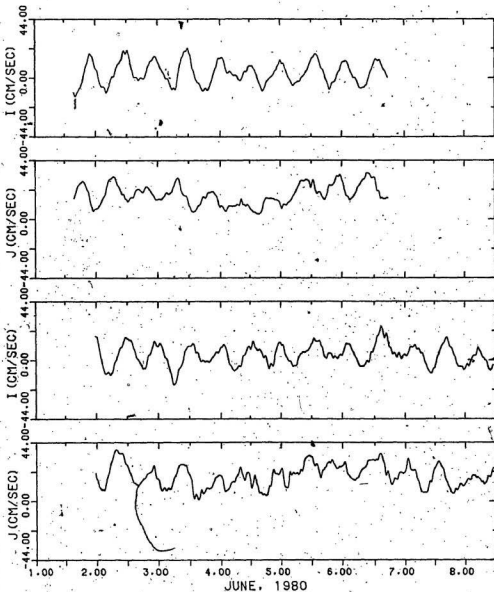
FIGURE 3.2: FLP time-series of the I and J components of velocity for the 1980 southwestern meter (mooring 80-1) -(top) and the 1980 northeastern meter (mooring 80-2) -(bottom)
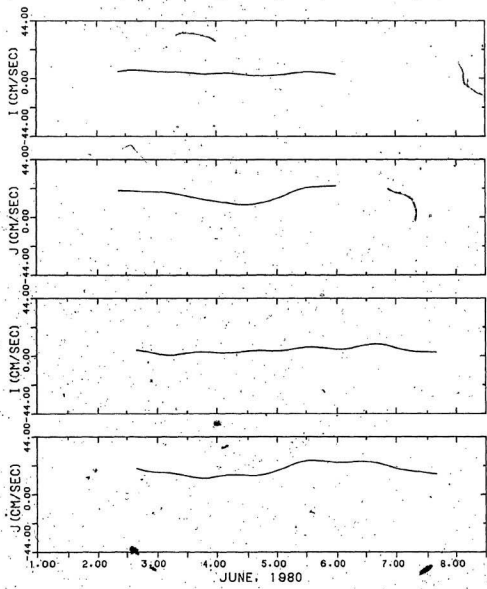
FIGURE 3.3: SLP time-series of the I and J components of velocity for the 1980 southwestern meter (mooring 80-1) -(top) and the 1980 northeastern meter (mooring 80-2) -(bottom)
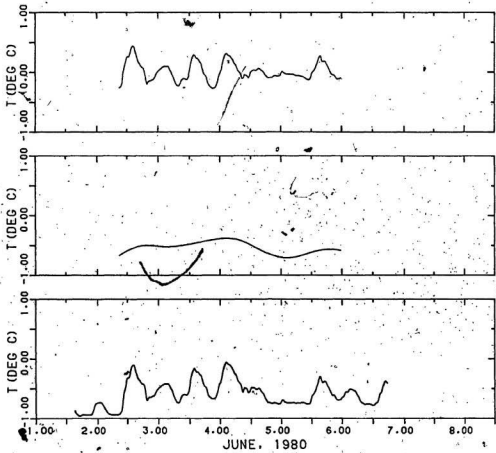
FIGURE 3.4: FLP (bottom), SLP (middle) and BP (top) time-series of temperature for the 1980 southwestern meter

time of these measurements, the mean flow of the Labrador Current should dominate the dynamics at the shelf break near Carson Canyon.

FLP filtered progressive vector diagrams (PVD's) for both 1980 current meters are presented in Figure 3.5. A semi-diurnal tide superposed on a predominant mean flow is evident in these plots. The means of the residual (SLP filtered) velocities at each of the two current meter moorings are presented in Figure 3.6. Although the residual flow is predominantly along-isobath, it is seen that there exists a significant up-slope component of velocity at both sites. Estimates for the magnitude of the deflection are similar: 13.0° for the northeastern meter and 14.0° for the southwestern meter. From Figure 3.6, it can be seen that if the mooring positions are translated by distances ≤ 2 km in each case, then it is possible to infer along-isobath flow at both locations. The 2 km spacing between the sounding lines from which the bathymetric map was drawn introduces uncertainty in the direction of the isobaths at kilometer scales, which together with possible current meter compass errors (Keenan, 1979 and 1981) and navigational uncertainties, suggest that the mean flow could in fact be in the direction of the isobaths. Nevertheless, the fact that upslope residuals were observed at both locations indicates that the effect may be real.

3.2 1980 Kinetic energy spectra

This section may be omitted at a first reading, since the results of the spectral analysis are not essential to further discussion, but are included for completeness.
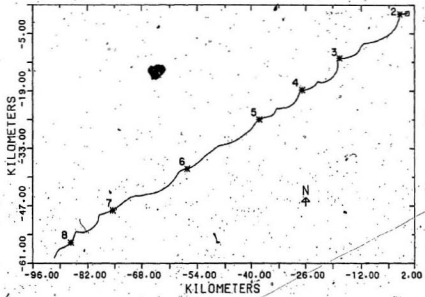
FIGURE 3.5: FLP PVD's for the 1980 northeastern (top) and southwestern (bottom) current meters
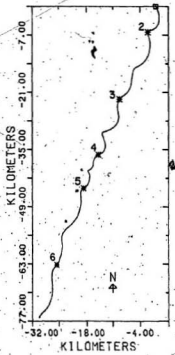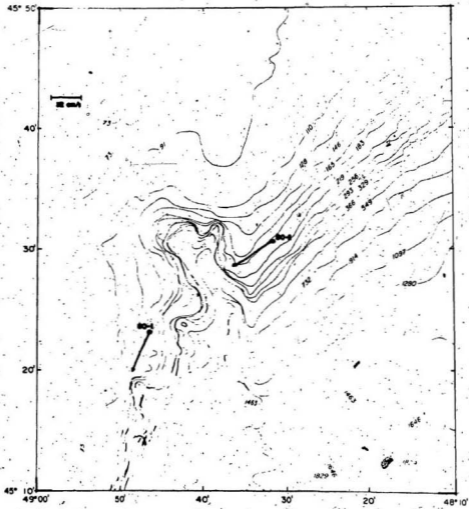
FIGURE 3.6: Mean (SLP) velocity vectors for 1980 at Carson Canyon (depth in meters).

Plots of kinetic energy spectra are presented in Figure 3.7. The strongest peak in both spectra may be seen at the M_2 (semi-diurnal) tidal frequency (8.05×10^{-2} cph). The energy spectral density at the semi-diurnal frequency for the southwestern meter at mooring 80-1 is 89×10^3 cm^2 s^{-2} cph^{-1}, and it is 66×10^3 cm^2 s^{-2} cph^{-1} for the northeastern meter at mooring 80-2. In the spectra for the southwestern meter (Figure 3.7a), there is a subsidiary, but statistically nonsignificant peak (90% confidence) corresponding to a frequency of 5.58×10^{-2} cph, which is close to the local inertial frequency (5.96×10^{-2} cph). The energy spectral density at the O_1 (diurnal) tidal frequency (3.87×10^{-2} cph), corresponds to a minimum in the spectrum of the southwestern meter. The second highest peaks visible in the spectra are for the frequencies lower than 1.35×10^{-2} cph in both cases. Unlike the situation described for the southwestern meter, there exists a distinct minimum in the spectrum (Figure 3.7b) of the northeastern meter at the inertial frequency. Also different is the existence of a broad peak in the spectrum of the northeastern meter in the frequency range of 3.50×10^{-2} and 4.23×10^{-2} cph which encompasses the frequency of the O_1 tidal constituent.

Mountain (1980) discusses the spectra obtained from the along- and cross-slope velocity records (April-June) from current meters at 110 and 380 m (490 m bottom depth) in the high speed core of the Labrador Current to the southwest of Carson Canyon. Strong spectral peaks for the semi-diurnal signal in all three velocity component records are reported, as are small, statistically non-significant peaks (at the 95% confidence level) for the inertial and diurnal frequencies. Seaconsult (1978) reports a negligible tidal signal and a strong inertial signal (as does Hayes, 1984)
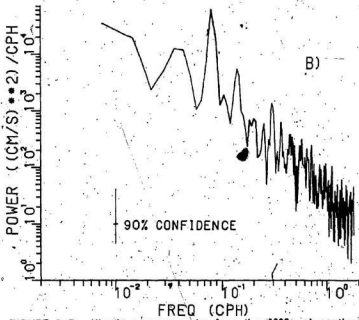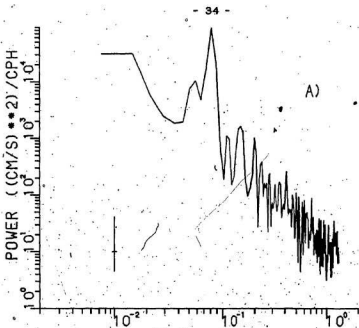
FIGURE 3.7: Kinetic energy spectra from the 1980: a) southwestern, and b) northeastern current meter, despiked data (90% confidence intervals).

for the summertime records of a current meter at 168 m depth (≈ 800 m above bottom) in the Labrador Current at Flemish Pass. The absence of strong tidal signals is probably related to the greater water depth at the mooring in Flemish Pass. The Seaconsult (1978) report specifies that the strong currents observed at the inertial frequency consist of bursts of internal wave activity. According to Robe (1975), the M_2 tide was the only periodic component that could be identified in the May-June velocity records from a current meter which was situated 40 m above bottom, 31.5 km upstream of Carson Canyon where the bottom depth is 951 m.

3.3 Meteorological and tidal data

Wind velocities (Figures 3.8a and b), obtained at Hibernia in 1980 are resolved along the direction of the continental slope immediately upstream of Carson Canyon in the meteorological sense: positive A (45°T) gives the northeasterly (along-slope) wind component and positive C (315°T) gives the northwesterly (cross-slope) component. It is evident from Figure 3.8a and 3.8b that no major storm activity took place during the research cruise. Note that the recorded wind speeds did not exceed 16 m s^{-1}, and, that there are no obvious wind-related effects in the current meter records.

The tidal height at Hibernia for the mooring period in June of 1980 is given in Figure 3.8c. The tide at Carson Canyon is estimated to lag Hibernia by about 10 minutes (as estimated from a co-tidal chart for the M_2 tide in the Atlantic, Neumann and Pierson 1966, p. 320).
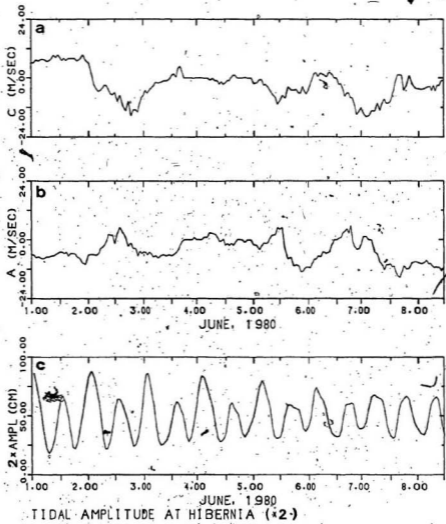
FIGURE 3.8: a) Northwesterly (C = 315 °T) and b) northeasterly (A = 45 °T) winds, and c) tidal heights for June, 1980 at Hibernia

3.4 1980 CTD data

Sixty-four CTD casts. the locations of which are shown in Figure 3.1. were made in the Carson Canyon area. The time. position. and depth of each cast are listed in Table A2 of Appendix A. A 23-hour time-series of hourly CTD casts was conducted at station 11 at the center of the canyon.

3.4.1 Temperature and salinity sections

The vertical cross-sections of temperature taken from CTD transects are presented in Figure 3.9 and 3.10. These figures represent transects across the slope to the northeast (NE) of Carson Canyon. along the central axis (CA). along the southwest canyon wall (SW); and across the slope to the far southwest (FS) of the canyon. Corresponding salinity sections follow in Figures 3.11 - 3.12. The presence of Labrador Current Water is indicated by cold temperatures of 0 °C or less. and salinities between 33 and 34 ppt. (Because of the cold temperatures. density is primarily determined by salinity. and so. isopycnals are approximately equivalent to isohalines). Note that stations 20. 21 and 33. 39 are repeated in the CA and SW sections. as are stations 39 and 40 in the CA. SW and FS sections.

Intrusions of warm water. possibly representing interleaving. are centered at about 200 m to the southeast (the right hand side) of all the temperature and salinity sections except for the NE salinity section.

The presence of localized deformations in the isolines of temperature and salinity at certain of the stations. which appear as peaks. are probably caused by tidal aliasing as will shortly be demonstrated.

- 38 -
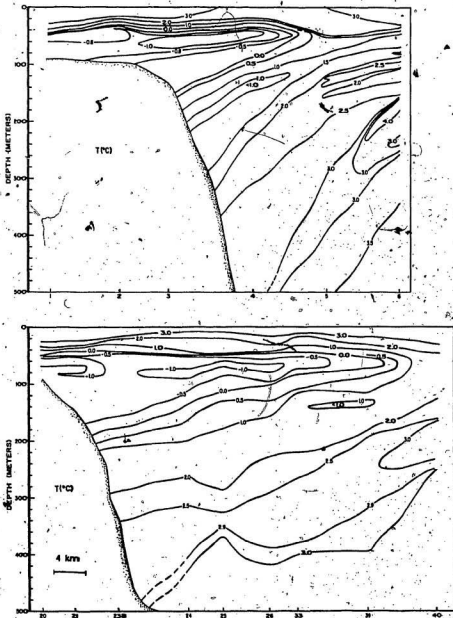
FIGURE 3.9: Top, Northeastern (NE) and bottom, Central Axis (CA) temperature sections for 1980
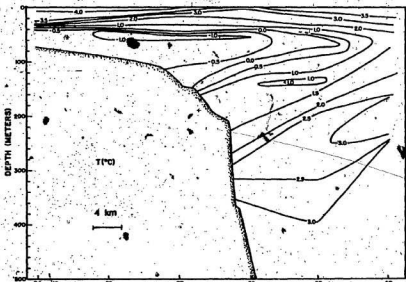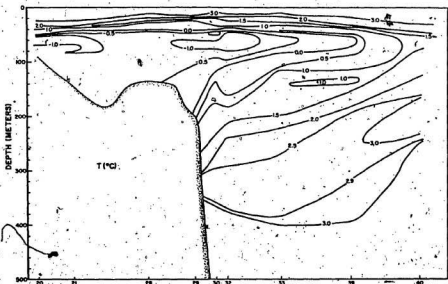
FIGURE 3.10: Top, Southwestern (SW) and bottom, Far Southwestern (FS) temperature sections for 1980
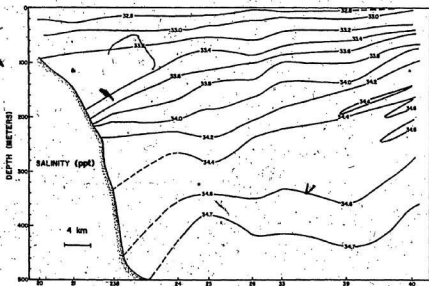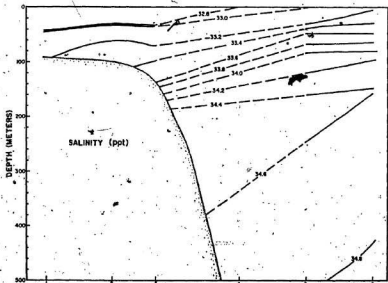
FIGURE 3.11: Top, Northeastern (NE) and bottom, Central Axis (CA) salinity sections for 1980
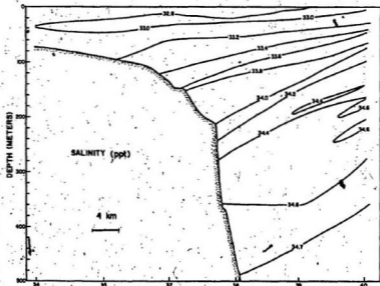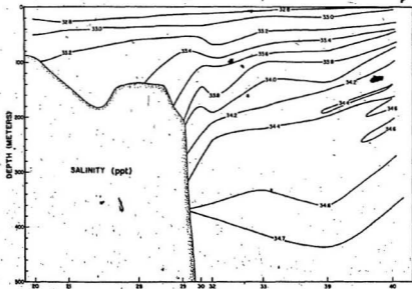
FIGURE 3.12: Top, Southwestern (SW) and bottom, Far Southwestern (FS) salinity sections for 1980.

A Labrador Current "cold core", as it is referred to here, is defined by the region enclosed by the $-1\,°C$ isotherm. A core of temperatures $\leqslant -1\,°C$ centered at about 100 m depth is a feature typically observed in the Labrador Current (Seaconsult 1978, p. 22) and measurements of $-1.5\,°C$ have been observed uniformly throughout the length of the Labrador Current as far south as $43\,°N$ (Smith et al. 1937, p. 27). At least one cold core is observed at a depth of ≈ 70 m in every temperature section. A single cold core is observed above the shelf break (the 110 m isobath) in the two temperature sections (NE and FS) furthest removed from the canyon (Figures 3.9 and 3.10). The CA and the SW temperature sections exhibit two cold cores. An "inner" cold core is seen to extend over the shelf break at the head of the canyon in each of these two canyon transects. Note, however, that although the "outer" core is defined by different stations in each section, the same pair of stations are within the inner core in each case.

The cold core in the NE transect spans the 500 m contour, which is the location of the Labrador Current velocity core estimated by Mountain (1980). The projection of the 500 m isobath from the northeast slope into the canyon (Figure 3.1) intersects the outer cold cores of the CA (Figure 3.9) and SW (Figure 3.10) temperature sections by passing through the canyon just to the northeast of either CTD 26 or CTD 33. The center of the cold core in the FS section (Figure 3.10) is located in much shallower water than in the NE section (Figure 3.9).

The existence of two cold cores in the canyon transects does not appear to be an artifact of the CTD cast times (see Table A2 in Appendix A). If two cold cores are observed because a single stream (as in the NE and FS sections) was laterally advected along the canyon axis, then

the stream would have had to move up-canyon from station 24, past station 23B to station 21 at a rate in excess of 2 m s^{-1}. Then the single stream would have had to shift down-canyon along the southwest wall from station 21, and pass station 28 to arrive at station 30 with a rate greater than 3 m s^{-1}. These high speed fluctuations are unrealistic.

3.4.2 23-Hour time-series

The temperature and salinity time-series data from the 23 CTD casts performed at station 11 are displayed as depth vs. time graphs in Figure 3.13. The 23-hour time-series exhibit an apparent internal tide at the semi-diurnal frequency. The upward displacements of the isotherms and isohalines above 300 m depth are largest between 100 and 200 m. Peak displacements occur at about 0600 hours and 1800 hours and correlate well with the occurrence of high water at Hibernia (Figure 3.8c). In the previous section it was pointed out that the peaks in the isotherms and isohalines in the off-shelf transects are probably due to tidal aliasing. The observation of vertical tidal excursions on the order of 100 m in only 3 to 4 hours corroborates this point. Note also the sudden increase in the width of the cold core at 0700 GMT, and later, in the width of the region enclosed by the -1.2 °C isotherm at 2000 GMT, both of which times correspond to high tide.

Ship drift while on station may contribute significantly to the variability observed in the 23-hour series. Estimates of this sort of error are difficult to make, however, especially because cross-canyon temperature and salinity gradients are not known.
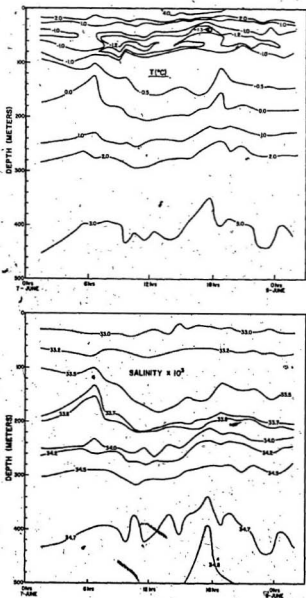
FIGURE 3.13: Time-series of temperature (top) and salinity (bottom) at the 1980 CTD station 11ª

3.5 Dynamic topography

Contours of the dynamic topography of the 5 dbar surface relative to 200 dbar are superimposed on the bathymetry in Figure 3.14. Dashed contours indicate where the extrapolation technique of Reid and Mantyla (1976) has been used used to obtain values on the shelf (see Chapter 5), and where there is an insufficient number of stations on the downstream side of the canyon.

A time-series of the dynamic height (Figure 3.15) of the 5 dbar surface relative to 200 dbar has been derived from the 23 casts at station 11. There is pronounced variability in the dynamic height values at the semi-diurnal frequency, with peak-to-peak changes of as much as 2 dyn cm. The minima in the dynamic height series approximately corresponds with times of high tide (Figure 3.8c). Similarly, the maximum peak in the dynamic height corresponds to low tide (which occurs at 1300 hours). The variability bears important consequences for the contouring of dynamic topography at Carson Canyon since a range of 2 dyn cm represents a significant fraction of the variation in dynamic height over the upper canyon (Figure 3.14). It is possible that internal wave trapping (Chapter 1) may enhance tidal aliasing within the canyon. Precisely how much ship drift at station 11 contributes to the variability of the time-series in Figure 3.15 cannot be ascertained. It may be noted, however, that the gradient of the dynamic topography near station 11 (Figures 3.1 and 3.14) is such that as much as 50% of the peak-to-peak change in the dynamic height series could be accounted for by a ship drift of a few kilometers.
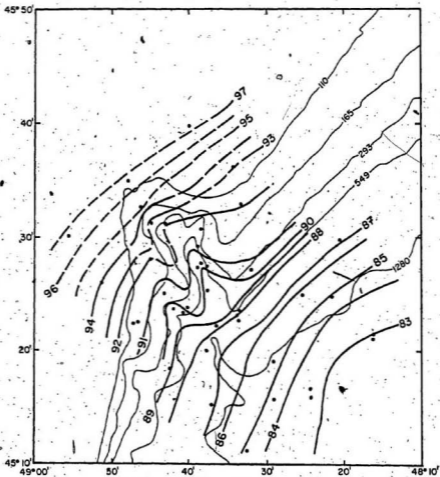
FIGURE 3.14: Dynamic topography (heavy lines) of the 5 dbar surface relative to 200 dbar (expressed in dyn cm = (dynamic height — 189) x 100) superimposed on the bathymetry (light lines with depth in meters). The solid circles indicate 1980 CTD station positions.
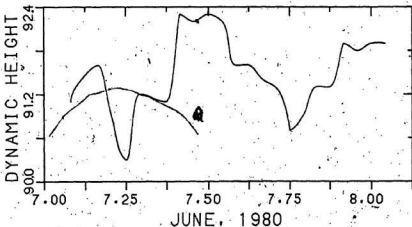
FIGURE 3.15: Time-series of dynamic heights (in dyn cm) of the 5 dbar surface relative to 200 dbar at the 1980 CTD station 11 with the date in June along the horizontal axis.

Despite these uncertainties, the dynamic topography in Figure 3.14 exhibits a number of interesting features, including shelfward deflection of the dynamic height contours at the canyon and a distinctive wave-like pattern in the canyon lee. These features are discussed further in Chapter 5.

An estimate for the geostrophic speed at the Labrador Current axis upstream of Carson Canyon is 48 cm s^{-1}, calculated from the 1980 CTD pair 10-8 (see Figure 3.1). The axis of the Labrador Current velocity core (as distinct from the axis of the -1 °C cold core) is estimated to follow the 500 m isobath where the gradient of the dynamic topography (Figure 3.14) is greatest at this location. This depth, it may be recalled

from Chapter 1, compares with a depth of 490 m which Mountain (1980) estimates to be the depth over which the high speed velocity core of the Labrador Current may be found. The figure of 48 cm s^{-1} compares favorably to the values of 46 cm s^{-1} and 60 cm s^{-1} for the average and maximum speeds reported respectively by Mountain (1980) from direct current measurements and by Robe (1975) from geostrophic velocity estimates.

CHAPTER 4   1981 DATA

Figure 4.1 shows the locations of the 1981 current meter moorings and CTD stations at Carson Canyon. Table 4.1 presents details concerning the current meter moorings.

TABLE 4.1: 1981 Mooring information				
Mooring	81-1	81-3	81-2	
Inst.	southwestern	northeastern	central axis upper	lower
Inst. depth	145 m	144 m	168 m	703 m
Bottom depth	155 m	154 m		713 m
N. Latitude	45° 29.5'	45° 31.4'	45° 29.1'	
W. Longitude	48° 43.9'	48° 36.2'	48° 39.6'	
Deployed	2135/5 June	2305/5 June	1650/4 June	
Recovered	0930/18 June	1145/18 June	1800/19 June	
Sampling interval	5 min	5 min	5 min	
Orientation *	150 °T	350 °T	210 °T	

* The orientation is the angle of the isobath at a given mooring in the downstream (J component of velocity) direction.

The data for each of the four current meters are presented on separate figures in the following order: the southwestern meter, the only meter (at a depth of 145 m) on mooring 81-1; the central axis upper meter (168 m depth), the uppermost of two meters on mooring 81-2 and the only current meter not positioned 10 m above bottom; the central axis lower meter (703 m depth), the bottom meter on mooring 81-2; the northeastern current meter, the sole meter (144 m depth) on mooring 81-3. The southwestern, central axis upper and northeastern current meters will sometimes be referred to as the "shallow" current meters. Dates marked on time-series plots denote 0000 h. Additional plots of data not discussed in detail in the text appear in Appendix B at the end of this thesis.

- 50 -
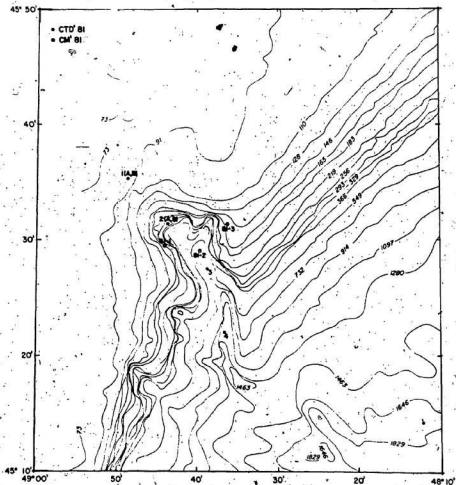
FIGURE 4.1: Current meter mooring (open circles) and CTD station (solid circles) locations for 1981 (depth in meters).

4.1 1981 Current meter records

Figures 4.2 – 4.5 give the FLP ("first low-pass" filtered) series of temperature, salinity, and the I (cross-isobath) and J (along-isobath) components of velocity for each of the 1981 current meters. Prior to about 9 June and after about 15 June, the FLP records of temperature and salinity of the shallow current meters exhibit characteristics (i.e. temperatures and salinities between 33 – 33.5 ppt) typical of the Labrador Current. The temperatures and salinities are generally much greater at the central axis lower meter (Figure 4.4) because of that current meter's greater depth (note the different temperature scale for this instrument).

A striking feature in the FLP time-series, beginning about midday on 9 June, is the large and abrupt increase and subsequent gradual decrease in both temperature and salinity recorded by the shallow current meters (Figures 4.2, 4.3 and 4.5), and to a lesser extent, an increase in temperature recorded by the central axis lower meter (Figure 4.4). Maximum temperatures (nearly 2 °C) and salinities (nearly 34.5 ppt) for the shallow current meters are characteristic of deeper water. These records therefore suggest the occurrence of an upwelling event of ~ 5 d duration. The most intense signs of upwelling in the temperature and salinity records were registered at the southwestern (81-3) mooring, starting at 1420 h, 9 June (Figure 4.2). The starting times of the increases recorded by the other shallow current meters are difficult to ascertain because of the stronger semi-diurnal signal. Although better demonstrated in subsequent plots, examination of Figures 4.2 – 4.5 indicates that substantial changes in the current velocities precede the temperature and salinity increases
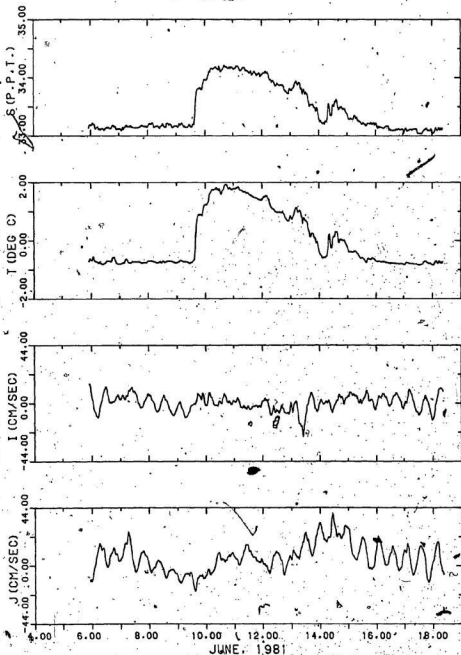
FIGURE 4.2: FLP time-series of temperature, salinity, and the I and J components of velocity for the 1981 southwestern meter (mooring 81-1).
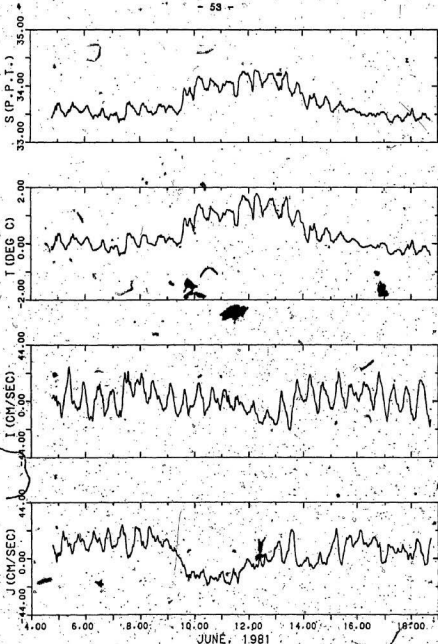
FIGURE 4.3: FLP time-series of temperature, salinity, and the I and J components of velocity for the central axis upper meter (mooring 81-2).
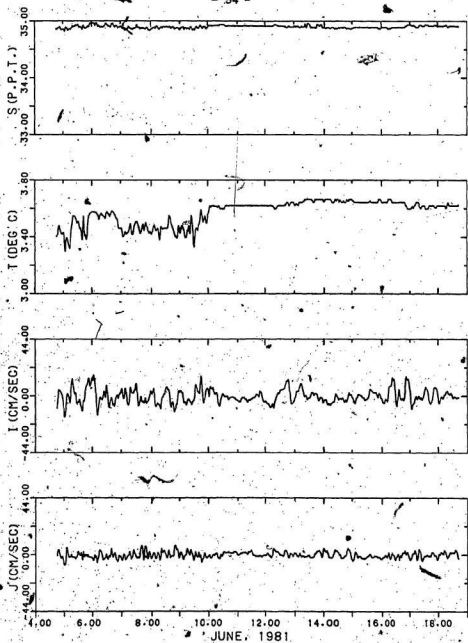
FIGURE 4.4.   FLP time-series of temperature, salinity, and the I and J components of velocity for the central axis lower meter (mooring 81-2). The temperature scale differs from Figures 4.2, 4.3 and 4.5.
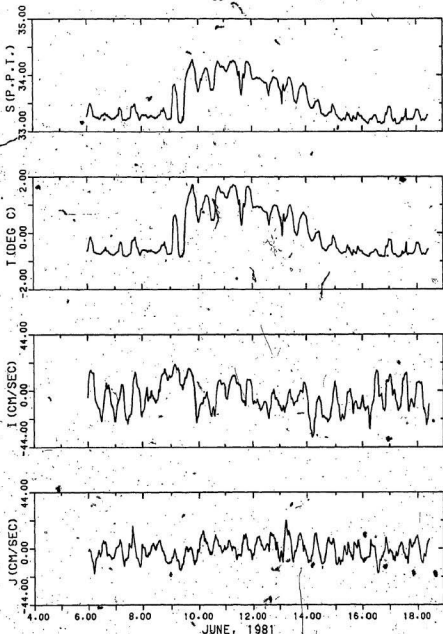
FIGURE 4.5. FLP time-series of temperature, salinity, and the I and J components of velocity for the 1981 northeastern meter (mooring 83-3).

which occur during June 9. This effect is most apparent in Figure 4.3 as an abrupt decrease of the J component of velocity as recorded by the central-axis upper meter at near 0000 h on 9 June, which, upon comparison with the top two plots in the same figure, precedes the increases in temperature and salinity by about half a day. Henceforth, the upwelling of intermediate water, along with associated changes in current patterns from those existing prior to 8 June, 1981, will be referred to in this thesis as the "upwelling event", or briefly, the "event".

With few exceptions, a vigorous semi-diurnal tide is clearly evident in all of the records presented in Figures 4.2 - 4.5. The exceptions are: the absence of this tidal signal in the temperature and salinity records from the southwestern (Figure 4.2) and central axis lower (Figure 4.4) meters; and in the J component of velocity for the central axis lower meter.

The SLP filtered records ("second low-pass" filtered to remove inertial, semi-diurnal and higher frequency signals) are presented in Figures 4.6 - 4.9. Peak temperatures and salinities were recorded by the southwestern meter towards the end of 10 June (Figure 4.6), and by the northeastern meter early on 11 June (Figure 4.9). The central axis lower meter also indicates a temperature response to the event. At midday on June 9, the mean temperature rose by ≈ 0.2 °C (Figure 4.8), about 1/10 that at the shallow meters. The higher temperatures at the deep, central axis lower meter persist longer than the time taken for the shallow current meters to show a recovery from the upwelling event.

FIGURE .4. 6: SLP time-series of temperature, salinity, and the I and J components of velocity for the 1981 southwestern meter (mooring 81-1).

FIGURE 4.7: SLP time-series of temperature, salinity, and the I and J components of velocity for the central axis upper meter (mooring 81-2).
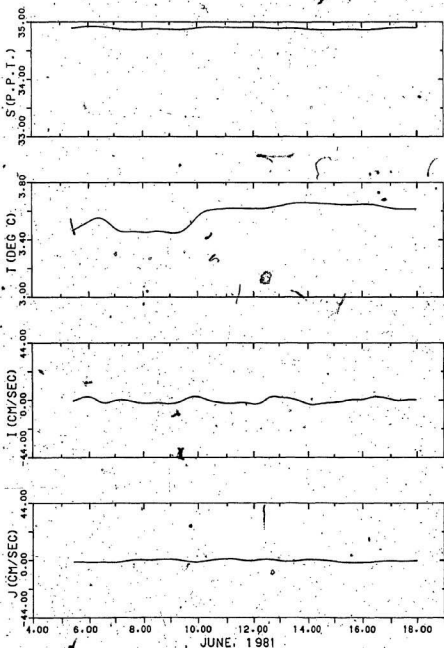
FIGURE 4.8: SLP time-series of temperature, salinity, and the I and J components of velocity, for the central axis lower meter (mooring 81-2). The temperature scale differs from Figures 4.6, 4.7 and 4.9.
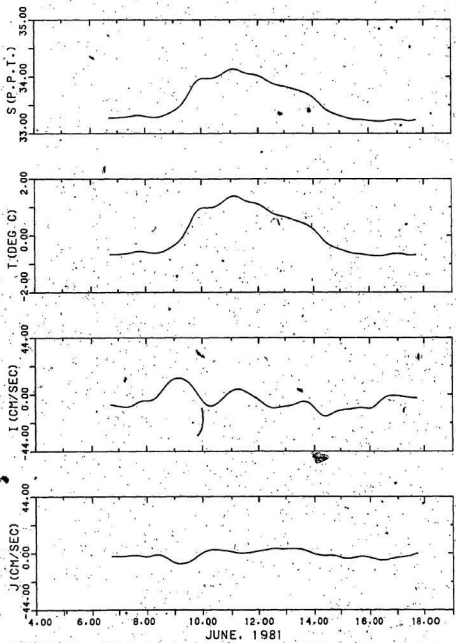
FIGURE 4.9: SLP time-series of temperature, salinity, and the I and J components of velocity for the 1981 northeastern meter (mooring 83-3).

Changes in the velocity field associated with the event are brought out most clearly in Progressive Vector Diagrams. PVD's computed from the SLP filtered data for each of the four 1981 current meters are given in Figures 4.10 — 4.13. Asterisks mark 0000 h for each day. Figure 4.10, the PVD for the southwestern meter (145 m depth on mooring 81-1, Figure 4.1), shows clearly the start of the upwelling event on 8 June when the mean southward flow slows and then completely reverses to the north. After about 1.5 d of reversed flow, an anticlockwise rotation of the flow direction develops. The flow is cross-canyon to the east on June 12; during June 13, it accelerates towards the southsouthwest; and on 15 June, the velocity shifts toward the south and decelerates for the remainder of the record.

In Figure 4.11, southwestward flow is indicated by the PVD for the central axis upper meter (168 m depth on mooring 81-2, Figure 4.1) prior to 9 June. On 9 June the current slows, reverses toward the north-northwest, and continues in this direction almost until June 12. A clockwise rotation then occurs until June 15, when the flow shifts abruptly southeastward, the same direction as that prior to the event, and maintains this direction to the end of the record.

The PVD for the central axis lower meter presented in Figure 4.12 (703 m depth on mooring 81-2, Figure 4.1) is scaled 16 times larger than the others. A net northeastward drift of 0.9 cm s^{-1} toward the secondary head (Figure 4.1), is observed between 5 and 8 June. A mean downcanyon (southeastward) drift of 0.9 cm s^{-1} occurs during the event between 8 and 15 June.
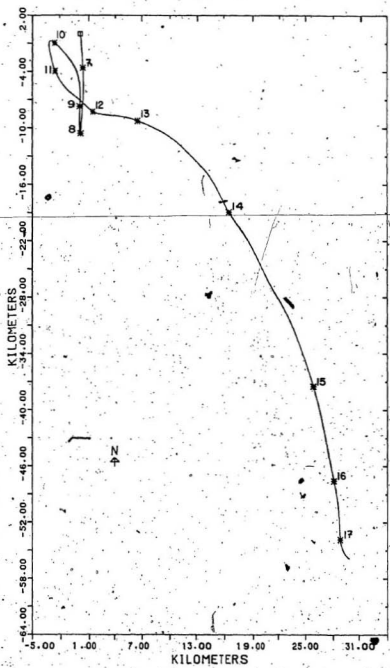
FIGURE 4. 10: SLP PVD: 1981 southwestern meter. mooring (81-1)
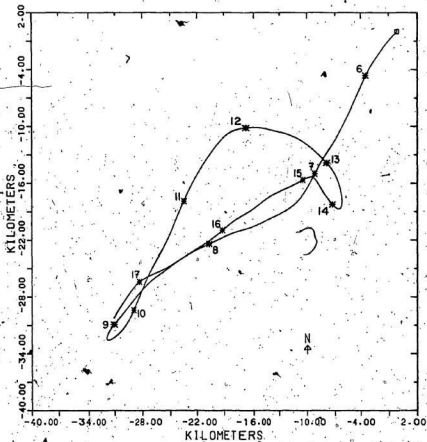
FIGURE 4.11: SLP PVD: 1981 central axis upper meter, mooring (81-2).
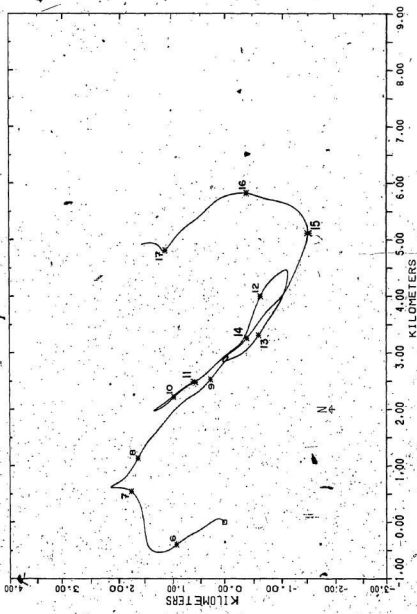
FIGURE 4.12: SLP PVD: 1981 central axis lower meter...mooring (81-2). Note the change in scale from Figures 4.10, 4.11 and 4.13
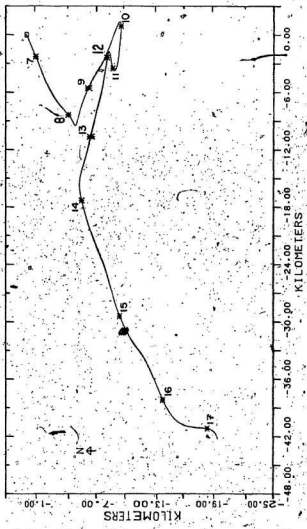
FIGURE 4.13: SLP PVD for the 1981 northeastern meter, mooring (BT-3)

The PVD for the northeastern meter (144 m on mooring 81-3, Figure 4.1) is presented in Figure 4.13. Southwestward flow is indicated during the period before the start of the upwelling event, and from 14 June until the record ends. During June 8 the current direction shifts to southeastward, but does not reverse. Late on 9 June, the current direction rotates clockwise, and is generally westnorthwestward until late on 13 June. From June 14 on, the flow returns to the southwest direction, but begins to slow markedly on 16 June.

The PVD's permit the "onset" of the event in the velocity records to be defined in terms of the initial changes in direction; the reversals at the southwestern and central axis upper meters; and the near reversal at the northeastern meter. These direction changes correspond to zero-crossings of the J component at the southwestern and central axis upper meters (Figures 4.6 and 4.7), and of the I component at the northeastern meter (Figure 4.9). This definition corresponds to onset times of; 0700 h, 8 June at the southwestern meter; 1000 h, 9 June at the central axis upper meter; and 1000 h, 8 June at the northeastern meter. The actual times of onset, corresponding to initial deceleration of the mean flow, are difficult to define in terms of the SLP velocity components and the PVD's, but are estimated to lead the times defined above by 0.25 - 0.5 d. For example, the abrupt decrease of the J component recorded by the central axis upper meter at 0000 h, 8 June (Figure 4.3) which does not appear to be tidally induced, occurs 0.4 d before the zero-crossing time above.

4.1.1 Vector plots

The 24 h segment-averaged velocity vectors for each of the shallow meters are plotted in Figure 4.14. The vectors represent the sum of the SLP filtered components from each of the 1981 shallow current meters after averaging over non-overlapping 24-hour segments. The segment-averaged vectors are plotted at the corresponding mooring positions on a plan-view chart showing the 160 m isobath at Carson Canyon. Only data from the central axis upper meter were available during the first 24 h period (6 June). Vectors were not drawn (after 6 June) if the speed was less than 0.7 cm.s^{-1}. The midpoints of the segment intervals correspond to 0530 GMT on the corresponding day. (12-hour segment-averaged vector plots are given in Figure B23 of Appendix B.)

The steady state circulation at Carson Canyon, unperturbed by the upwelling event, is inferred from the vector plot for 7 June (the currents are averaged between 1730 h. 6 June - 1730 h. 7 June). Note that a line drawn through the northeastern (81-3) and central axis (81-2) mooring positions parallels the continental slope upstream of Carson Canyon and that although there is some shelfward flow (i.e. 20° deflection towards the canyon head) indicated by the northeastern meter on 7 June, the cross-canyon flow observed by the central axis upper meter is parallel to the upstream isobaths. The current vector at the central axis upper mooring in the 6 June frame does show a down-canyon deflection of the mean current.

The first evidence of the upwelling event in Figure 4.14 is a deceleration of the flow at the southwestern (81-1) and northeastern (81-3) moorings on June 8. A pattern suggestive of a clockwise gyre over Carson Canyon develops by 9 June but then changes to an anticlockwise
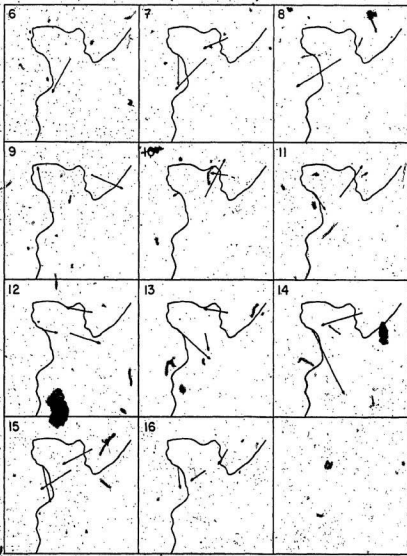
24 HR., START 05:30Z 6/06/81. 1CM=10CM/SEC

FIGURE 4.14: 24-hour segment-averaged vector plots for the 1981 shallow current meters. The 160 m isobath and the date in June are shown. The midpoint of each interval is 0530 GMT (Z)

pattern on 10 June. The anticlockwise motion persists until 14 June, when the pattern changes drastically with the development of up-canyon flow at the central axis (81-2) mooring. The circulation indicated in Figure 4.14 for 14 June shows that maximum mean currents are observed by both the southwestern and northeastern meters at this time (1730 h. 13 June – 1730 h. 14 June) which reflects the accelerations indicated in the PVD's in Figures 4.10 and 4.13. A day later, on 15 June, the circulation pattern appears to nearly return to that of 7 June, although the mean flow over the canyon continues to decelerate as indicated by the plot for 16 June. Figure 4.14 shows that the currents at the southwestern (81-1) mooring generally are constrained to follow the bathymetry. The mean current on 9 June at the northeastern (81-3) mooring possesses a large cross-isobath component (see also the l component of velocity. Figure 4.9) which is concurrent with the initial temperature and salinity increases associated with the upwelling event. However, this flow is in fact directed off-shelf. Only a north to northeastward flow, such as indicated by the vector of June 11 at this same mooring, can definitely travel onto the shelf. The temperature and salinity maxima at mooring 81-3 occurred during this period (Figure 4.9).

Figure 4.15a presents an overlay of the SLP temperature time-series recorded by the shallow current meters. The highest temperature (1.8 °C) was recorded by the southwestern meter, the maximum temperatures observed at the northeastern and central axis upper meters both being 1.4 °C. The first increase in mean temperature is indicated in the northeastern meter record at 1600 h, 8 June, followed by increases recorded by the southwestern meter at 0500 h, 9 June, and then the central axis upper meter at 1000 h on 9 June. This sequence indicates that
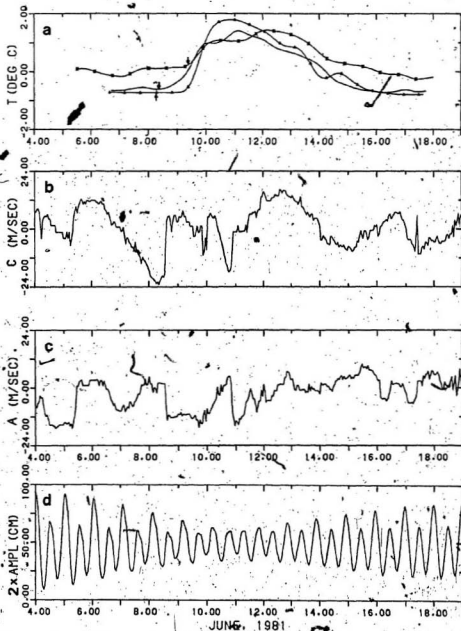
FIGURE 4.15: a) Overlay of the SLP: southwestern (triangle), northeastern (line), and central axis upper (star) current meter temperature records. b) Northwesterly (C = 315 °T) and c) northeasterly (A = 45 °T) winds. d) Tidal heights at Hibernia.

JUNE, 1981

the upwelling perturbation propagated along the lip of the canyon with shallow water to the right before moving into deeper water. Peak temperatures are observed at progressively later times; on the evening of 10 June at the southwestern meter, early on 11 June at the northeastern meter, and early on 12 June at the central axis upper meter. All of the records indicate essentially complete decay of upwelling by 16 June. Maximum temperatures at the southwestern and northeastern meters correspond to the of upslope flow at each mooring (Figure 4.14) on June 10 and 11 respectively. Note, however, that these upslope flows indicate on-shelf upwelling in opposite directions. Referring now to the SLP temperature record of the central axis lower meter (Figure 4.8), the maximum temperature occurs near the end of 13 June, later than in the other temperature records. The start of the increase, midday on 9 June, is about the same as that measured by the central axis upper meter, but the relaxation time is much longer than the 5 or so days estimated for the shallow current meters. Also shown in Figure 4.15a, are arrows indicating the times at which the onset of the event was reflected in the velocity field, according to the definition discussed previously. Consequently, it is seen that the initial increases in mean temperature (and salinity; compare Figures 4.6, 4.7 and 4.9), lag the onset times defined for the velocity records at the northeastern and southwestern meters by ≈ 0.25 - 1 d.

4.2 Meteorological and tidal data

Wind velocities presented in Figures 4.15b and 4.15c, obtained in 1981 from an anemometer at 76 m above mean sea level on a drilling rig in the Hibernia field (Figure 1.1), are resolved parallel to the continental slope upstream of Carson Canyon with positive A being northeasterly

(45 °T) and positive C northwesterly (315 °T). Unlike the previous year
(see Figure 3.8), intense southeasterlies of about 0.5 d duration (June 7
~ 8, Figure 4.15c) accompanied a severe storm while the 1981 current
meter moorings were deployed. The peak wind speed at Hibernia of
23 m s^{-1} directed from 130 °T (C = -23 m s^{-1}, A = 0) was observed at
0600 h, 8 June. The high winds were generated by the passage of a
trowal ("transfer of warm air aloft") which was associated with a low pres-
sure system centered to the northwest of the Hibernia-Carson Canyon
region. The storm development, including the passage of the trowal
(marked by northwestward pointing arrows at Carson Canyon on 8 June),
is shown in the surface pressure charts reproduced in Figures 4.16 and
4.17. These charts indicate that the intense southeasterlies on June 7
and 8 at Hibernia were preceded by high winds at sea level from the
south to southwest at Carson Canyon. Consequently, it is suggested that
high speed along-slope southwesterlies, which lasted for about half a day,
developed at Carson Canyon sometime on 7 June and peaked earlier than
0600 h, 8 June. It is near the start of 8 June that the flow at the
southwestern and northeastern meters began to slow before the onset of
the event (i.e. before the establishment of an anticlockwise pattern over
the canyon apparent in Figure 4.14; see also Figure B23), and about 1 d
before the first increase in mean temperature was registered by the
northeastern meter (Figure 4.15a). The role of the strong, impulsive,
northwestward (along-slope) wind stress in the upwelling event of 1981 will
be discussed later.

Tidal heights at Hibernia are plotted in Figure 4.15d. Neap tide
coincides with a decreased amplitude of the M_2 signal between 10 - 13
June in the FLP filtered velocity components shown in Figures 4.2 - 4.5.
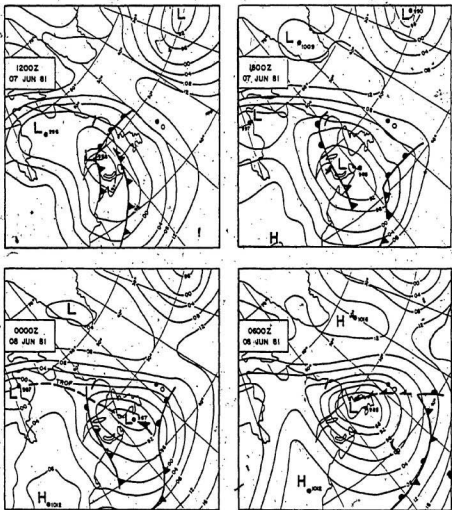
FIGURE 4.16: 6-Hourly surface pressure charts from 1200 GMT (Z) 7 June to 0600 GMT 8 June, 1981, at Carson Canyon (open circle) and Hibernia (closed circle to the north).
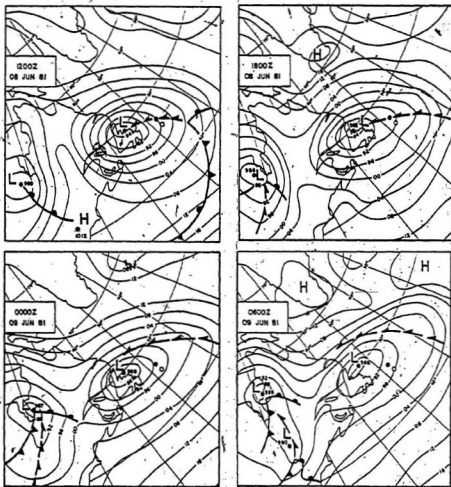
FIGURE 4.17: 6-Hourly surface pressure charts from 1200 GMT (Z) 8
June to 0600 GMT 9 June, 1981 at Carson Canyon (open
circle) and Hibernia (closed circle to the north).

The higher frequency internal wave signals in the velocity records from the central axis lower meter (Figure 4.4) are also suppressed during this period. The correlation between neap tide and the observed currents might be coincidental however. Huthnance (1981) reports that the neap-spring cycle is not usually seen in current meter time-series obtained on or near the continental slope. Additionally, it was found by Hayes and Halpern (1976) that the horizontal kinetic energy of the baroclinic M_2 tide was reduced near the coast during an upwelling event. A similar effect at Carson Canyon is suggested by the increased amplitude of the semi-diurnal signal over the period of the event in the FLP series of temperature and salinity for the shallow current meters plotted in Figures 4.3 and 4.5 (see also the BP filtered records in Figures B8 and B10 in Appendix B). The larger peaks in temperature and salinity during neap tide suggest increased gradients due to the presence of upwelled warmer, more saline water in Carson Canyon. (Take special note of the large, isolated tidally induced peaks at 0600 h on 9 June in the temperature and salinity records of the northeastern meter, Figure 4.5, before the increases become sustained over more than one phase of the tide.)

4.3 Comparison of the 1980 and 1981 current meter data

Mean values from the despiked time-series of temperature, salinity and the I and J components of velocity recorded before 0000 h, 8 June by the 1981 current meters are presented in Table 4.2. Those figures are also compared in Table 4.2 to mean values over the entire deployment period for the 1981 current meters (additional statistics are presented in Tables B1 A-D), and to the similar mean values available from 1980 (also see Table A1 in Appendix A for the 1980 current meter statistics).

TABLE 4.2: Mean values of despiked current meter data from 1980 and 1981

current meter †	Temp. (°C)	Sal (ppt)	I (cm s⁻¹)	J (cm s⁻¹)	(I² + J²)^(1/2) (cm s⁻¹)
1981					
SWN					
≤ 8 June	-0.73	33.15	3.6	6.9	7.8
Total	0.00	33.45	0.4	6.3	6.3
CAU					
≤ 8 June	-0.01	33.54	2.9	12.8	13.1
Total	0.38	33.70	1.1	4.2	4.4
CAL					
≤ 8 June	3.48	34.89	-0.4	-1.0	1.1
Total	3.57	34.90	-0.4	-0.4	0.5
NEN					
≤ 8 June	-0.60	33.30	-5.8	-3.2	6.5
Total	-0.02	33.53	-4.7	-1.4	4.9
1980					
SWN					
Total	-0.59	-	3.7	18.2	18.6
NEN					
Total	-	-	3.9	19.0	19.4

† SWN = southwestern, CAU = central axis upper,
CAL = central axis lower, NEN = northeastern.

Table 4.2 shows that there is no large difference between the average temperature recorded by the 1980 southwestern meter and those for the 1981, southwestern and northeastern meters, prior to 0000 h, 8 June. As a further comparison, Figure 4.18 demonstrates the high degree of similarity between a segment of the FLP temperature record from the 1980 southwestern meter (see Figure 3.4) and the first 2.5 d of the FLP temperature record from the 1981 northeastern meter. (The 1981 northeastern meter was chosen for comparison since it is possibly the least affected by the topographical influence of Carson Canyon; no temperature record was obtained from the 1980 northeastern meter.) According to Table 4.2, velocity magnitudes at the 1981 shallow current meters ≤ 0000 h, 8 June, are typically much lower than the values from 1980.

which could be due to the influence of the canyon or to the cross-slope current shear of the Labrador Current (discussed in Chapters 3 and 5). Average increases of temperature, 0.57 C°, and of salinity, 0.23 ppt, are computed from Table 4.2 for all three shallow current meters from before 8 June to that of the totals. Perhaps the most noticeable effect of the event on the mean values is a 2 to 3-fold decrease in the speeds observed at the central axis (81⌣2) mooring. In addition, the mean velocity components for 1981 in Table 4.2 are greater during the period prior to the upwelling event than those for the entire period.
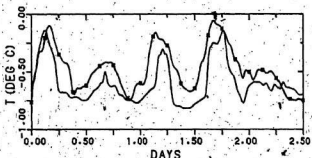
FIGURE 4.18: Overlay of 2.5 d of the FLP-filtered temperature time-series from the 1980 southwestern (star) and 1981 northeastern (line) current meter records.

4.4 1981 Kinetic energy spectra

As in Chapter 3, the results of the spectral analyses are not central to the thesis, but are presented for completeness. Plots of the kinetic energy spectra for each of the 1981 current meters are presented in Figures 4.19 and 4.20. Spectra for the 1981 current meters differ in many
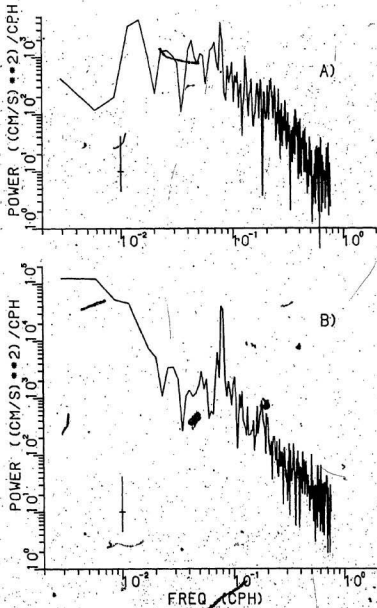
FIGURE 4.19: Kinetic energy spectra from the 1981: a) central axis lower, and b) central axis upper current meter, despiked time-series (with 90% confidence intervals).
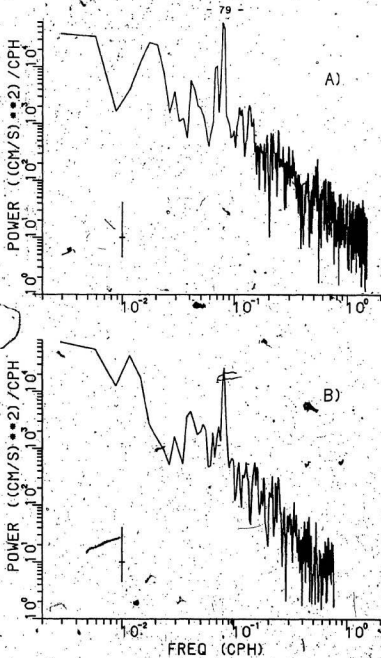
FIGURE 4.20: Kinetic energy spectra from the 1981: a) northeastern, and b) southwestern current meter, (despiked time-series (with 90% confidence intervals).

respects from the description of those for 1980 (Chapter 3). The foremost difference is that the maximum energy spectral densities in the 1981 spectra correspond not to the M_2 tide (frequency = 8.05×10^{-2} cph) but to lower frequencies, except for the 1981 northeastern meter (Figure 4.20a), for which the maximum spectral density occurs at the M_2 tidal frequency. Another feature observed in all the 1981 spectra, but not in the 1980 spectra, is the presence of broad peaks between the O_1 tidal and the inertial frequencies (3.87×10^{-2} and 5.96×10^{-2} cph respectively). These maxima might be associated with the effects of the sheared current on internal-inertial oscillations induced by wind-impulse forcing (Mayer, et al. 1981). The spectrum of the central axis lower meter (Figure 4.19a) contains the least energy of all and shows two distinct and relatively broad peaks centered at 2.43×10^{-2} and 1.35×10^{-2} cph. This spectrum, unlike the others, is not reddened: the energy density does not increase at the lowest frequencies. A broad peak in the spectrum of the northeastern meter (Figure 4.20a) is clearly defined at 1.62×10^{-2} cph.

A notable feature of these spectra is the presence of secondary peaks with frequencies slightly smaller than the M_2 tide but larger than the inertial frequency at about 7.3×10^{-2} cph. However, only for the spectrum for the northeastern meter (Figure 4.20a) is the secondary peak statistically significant. The cause(s) of the secondary peaks near the M_2 tide in the Carson Canyon spectra is (are) not known. The spectrum for the deep, central axis lower meter (Figure 4.19a) shows that statistically significant energy (4×10^{3} cm^2 s^{-2} cph^{-1}) was generated at the semi-diurnal frequency in Carson Canyon at 700 m depth. Also, because of the near equivalence in depths among the shallow current meters (see

Table 4.1), there is evidently a southwestward cross-canyon decrease in power of the M_2 tide: at the northeastern ($59 \times 10^3 \ cm^2 \ s^{-2} \ cph^{-1}$, Figure 4.20a); central axis upper ($40 \times 10^3 \ cm^2 \ s^{-2} \ cph^{-1}$, Figure 4.19b); and southwestern ($26 \times 10^3 \ cm^2 \ s^{-2} \ cph^{-1}$, Figure 4.20b) current-meter positions. In 1980, the M_2 tide (on the continental slope) was greater at the southwestern (80-1) mooring ($89 \times 10^3 \ cm^2 \ s^{-2} \ cph^{-1}$) than at the northeastern (80-2) mooring ($86 \times 10^3 \ cm^2 \ s^{-2} \ cph^{-1}$). The cause of this cross-canyon decrease in M_2 tidal amplitude is not known, but may be related to the absence of this signal in a current meter record obtained downstream of a southeastern Grand Bank canyon (Robe, 1975).

4.5 1981 CTD data

CTD station locations are plotted in Figure 4.1. The positions, times, and depths of these stations are listed in Table B2 in Appendix B. Only 7 CTD casts were possible due to high winds.

4.5.1 Temperature, salinity and σ_t sections

Vertical cross-sections of temperature (Figure 4.21), salinity and density (Figure 4.22) were derived from one transect along the axis of Carson Canyon on 11 June, 1981, between 1500 and 1643 GMT. The Labrador Current cold core (the region bounded by the $-1 \ ^\circ C$ isotherm) is evident in Figure 4.21 and the salinity is about 33.0 ppt at the depth corresponding to the cold core (about 80 m). The σ_t section is included here to illustrate the equivalence of isohalines and isopycnals. The CTD

data used in the 1981 sections (Figures 4.2) and 4.22) were obtained during the period in which the central axis upper meter (at a depth of 168 m) registered flow towards the secondary head, counter to the mean direction of the Labrador Current (Figure 4.14). The mean temperature and salinity values taken from the SLP filtered records of the central axis upper meter (see Figure 4.7) at this time were respectively 1.3 °C and 34.1 ppt.
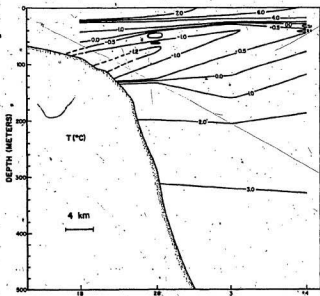
FIGURE 4.21: Central Axis temperature section for 11 June, 1981.
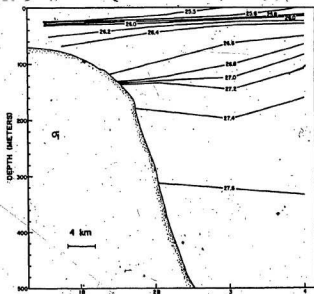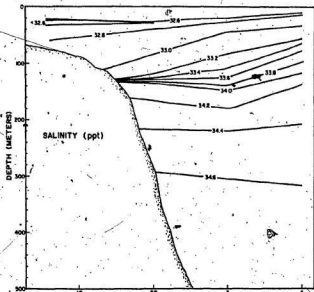
FIGURE 4.22: Central Axis salinity (top) and σ_t (bottom) sections for 11 June, 1981.

Generally, temperatures and the vertical temperature gradient below the cold core (Figure 4.21) are greater than for the 1980 central axis temperature section (Figure 3.9). Those isotherms > 0° C below 100 m depth slope upwards towards the canyon head. In addition, the Labrador Current cold core in 1981 (Figure 4.21) does not extend as far down-canyon as it did in the 1980 section. Nor does the cold core observed in 1981 intersect that location near station 25 (see Figure 3.1) which was estimated to be near the position of the velocity core.

The salinity section for 1981 (Figure 4.22) differs significantly from the central axis salinity section for 1980 (Figure 3.11). Below 100 m the salinities are generally greater and the isohalines which are > 33.8 ppt slope upwards from the center of the canyon at station 3 to the head at station 28. The reversal in slope is not thought to be caused by tidal aliasing because the transect was completed in only 2.75 h. At depths shallower than 100 m, the temperature and salinity transects resemble more closely those from 1980, especially at the shelf break.

Figure 4.23 is a profile of temperature and salinity from a CTD cast prior to the upwelling event at 1400 h, 6 June at mooring 81-2 (see Figure 4.1). Salinities from Figure 4.23 are compared in Table 4.3 with salinities measured by the central axis upper meter in order to estimate the upper limits of vertical velocities during the upwelling event. Values for the central axis upper meter were taken from the despiked listing. The first two lines of data in Table 4.3 show that the measurements obtained by the two instruments are consistent. The arrival times of isohalines at the current meter, and the vertical separation of these same isohalines in the CTD profile, are used to calculate rates of isohaline ascent. The values are not interpreted as being representative of vertical velocities.
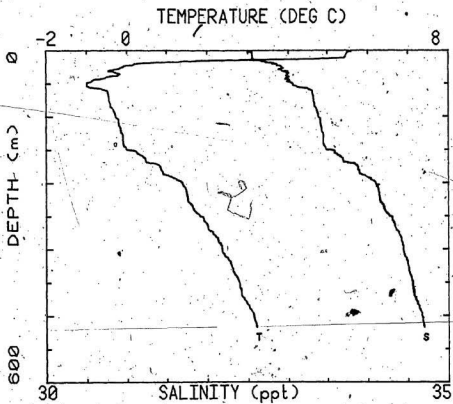
FIGURE 4 23: Vertical profile of temperature (T) and salinity (S) at station .81-2 from the CTD cast of 6 June, 1981.

because the advective contribution to the rate of salinity increase is unknown.

TABLE 4.3: Comparison of temperature and salinity measurements
by the CTD and the central axis upper meter (CAU) at mooring 81-2

Instrument	Temp (°C)	Sal (ppt)	Pres (dbar)	GMT/Date
CTD 81-2	-0.10	33.45	167	1354/6 June
CAU	-0.10	33.46	167	1335/6 June
CTD 81-2	+0.07	33.55	180	1354/6 June
CTD 81-2	+1.58	34.18	277	1354/6 June
CAU	+0.08	33.57	167	1255/9 June
CAU	+1.41	34.18	167	0340/10 June
CTD 81-2	+0.07	33.55	180	1354/6 June
CTD 81-2	+1.12	33.99	229	1354/6 June
CAU	+0.08	33.57	167	1255/9 June
CAU	+0.96	33.99	167	1525/9 June

A peak ascent rate of 0.5 cm s^{-1} is found from the bottom four lines in Table 4.3 using the amount of time taken (2.5 h) for the 33.99 ppt isohaline to undergo a 49 m (229 - 180 m) vertical displacement on June 9. A similar calculation for the 34.18 ppt isohaline results in a mean ascent rate of 0.2 cm s^{-1} for the upwelling of intermediate depth water on June 9 and 10. Ascent rates might possibly be greater at the other moorings where larger amplitude and more rapid increases than at mooring 81-2 were recorded (compare Figures 4.2, 4.3 and 4.5).

CTD stations 1A and 2A (Figure 4.1) were occupied one day earlier, but in the same locations respectively as stations 1B and 2B used in the sections (Figures 4.21-4.22). Temperature and salinity profiles collected at station 2A (Figure 4.1) at 1419 h on 10 June, 1981, are presented in Figure 4.24a. Figure 4.24b shows similar profiles for the CTD data collected at station 1A at 1256 h, also on 10 June. The two temperature
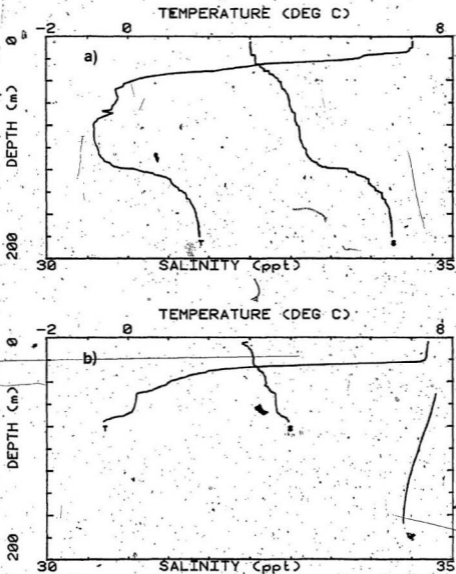
FIGURE 4.24: Vertical profiles of temperature (T) and salinity (S) from CTD casts on 10 June, 1981, at a) station 2A and b) station 1A.

profiles in Figure 4.24 are of particular interest because they show no Labrador Current cold core water (≤ -1 °C) at the head of Carson Canyon, even though one day later, on 11 June, the cold core possesses an observed thickness of 40 m (Figure 4.21) at station 18.

4.5.2   Dynamic heights and geostrophic velocity profiles

The dynamic heights calculated for the 5 dbar surface relative to 200 dbar from CTD data collected on June 8 (station 81-2 only) and June 11, 1981, are listed in Table 4.4.

TABLE 4.4: Dynamic heights for June, 1981

Station	Dynamic Height (dyn cm)
18	94
2B	93
81-2	93
3	91
4	88

The range of values in Table 4.4 (88 – 94 dyn cm) is not grossly different from that indicated by Figure 3.14 for the 1980 dynamic topography along the canyon axis. As in 1980, the dynamic heights for 11 June 1981 are seen to decrease away from the shelf break when referenced to the station locations shown in Figure 4.1, implying geostrophic flow to the southwest. This direction is opposite to the ≈ 10 cm s^{-1} northeastward flow measured by the central axis upper meter (Figure 4.11) at mooring 81-2 over the same period.

A vertical profile of geostrophic velocity for the pair of CTD stations 2B-3 (the solid line in Figure 4.25a) is used to investigate this discrepancy. The line between these two stations intersects mooring 81-2 (Figure 4.1). Note the existence of a distinct, 4.4 cm s^{-1} counter current at 130 m and positive (southwestward) geostrophic velocities above 100 m. The major differences between this profile and the corresponding profile for the 1980 station pair 23B-24 (the dashed line in Figure 4.25a) at the head of the canyon (locations are given in Figure 3.1) are this counter current and the significant velocity decreases at all depths above 100 m in 1981. These observations therefore show that the Labrador Current was present at the central axis during the reversal at mooring 81-2 on 11 June, but with reduced speeds and displaced upwards by a counter current.

A geostrophic velocity profile for the 1981 station pair 3-4 (the solid line in Figure 4.25b) further down-slope from mooring 81-2, and along the central axis of Carson Canyon bears little resemblance to the corresponding profile from the 1980 station pair 24-26 (the dashed line in Figure 4.25b). The near doubling of the surface current in 1981 suggests a seaward shift of the velocity axis of the Labrador Current.
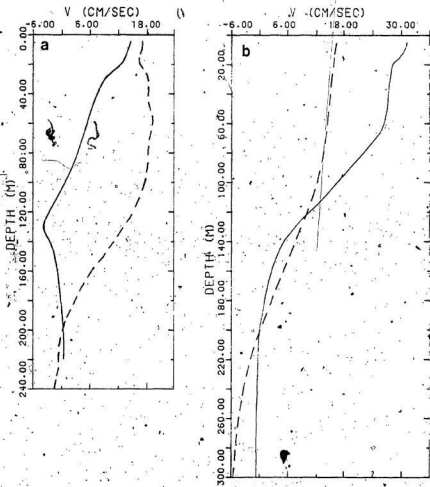
FIGURE 4.25: Vertical profiles of geostrophic velocity between CTD stations: a) 2B and 3 (of 1981, solid line) and 23B and 24 (of 1980, dashed line), and b) 3 and 4 (of 1981, solid line) and 24 and 26 (of 1980, dashed line).

CHAPTER 5   THE MEAN FLOW

In this chapter, the steady-state mean flow of the Labrador Current at Carson Canyon is analyzed. Important observations with respect to the mean flow are summarized first, using selected data from 1980 and 1981 to define a mean circulation pattern in the upper layer. Figure 3.14 gives the dynamic topography of the 5 dbar surface relative to 200 dbar for the 1980 survey. Although ageostrophic effects are important, as shown later in this chapter, and therefore affect the interpretation of Figure 3.14 as a streamline pattern, several features of the mean circulation are inferred from the combination of the dynamic topography with the measured mean currents. Figure 5.1 gives the composite mean current vectors from 1980 (Figure 3.6) and 1981 (from the 7 June plot of Figure 4.14). The 1981 measurements precede the upwelling event. The mean currents up- and downstream of the canyon (moorings 80-2 and 80-1) are predominantly along-isobath as is the dynamic topography (Figure 4.14) in the same regions. This result is consistent with findings by others at points removed from canyons along the southeastern Grand Bank (Kudlo et al. 1979; Mountain 1980). There is, however, an upslope deflection of the mean current at mooring 80-2 and the dynamic topography also shows a shelfward turning directly upstream of the canyon, which may represent an upstream, canyon-induced disturbance (Chapter 3). Cross-isobath flow over the northeastern wall, at and seaward of the secondary head, is indicated at mooring 81-3 and by the dynamic topography < 92 dyn cm. The mean flow at the 1981 southwestern mooring (81-1) is predominantly parallel to the southwestern wall, which is consistent with the along-isobath flow around the head and along the southwestern wall implied by the 92 and 93 dyn cm contours. The mean current at the central axis mooring
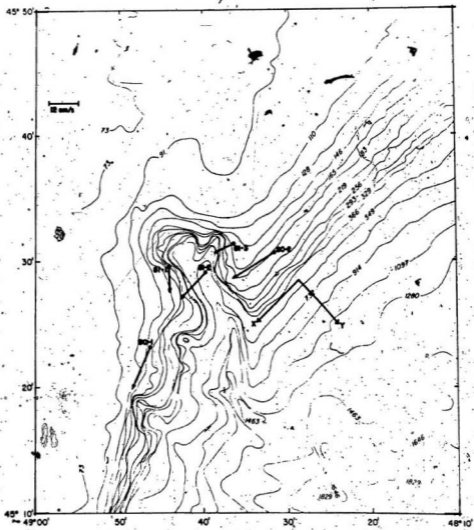
FIGURE 5.1: Vector plots of the mean, steady state currents at the 1980 and 1981 moorings, and the coordinate system for the mean flow analysis

(81-2) is cross-canyon, approximately tangential to the contours of dynamic height. Wave-like features are present in the dynamic topography in the lee of the canyon. Toward the canyon mouth in deep water, relatively unperturbed, cross-canyon flow is indicated by the dynamic topography < 89 dyn cm.

Finally, the 1980 CTD sections show that the cold core of the Labrador Current bifurcates at the canyon (Figures 3.9 and 3.10). The warmer water separating the two cores is located downstream of the secondary head. Furthermore, a net near-bottom drift of 0.9 cm s^{-1} toward the secondary head, both prior to and subsequent to the upwelling event in 1981, was observed at the central axis lower meter (Figure 4.12).

These observations combine to produce a consistent mean flow pattern, of which the principal characteristics are: predominantly along-isobath flow in the far field up- and downstream of the canyon, cross-isobath and cross-canyon flow at the northeastern wall and central axis, along-isobath flow at the head and at the southwestern wall, wave-like features in the canyon lee, splitting of the cold temperature core, and a deep return flow toward the secondary head at the central axis.

In this chapter, after comparing the measured and geostrophic velocities, the importance of bottom friction to the current measurements is estimated. Then, explanations for the existence of the principal features of the mean flow (listed above) are sought by examining the implications of the constraint imposed by potential vorticity conservation. Finally, the magnitudes of the non-linear and Coriolis acceleration terms in the central canyon region are estimated and compared.

5.1 The coordinate system; comparison of measured and geostrophic velocities

The coordinate system for the mean flow analysis (Figure 5.1) is aligned with the upstream bathymetry. The along-slope velocity component u is positive pointing toward 225 °T (+x) and the cross-slope component v is positive in the off-shelf direction toward 135 °T (+ y). Note that this system is distinct from the I (cross-isobath) and J (along-isobath) velocity component system used earlier.

Variations in the measured and geostrophic mean velocities are now compared. A representative estimate for variations of the mean speed at Carson Canyon is ±5 cm s⁻¹ (from the standard deviation of the SLP components for the 1980 current meters, Table A1 in Appendix A). The variation in the direction of the observed mean current is small: ±3° (see the SLP PVD's for 1980 in Figure A8 in Appendix A). The time variation in dynamic height at a single station in the central canyon region is 2 dyn cm (Figure 3.15). As discussed in Chapter 3, this is apparently due to a semi-diurnal internal tide, although the contribution from ship drift is unknown and could be significant. To the degree to which this observed variation is both real and representative of the area, the dynamic topography is likely to be tidally aliased. Nevertheless, the flow pattern inferred from the dynamic topography is consistent with the measured mean directions. Furthermore the variations in these directions are small. It is concluded that flow directions estimated from Figure 3.14 are not grossly in error.

It remains to make a direct comparison between geostrophic and measured velocities, which comparison will test the assumption of a 200 m level of no motion. Unfortunately, this comparison can be made only at

the southwestern (80-1) mooring, because the loss of salinity measure-
ments at station 4 (see Figure 3.1) precludes the possibility of obtaining a
reliable geostrophic estimate at the northeastern (80-2) mooring. The
measured velocity at 120 m depth at mooring 80-1 (approximately the
same location as station 37; see Figure 3.1) is 17.3 cm s^{-1} (from the
SLP mean components of Table A1, Appendix A), which yields a
16.1 cm s^{-1} component perpendicular to the line joining stations 37 and
38. The geostrophic velocities calculated at 120 m between stations 38
and 39 (13.6 cm s^{-1}), and stations 38 and 37 (14.3 cm s^{-1}), have
been linearly extrapolated to station 37. The result is 14.6 cm s^{-1} at
station 37, which is smaller than the measured value by only 9%. Part of
this difference may arise because the use of a 200 dbar depth of no
motion results in an underestimate of the geostrophic velocities. It must
be pointed out, however, that the geostrophic velocities represent averages
across a sheared jet between stations whose average spacing is
O(10 km). The observed agreement between measured and geostrophic
velocities may therefore be fortuitous.

5.2 Bottom friction

The Ekman layer depth δ_E is defined as $(2A_v / f)^{1/2}$ (e.g. Pedlosky
1979, p. 177). A_v is the vertical eddy viscosity coefficient and f is the
Coriolis parameter, which at Carson Canyon (45.5° N) is
1.04 × 10^{-4} s^{-1}. Gill (1982, p. 332) estimates δ_E by a quadratic drag
law for the bottom stress in terms of the interior geostrophic velocity
(defined here by the symbol U_G) such that,

$$\delta_E = 4 C_D U_G / f \qquad (5.1)$$

where an order of magnitude estimate of C_D is typically 2×10^{-3} (e.g. Csanady 1982, p. 12).

Estimates of U_G and δ_E for the northeastern meter (on the upstream, 80-2 mooring) have been calculated in the following manner. The velocity components in the bottom Ekman layer are (Pedlosky 1979, p. 178).

$$u = U_G \left[1 - e^{-z/\delta_E} \cos(z/\delta_E) \right] \qquad (5.2a)$$

and,

$$v = U_G \, e^{-z/\delta_E} \sin(z/\delta_E) \qquad (5.2b)$$

where $z = 0$ at the sea floor. The speed, R, is therefore given by $\sqrt{u^2 + v^2}$, or,

$$R = U_G \left[1 + e^{-2z/\delta_E} - 2e^{-z/\delta_E} \cos(z/\delta_E) \right]^{1/2}. \qquad (5.2c)$$

(Note that the definition of $\delta_E = \left[\frac{2 A_v}{f} \right]^{1/2}$ is different from that used by Armi and Millard (1976), who used the height (D_E) at which the speed in the bottom boundary layer was 99% of, and in the same direction as, the interior flow. That is, $R = 0.99 \, U_G$. For comparison, at $z = \delta_E$, $R = 0.86 U_G$ and is directed at an angle of 21° to the left of the interior flow, and $D_E = 5\delta_E$.) Substituting for δ_E using (5.1) with $z = 10$ m, $R = 19.5$ cm.s^{-1} (the SLP mean components from Table A1), and $C_D = 2 \times 10^{-3}$, equation 5.2c becomes.

$$0.195 = U_G \left[1 + e^{-1/4U_G} - 2e^{-1/8U_G} \cos(1/8U_G) \right]^{1/2}. \qquad (5.3)$$

This equation can in principle be solved iteratively for U_G, for which δ_E

can be then obtained using equation 5.1. Table 5.1 was constructed by following this procedure for different values of C_D. The values in Table 5.1 are therefore the geostrophic velocities and Ekman layer thicknesses required to give the observed speed of 19.5 cm s^{-1} at 10 m above bottom. The directions were obtained using equations 5.2a and 5.2b. Note that the right hand side of equation 5.3 has a maximum value of 0.177 which is approached for values of $U_G > 100$ cm s^{-1}. Therefore, equation 5.2c cannot be satisfied for $C_D = 2 \times 10^{-3}$ and $R = 19.5$ cm s^{-1}.

TABLE 5.1: Geostrophic velocities, U_G, Ekman layer depths, δ_E, and deflection angles (positive is to the left and down-slope) for the 1980 northeastern meter at $z = 10$ m.

$C_D \times 10^3$	U_G (m/s)	δ_E (m)	Angle (degrees)
> 1.7	-	-	-
1.6	0.495	30.0	36.0
1.4	0.312	17.0	30.0
1.2	0.240	11.0	23.0
1.0	0.203	7.8	16.0
0.9	0.194	6.7	13.0
0.8	0.187	5.7	9.6
0.7	0.183	4.9	6.3
0.6	0.182	4.2	3.4
0.5	0.184	3.5	1.0
0.4	0.189	2.9	-0.52
0.3	0.194	2.2	-0.64

The larger ($> 10°$) deflection angles in Table 5.1, which correspond to $C_D > 0.8 \times 10^{-3}$, are to the left of the interior geostrophic flow, and were this interior flow to be approximately along-isobath as expected (see the next section), would result in a large downslope component of velocity at 10 m above bottom, in contradiction with observations. The smaller (-1 to $6°$) deflection angles correspond to low values of C_D and values of $\delta_E < 5$ m. Similar Ekman layer thicknesses are reported in the literature.

For example, a value of 2.94 m was derived by Janowitz and Pietrafesa (1980) in a barotropic model of the time-dependent response in the shelf-slope region to a uniform applied wind-stress. In the limit of long times, the predicted interior geostrophic velocity parallel to the slope was found to be time-independent and equal to 19 cm s^{-1}. Using (5.1), this geostrophic velocity and 2.94 m Ekman layer thickness gives 0.3 x 10^{-3} for the value of C_D ($f = 0.8$ x 10^{-4} s^{-1}). In the remainder of this chapter it will be assumed that δ_E < 5 m, and that as a result, the measured currents effectively represent the interior geostrophic flow. Although this requires rather low values of C_D (~ 0.5 x 10^{-3}), comparable values have appeared in the recent literature. Moreover, Csanady (1982, p.12) states that C_D is known to within an order of magnitude at best. Therefore, in the absence of velocity measurements distributed in the vertical to demonstrate otherwise, the additional complications associated with including friction in the analysis are probably unwarranted.

5.3 The velocity field upstream of Carson Canyon

Observations of the velocity field upstream of Carson Canyon are now analyzed in terms of the potential vorticity of the flow. According to direct current measurements at mooring 80-2 (Figure 5.1), the mean, near shelf-break speed of the Labrador Current is 19 cm s^{-1} at 10 m above bottom along the 170 m isobath. The maximum velocity of the Labrador Current is estimated to be 48 cm s^{-1} from the 1980 CTD pair 10-8 assuming geostrophy and a depth of no motion at 200 m (Chapter 3). The velocity axis coincides with the seaward half of the cold core (Figure 3.9, top) and the 500 m isobath (Figure 3.14).

An estimate for the cross-stream variation of the mean velocity is needed at this point because it determines the magnitude of the relative vorticity, which itself partly determines whether or not the mean flow will follow the isobaths. It cannot be reliably obtained from the dynamic topography because the station spacing is so large. An expression for the cross-stream velocity profile of a free jet is therefore derived, and its applicability to the Labrador Current discussed later.

The vertically integrated, horizontal momentum equations for a two-layer system in which the upper and lower layers move at speeds u and u' in geostrophic equilibrium are, for the upper layer

$$f \, u = -g \, \eta_y \tag{5.4}$$

and for the lower layer

$$f \, u' = -g \, \eta_y - g' \, \eta'_y \tag{5.5}$$

where the subscript y denotes differentiation with respect to y, the cross-stream coordinate. η is the sea surface elevation, η' is the elevation of the interface between the two layers, $g' = \dfrac{\rho' - \rho}{\rho'} g$, and the density ρ' in the lower layer is greater than the density ρ in the upper layer. (A similar representation is shown schematically in Figure 6.1.) The equilibrium thicknesses of the upper and lower layers are $h + \eta - \eta'$ and $h' + \eta'$, where h and h' are constants. The potential vorticity (e.g. Gill 1982, pp. 232 – 233 and p. 235) is, for the upper and lower layers respectively:

$$\frac{\zeta + f}{(h + \eta - \eta')} \tag{5.6}$$

and

$$\frac{\zeta' + f}{(h' + \eta')} \tag{5.7}$$

where $\zeta = -u_y$ and $\zeta' = -u'_y$ are the relative vorticities in the upper

and lower layers, since the cross-stream velocities are assumed to be zero. Stommel (1965, pp. 108 – 109) showed that the potential vorticity is nearly uniform across the Gulf Stream. The assumption is made here that this is also true of the Labrador Current, although it cannot be justified in terms of the measurements presented here. Discussion returns to this point later. Consequently, the potential vorticity of each layer, uniform in the cross-stream direction, is equal to the constant value $\frac{f}{h}$ in the upper layer and $\frac{f}{h'}$ in the lower layer outside the jet where the velocity is zero. Equating the potential vorticities (5.6) and (5.7) in each layer with their uniform values outside the jet region, the following relations are found for the upper and lower layers respectively:

$$-u_y = \frac{f}{h}\left[\eta - \eta'\right] \quad \text{and} \tag{5.8}$$

$$-u'_y = \frac{f}{h'}\eta' \tag{5.9}$$

The difference velocity $\hat{u} = u - u'$ is found in terms of η' by subtracting (5.5) from (5.4),

$$\hat{u} = \frac{g'}{f}\eta'_y \tag{5.10}$$

Subtracting (5.8) from (5.9), making the approximation $\eta \ll \eta'$, differentiating the result with respect to y, and then substituting $\hat{u}$ for η'_y from (5.10) yields

$$\hat{u}_{yy} = \frac{f^2}{g'\left[\frac{hh'}{h+h'}\right]}\hat{u} \tag{5.11}$$

With the assumption that the jet is restricted to the upper layer ($u' \ll u$), u replaces $\hat{u}$ in (5.11), which may then be integrated to give

$$u = U_0\, e^{-|y|/R_i} \tag{5.12}$$

Here, U_o is the maximum speed of the jet at its axis ($y = 0$) and R_l is the internal Rossby radius of deformation, given by,

$$R_l = \frac{\sqrt{g \cdot \frac{hh'}{h+h}}}{f} = \frac{c'}{f} \qquad (5.13)$$

for two-layer flow, where $c' = \sqrt{g \cdot \frac{hh'}{h+h}}$ is the (first baroclinic mode) long interfacial wave speed (Gill 1982, p. 207).

Equation 5.12 will now be applied to the Labrador Current, choosing the origin of the y-axis to be at the 500 m isobath, the approximate location of the velocity axis, as shown in Figure 5.1. Table 5.2 presents values of R_l estimated from the CTD data using equation 5.13. A typical value of R_l is 8.0 km. The line segment perpendicular to the continental slope between mooring 80-2 and 500 m depth northeast of Carson Canyon is 8.0 km long (see Figure 5.1). Employing $R_l = 8.0$ km, $y = 8.0$ km, the speed estimate $U_o = 48$ cm s^{-1}, and equation 5.12, the estimated speed at mooring 80-2 is $u = 18$ cm s^{-1}. This is within 6% of the measured speed (19 cm s^{-1}).

Using the above results, the cross-stream shear near the shelf break is estimated to be $|\zeta| = \left|\frac{-\partial u}{\partial y}\right| = \frac{u}{R_l} < \frac{18 \text{ cm s}^{-1}}{8 \text{ km}} = 2.2 \times 10^{-5}$ s^{-1}. This may be an upper limit. A decrease in shear on the shelf side of the Labrador Current has been reported by Hill et al. (1973). Their Figure 5(a) for the geostrophic current contours for a section across the slope about 30 km south of Carson Canyon shows an asymmetry between the two sides of the velocity core with greater shear on the left hand side of the Labrador Current looking downstream. It is concluded that $|\zeta| \ll f$ in the vicinity of the shelf break upstream of the canyon.

TABLE 5.2: R_i estimated from CTD data by equation 5.13

CTD Station	$\frac{\rho' - \rho}{\rho} \times 10^{-4}$ *	$h + h'$ ** (meters)	R_i † (kilometers)
1980			
10	7.38878	400	8.2
11	6.98897	550	9.0
14	4.00971	550	6.8
15	4.68144	640	7.6
16	4.36989	690	7.5
25	5.03203	870	8.4
26	4.73981	1180	8.4
38	4.24375	500	6.5
1981			
81-2	7.49582	600	9.5

* $\bar{\rho}$ taken at 150 m.
ρ' taken at deepest level of cast (normally 500 m).
**$h = 200$ m is the level of no motion and
$h + h'$ = bottom depth.
† the mean of all casts is $R_i = 8.0$ km.

The flow near the shelf break upstream of the canyon appears to be nearly barotropic. This is suggested by the close agreement between the measured velocity 10 m above bottom and the interior geostrophic velocity at the 1980 northeastern meter calculated from equation 5.12. Furthermore, the downward sloping isohalines > 33.2 ppt intersect the bottom well below the shelf break (Figures 3.11 and 3.12). This indicates reduced horizontal density gradients close to the shelf break (isohalines being approximately equivalent to isopycnals), which implies a decrease in the vertical shear because of the thermal wind equation (e.g. Gill 1982, p. 217). Hill et al. (1973) report an 18 cm s^{-1} barotropic flow at ~ 130 m depth northeast of Carson Canyon (also see Chapter 1).

Under barotropic conditions, $\left[\dfrac{\zeta + f}{D_o + \eta} \right]$ is the potential vorticity, where D_o is the water depth (e.g. $D_o = D_o(y)$ is the depth upstream of

Carson Canyon). For hydrostatic (i. e. shallow water) motion in the absence of friction, potential vorticity is conserved along a pathline. That is,

$$\frac{d}{dt}\left[\frac{\zeta + f}{D_0 + \eta}\right] = 0 \qquad (5.14)$$

where $\frac{d}{dt} = \frac{\partial}{\partial t} + u\frac{\partial}{\partial x} + v\frac{\partial}{\partial y}$. It is noted at this point that this provides some justification for the use of uniform potential vorticity in the previous model: that, in the light of (5.14), cross-stream mixing would cause the time-averaged potential vorticity to be uniform. For steady flow, pathlines and streamlines are equivalent, and ζ in natural coordinates along a streamline is given by (Gill 1982, p. 235),

$$\zeta = \frac{-\partial U}{\partial r} - \frac{U}{r} \qquad (5.15)$$

Here U is the speed of a fluid column along the streamline, and r is the local radius of curvature of the streamline. The signs are chosen for rightward curvature and $\frac{\partial U}{\partial r} > 0$, as appropriate to the right hand side of the Labrador Current looking downstream, and the northeastern side of the canyon. Negative vorticity is associated with the cross-stream shear and the rightward curvature of the flow. The conditions for which along-isobath flow may be maintained while conserving potential vorticity, are found by scaling ζ with respect to f. Consequently, dividing equation 5.15 by f defines two Rossby numbers: the shear Rossby number $R_0' = \left|\frac{-\partial U}{f\ \partial r}\right| = \frac{U}{R_f}$ by equation 5.12, and the curvature Rossby number $R_0'' = \left|\frac{U}{fr}\right|$. For small R_0' and large radii of curvature, $|\zeta| \ll f$ and, provided $\eta \ll D_0$, equation (5.14) requires that $\vec{u} \cdot \vec{\nabla} D_0 = 0$. Therefore, the flow is along-isobath. If R_0' or R_0'' become large, then conservation of potential vorticity no longer implies along-isobath flow.

Upstream of Carson Canyon, $r \to \infty$, and therefore $R''_o \ll 1$. Using the estimates obtained above, $R_o' \leq 0.22 < 1$ near the shelf break. The flow should therefore be approximately along-isobath. It can also be shown (Gill 1982, p. 235) that under these conditions the flow at the shelf break upstream is geostrophic.

5.4 Disturbances of the mean flow by the canyon

For a baroclinic jet like the Labrador Current in the upper layer of a two-layer system, the extent to which the jet responds to changes in the underlying topography depends on the depth of, and stratification in, the layer of water between the bottom and the jet. For example, consider the two-layer representation of the Labrador Current at Carson Canyon in Figure 5.2. For $f = $ constant, conservation of potential vorticity for steady flow in a two-layer fluid, in the limit of small Rossby number, reduces to (Pedlosky 1979, pp. 386 – 394),

$$\left[u_o \frac{\partial}{\partial x} + v_o \frac{\partial}{\partial y} \right] \left[\zeta_o + \frac{f}{h} \eta'_o \right] = 0 \qquad (5.16)$$

$$\left[u' \frac{\partial}{\partial x} + v' \frac{\partial}{\partial y} \right] \left[\zeta'_o - \frac{f}{h'} \eta'_o + \frac{f}{h'} (D - D_o) \right] = 0 \qquad (5.17)$$

where primes refer to the lower layer; and the zero subscripts indicate the values of the variables in the geostrophic limit, excepting $D_o(y)$ which is the depth upstream. Clearly, the terms in the square brackets are constant along streamlines. It is also clear that if there is no flow in the lower layer, no vertical velocities will arise from changes in topography and therefore the bottom boundary condition cannot influence the shape of the interface. In this case, the flow is along isopleths of η'_o provided $\zeta_o \ll \frac{f}{h} \eta'_o$, and η'_o does not intersect the bottom. Examining Figure 5.2, this argument suggests that because the interface slopes downward

toward the shelf, the Labrador Current will be influenced by canyon topography in varying degrees as a function of the off-shelf coordinate, y. Three regions of the canyon are defined in Figure 5.2. In the upper canyon region (UR), corresponding to the head, the flow is approximately barotropic, but with lower speeds due to cross-stream shear. The central canyon, or transition region (TR), is in the vicinity of the intersection of $z = -h + \eta'_o$ with the bottom, where the flow will begin to be influenced by the stratification. In the lower canyon region (LR), which extends seaward of the transition region, the bottom lies well below the interface.
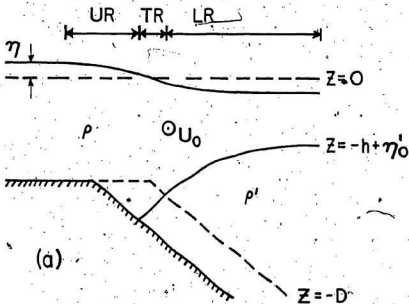
FIGURE 5.2: Two-layer representation of the Labrador Current at Carson Canyon.

Consider the upper canyon region. The radii of curvature of the iso-baths between ≈140 m and the shelf break (110 m) at and immediately upstream of the head are sufficiently large that the mean flow should be along-isobath. For example, typical values of the radii of curvature for the 128 m isobath are 7.5 km at the head and 11 km upstream of the head. According to equation 5.12, the speed and cross-stream shear at the 128 m isobath, using 10.5 km as the distance between the 128 m and 500 m isobaths upstream of the canyon, are 13 cm s^{-1} and 1.6 × 10^{-5} s^{-1} respectively. Therefore, R_o' = 0.16 and R''_o < 0.17 at the 128 m isobath. Because R_o' and R''_o are both small, it is sug-gested that the mean current is along-isobath at depths < 140 m at the head of Carson Canyon, as indicated by the dynamic topography (Figure 3.14), although no current meter data are available to support this.

The region shellward of the head (e.g. of the 110 m isobath) in Fig-ure 3.14 is somewhat perplexing. The contours of dynamic height cross isobaths, and speeds upstream appear to increase in the on-shelf direc-tion. These effects may be artifacts of the extrapolation of dynamic heights into this shallow region using the method of Reid and Mantyla (1976).

In the transition region, cross-isobath and cross-canyon flow were observed at moorings 81-2 and 81-3 (Figure 5.1). These directions are consistent with the local dynamic topography (Figure 3.14). The radii of curvature of the isobaths on the northeast side of Carson Canyon (Figure 5.1) are <2 km between approximately the 146 m and 914 m isobaths at about 48° 35′ W. Selection of these radii as length scales yields R''_o > 1 when U = 20 cm s^{-1}. This suggests that the relative vorticity associated with the curvature of the path would become too large for

steady along-isobath flow to be maintained (e.g. $\vec{u} \cdot \nabla \theta_{o} = 0$ in equation 5.14), consistent with the observations.

The theory of flows over topographic depressions is not well-developed. In contrast, flows over raised topographic features have been studied extensively (see the reviews by Hogg, 1980; Smith, 1979). Smith (1979; see also Gill 1982, pp. 274 - 283) discusses the effects of stratification on the horizontal deflection of winds caused by a mountain ridge where rotation is important. There is a leftward deflection of isobars and streamlines beginning upstream; pronounced ageostrophic (cross-isobar) flow in the region over the ridge; and a stationary lee wave in the pressure field with a wavelength comparable to the width of the ridge. The equivalent problem for an infinite trench does not appear to have been studied, but similar phenomena are to be expected, although with differences arising from the changes in the vortex column lengths being of different sign. For example, Batchelor (1967, pp. 573 - 574) shows that downstream of a ridge, a uniform barotropic flow is deflected to the right of its upstream direction; the same flow over a trench would be deflected to the left. It is tempting to suggest that the rightward turning of the dynamic height contours upstream of Carson Canyon and the wave-like pattern in the dynamic topography in the lee of the canyon axis are the result of a response similar to that presented by Smith (1979), but in the opposite sense. The wave-like features may, however, be associated instead with the small unnamed canyon immediately downstream of Carson Canyon (Figures 3.1 and 3.14).

The velocity axis of the Labrador Current lies within the lower canyon region (LR, Figure 5.2) wherein the thick lower layer effectively isolates the upper layer flow from the topography. Accordingly, the dynamic

topography > 89 dyn cm (Figure 3.14) indicates undisturbed. cross-canyon flow in this region.

5.5 The momentum balance in the central canyon region

The measurements to be employed, are the 1981 mean currents prior to the upwelling event shown in Figure 5.1. The u and v components of these velocities are presented below in Table 5.3.

TABLE 5.3: u and v components of velocity for 7 June, 1981.

Mooring	Meter	u (cm s^{-1})	v (cm s^{-1})
81-1	southwestern	6.7	6.8
81-2	central axis upper	14.6	-0.2
81-3	northeastern	8.2	-3.1

Values for the non-linear terms in the horizontal momentum equations were obtained with respect to the central axis mooring using the velocities from Table 5.3 and the equations below. Subscripts are defined as; swn = southwestern, cau = central axis upper, nen = northeastern. Primes represent the distances between the southwestern and central axis moorings: $\Delta y'$ in the cross-slope direction (4.48 km). $\Delta x'$ in the along-slope direction (3.50 km). Δx is the separation (the along-slope distance) of the northeastern and central axis moorings (6.14 km). In the x-direction.

$$u \frac{\partial u}{\partial x} = u_{cau} \left[\frac{u_{cau} - u_{nen}}{\Delta x} \right] = 15 \times 10^{-5} \text{ cm s}^{-2} \qquad (5.18a)$$

$$v \frac{\partial u}{\partial y} = v_{cau} \left[\frac{u_{swn} - u_{cau}}{\Delta y'} - \frac{\partial u}{\partial x} \frac{\Delta x'}{\Delta y'} \right] = -0.7 \times 10^{-5} \text{ cm s}^{-2}. \quad (5.18b)$$

and in the y-direction.

$$u \frac{\partial v}{\partial x} = u_{cau} \left[\frac{v_{cau} - v_{nen}}{\Delta x} \right] = 7.0 \times 10^{-5} \text{ cm s}^{-2} \qquad (5.18c)$$

$$v \frac{\partial v}{\partial y} = v_{cau} \left[\frac{v_{swn} - v_{cau}}{\Delta y'} - \frac{\partial v}{\partial x} \frac{\Delta x'}{\Delta y'} \right] = 0.3 \times 10^{-5} \text{ cm s}^{-2} \quad (5.18d)$$

For comparison, the Coriolis accelerations are, for the x-direction,

$$-fv_{cau} = 2.1 \times 10^{-5} \text{ cm s}^{-2}$$

and in the y-direction,

$$fu_{cau} = 150 \times 10^{-5} \text{ cm s}^{-2}.$$

It is clear that in the off-shelf (y) direction, the non-linear terms are negligibly small in comparison with the Coriolis acceleration at the central axis mooring. In the cross-canyon direction on the other hand, the $u \frac{\partial u}{\partial x}$ term is an order of magnitude larger than either the Coriolis acceleration or the other non-linear term. Provided friction is not important, this suggests that in the steady state, the momentum balance in the cross-canyon direction is between the non-linear term and the pressure gradient, and is geostrophic in the off-shelf direction along the canyon axis.

5.6 The splitting of the cold core and possible steady upwelling

The warmer water separating the two cold cores at the central axis appears at stations 23B and 28 (Figures 3.9 and 3.10), which are down-stream of the secondary head (Figure 3.1). This suggests that the source of the warmer water is in the vicinity of the secondary head. In Section 5.4, it was suggested that along-isobath flow is maintained during the turn around the lip of the canyon on the shelfward side of the secon-

dary head. but that cross-isobath flow occurs across the northeastern wall seaward of the secondary head. This may result in a horizontal diver- gence at the secondary head. which one would expect to cause a decrease in the vertical thickness of the cold core. Further, such a divergence would result in steady local upwelling of the warm water needed to divide the cold core. Evidence to support this interpretation may be the deep. 0.9 cm s^{-1} drift toward the secondary head registered by the central axis lower meter before and after the upwelling event (Figure 4.12). which could represent a compensating flow driven by the steady upwelling.

Two processes will probably result given that there is persistent upwel- ling at the secondary head: 1). mixing of deep water into the Labrador Current; 2) other upwelling processes would possibly be enhanced (e.g. Blanton, Atkinson, Pietrafesa and Lee 1981) at the secondary head. That the temperature and salinity increases during the 1981 upwelling event were first observed at the northeastern meter (Chapter 4) may be evidence of this enhancement.

5.7 Comparison with other canyons

The circulation at Carson Canyon is dominated by the cross-canyon flow of the Labrador Current. Since this current flows with shallow water to its right. Isopycnals slope downward toward the shelf, leading to the dynamical framework discussed in the preceding sections and sketched in Figure 5.2. It is perhaps not surprising, therefore, that the results of other canyon studies have been difficult to apply directly to this system. Mountain, Coachman and Aagaard (1976) report that barometric pressure drives the up- and down-axis flows observed at Barrow Canyon in the

Chukchi Sea. Unlike the situation at Carson Canyon, however, where the circulation is dominated by the cross-canyon flow of the Labrador Current, Barrow Canyon's axis is parallel to the major current directions of the area (Mountain, 1983, personal communication).

The model reported by Mayer et al. (1982) for the interior flow at the head of the Hudson Shelf Valley applies only where the canyon axis is shallow ($\approx$ 70 m below the shelf) and the frictional bottom boundary layer is about 10 m thick. In that case, the boundary layer represents a significant fraction of the canyon depth, and therefore, bottom stress makes an important contribution to the dynamics. Along canyon flow is observed in the Hudson Shelf Valley and the model by Mayer et al. (1982) predicts a seaward flow along the central axis. Carson Canyon is much deeper and the frictional bottom boundary layer is probably < 5 m. Bottom stress is therefore probably less important to the Carson Canyon problem, and was ignored in the previous sections.

Below a certain depth in a canyon called the horizon by Mayer et al. (1982), a non-zero axial pressure gradient associated with the stratification may exist. This leads to an estuarine-like, headward flow in the deep layer of the Hudson Shelf Valley. Provided the cross-canyon length scale is small enough, the pressure gradient in the lower layer is balanced by bottom stress (Mayer et al. 1982). Cannon (1972) reports that the same balance exists in Juan de Fuca Canyon. Carson Canyon is wide at the central axis mooring position and the Coriolis term would probably cause a rightward amplification of a deep baroclinic current in the up-canyon sense. Nevertheless, this effect may provide an alternate explanation for the observed residual flow toward the secondary head.

Freeland and Denman (1982) have modeled residual up-canyon flow

and steady upwelling in Spur Canyon off Vancouver Island. Shelfward flow within the canyon is implied by the along-canyon pressure gradient associated with a persistent cyclonic gyre to the north of the canyon head and by the narrow canyon width which inhibits cross-canyon flow. Consequently, the along-canyon momentum balance (in accordance with the coordinate system of Figure 5.1 and with z increasing positively upwards from zero at the sea surface) is given as,

$$v \frac{\partial v}{\partial y} + w \frac{\partial v}{\partial z} = \frac{-1}{\rho} \frac{\partial p}{\partial y} \qquad (5.19)$$

where $\frac{\partial p}{\partial y}$ is the pressure gradient associated with the geostrophic flow above the canyon. This mean current flows cross-canyon, but with shallow water to the left, so that isopycnals slope up toward the shelf. Within the canyon, the pressure gradient induces shelfward flow (i.e. $v < 0$ in equation 5.19), and the condition that steady flow be parallel to the isopycnals,

$$\vec{u} \cdot \vec{\nabla} \rho = v \frac{\partial \rho}{\partial y} + w \frac{\partial \rho}{\partial z} = 0 \qquad (5.20)$$

therefore requires that steady shelfward upwelling occur. It is to be noted that this flow can be coupled to the shoreward transport in the bottom Ekman layer on the shelf, which is to the left of the mean current associated with the gyre.

Useful insights are gained by qualitatively applying the results obtained by Freeland and Denman (1982) and by Mayer et al. (1982) to Carson Canyon, assuming initially that within the canyon transverse flow is negligible. At Carson Canyon, the pressure associated with the geostrophic flow decreases off-shelf which, using (5.19), would imply a seaward current ($v > 0$) within the canyon. Because isopycnals slope upward away from the shelf (because the mean current flows with the shelf to its

right), equation 5.20 implies steady seaward upwelling along isopycnals. At Spur Canyon, the sloping bottom was represented by Freeland and Denman as a streamline parallel to the axis and the source for the upwelled water is inflow at the mouth from the Juan de Fuca Canyon. This approach meets with difficulty at Carson Canyon, because the isopycnals intersect the bottom. Furthermore, a source for the seaward, along isopycnal flow is required. This could be the seaward transport in the bottom Ekman layer beneath the Labrador Current on the shelf, or a return flow from deeper water along the canyon axis of the type discussed by Mayer et al. (1982). If it is assumed that the pressure gradient which drives the seaward upwelling drives the bottom flow as well, then the following relation gives the along-canyon momentum balance in the bottom boundary layer:

$$Q = \frac{-1}{\rho} \frac{\partial p}{\partial y} + A_v \frac{\partial^2 v}{\partial z^2} \qquad (5.21)$$

where $\frac{\partial p}{\partial y} < 0$. This balance necessarily implies offshore flow at the bottom. Suppose, however, that a "horizon", similar to that proposed by Mayer et al. (1982), forms the upper boundary to the bottom layer. At the horizon, the offshore pressure gradient is assumed to vanish. Equation 5.21 then implies shoreward flow in the bottom layer, since the pressure gradient is due solely to stratification.

An order of magnitude estimate of this shoreward flow can be obtained using the approach of Mayer et al. (1982). Assuming that the bottom layer is vertically mixed, then it follows that ρ is independent of z, and that the pressure below the horizon at some depth z is

$$p(z) = p(-D + \Delta) + \rho(y)g(-D + \Delta - z) \qquad (5.22)$$

where $D \equiv$ the bottom depth, $\Delta \equiv$ thickness of the bottom layer, and $(-D + \Delta)$ is the depth of the horizon. The axial pressure gradient is therefore

$$\frac{\partial p}{\partial y} = g \frac{\partial \rho}{\partial y} \left[(-D + \Delta) - z \right] \qquad (5.23)$$

since $\frac{\partial p}{\partial y}$ is assumed to vanish at the horizon. Substitution of (5.23) into (5.21) and transformation of the result using $\gamma = \frac{(-D + \Delta) - z}{\Delta}$, the dimensionless depth below the horizon, gives,

$$A_v \frac{\partial^2 v}{\partial \gamma^2} = \frac{g}{\rho} \frac{\partial \rho}{\partial y} \Delta^3 \gamma . \qquad (5.24)$$

Equation 5.24 is integrated subject to the boundary conditions: $\frac{\partial v}{\partial \gamma} = 0$ at $\gamma = 0$ (the shear stress is zero at the horizon), and $v = 0$ at $\gamma = 1$ (the no-slip condition at the bottom). Therefore, the flow in the bottom layer is,

$$v = \frac{g}{6 \rho A_v} \frac{\partial \rho}{\partial y} \Delta^3 (\gamma^3 - 1) , \qquad (5.25)$$

which is equivalent to the result given by Mayer et al. (1982). An estimate of the along-axis density gradient is obtained from the 34.6 and 34.7 ppt isohalines shown in the 1980, central axis salinity section of Figure 3.11 (bottom). These isohalines are about 4 km apart at the bottom, yielding a positive density gradient of 0.05×10^{-3} g cm^{-3} / 4×10^5 cm $= 1.25 \times 10^{-10}$ g cm^{-4}. Because the high frequency currents have amplitudes greater than the 0.9 cm s^{-1} residual (see the I component record in Figure 4.4), the eddy viscosity is estimated using the mean amplitude U_{av} of the high frequency currents; that is $A_v = 32 \times 10^{-2} U_{av}^2$ (Gill 1982, p. 332), which gives $A_v = 8$ cm^2 s^{-1} using $U_{av} = 5$ cm s^{-1}. It is not possible to estimate Δ from the Carson Canyon data. It seems reasonable, however, to take $\Delta = 10$ m as a

rough estimate of the thickness of this frictional bottom boundary layer. Evaluation of (5.25) at the horizon ($\Upsilon = 0$) yields a shelfward velocity of $v = -2.5$ cm s^{-1}, which is the same order of magnitude as the measured residual.

In summary, seaward upwelling below the lip of Carson Canyon may be supported by inflow from the bottom Ekman layer at the head of the canyon or by up-canyon flow in a density-driven frictional bottom layer. The latter interpretation is supported by the observation of the 0.9 cm s^{-1} drift toward the secondary head at 10 m above bottom. It is not clear, however, that the assumption of no cross-canyon flow is valid in Carson Canyon. This assumption depends on two conditions (Freeland and Denman 1982): 1) that the width of the canyon $< R_i =$ the length scale of the geostrophic flow above the canyon, and 2) that the walls be vertical. At Carson Canyon, condition 1) cannot be readily justified as an approximation because the width $\approx R_i \approx 8$ km and condition 2) is not immediately satisfied because of the $\approx$ 1:10 slope of the walls (Figure 1.2). As a comparison, $R_i = 17$ km $\approx 3 \times$ width of Spur Canyon, and Freeland and Denman question whether the 1:7 bottom slope of the walls at Spur Canyon is sufficiently close to vertical. Finally, it has also been suggested that the residual upcanyon drift might be driven by steady, topographically controlled upwelling in the vicinity of the secondary head.

CHAPTER 6 WIND-DRIVEN UPWELLING

During the upwelling event of 1981, a counter current existed beneath the southwestward flowing Labrador Current (see Chapter 4). The counter current was northeastward at the central axis upper meter, in the same direction as the peak wind stress (Figures 4.16 and 4.17). A current reversal at the southwestern (81-1) mooring and a near reversal at the northeastern (81-1) mooring occurred nearly simultaneously and 0.25 - 1 d earlier than increases in mean temperature (Figure 4.15) and salinity (compare Figures 4.6, 4.7 and 4.9). Further, the speeds started to decrease about 0.25 -0.5 d before the major changes in direction. The temperature and salinity increases at the northeastern mooring led those at the southwestern by about 0.5 d (Figure 4.15). Because the phase speeds of long surface waves are much greater than those of long interfacial waves, the delay between the changes in velocity and those in temperature and salinity may result from a lag between the corresponding barotropic and the baroclinic responses to the wind impulse. The distance along the isobath of depth, D = 160 m, between the northeastern and southwestern moorings is 20 km. A barotropic wave of phase speed $\sqrt{gD}$ would require 8 min to traverse this distance. In contrast, the first-mode baroclinic wave speed $= R_i \times f = 0.8$ m s^{-1} (where $R_i = 8$ km is the internal Rossby deformation radius discussed in Chapter 5) implies a time difference of 7 h between the occurrence of the baroclinic response at the southwestern and northeastern moorings. If the baroclinic response is characterized by interfacial Kelvin waves, which travel with shallow water to the right, the response at the southwestern mooring would lag that at the northeastern mooring by this amount.

6.1 The transient upwelling response to a wind-impulse

In order to show how the deformation of the sea surface by the wind stress might cause a current reversal at the shelf break, consider a two-layer representation of the Labrador Current over the continental slope (Figure 6.1). If the Labrador Current were not present, the equilibrium sea surface at $z = 0$ and the equilibrium interface between the two layers at $z = -h$ would both be level. Here, the Labrador Current is directed into the page, parallel to the x axis with an undisturbed velocity of $+u_0$ in the upper layer. The initial, undisturbed sea surface displacement (η) is positive and the displacement (η') of the interface between the two layers is negative. Both decrease in magnitude with distance y away from the shelf. The initial velocity u' in the bottom layer is zero. (Primed variables refer to the lower layer.) The momentum equations in the upper layer are:

$$f\,u_0 = \frac{-1}{\rho}p_y \qquad (6.1)$$

$$g = \frac{-1}{\rho}p_z \qquad (6.2)$$

and in the lower layer,

$$0 = \frac{-1}{\rho'}p'_y \qquad (6.3)$$

$$g = \frac{-1}{\rho'}p'_z \qquad (6.4)$$

where subscripts denote differentiation, g is the acceleration due to gravity, p is the pressure, and ρ is the density. The sea surface elevation is defined by $\eta(y,t)$, and the elevation of the interface above $-h$ is given by $\eta'(y,t)$. Equations 6.2 and 6.4 may be vertically integrated to obtain,
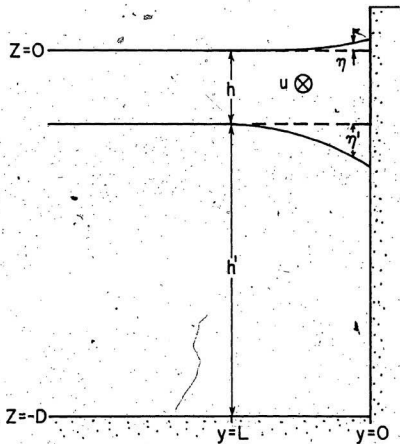
FIGURE 6.1: Schematic and coordinate system for the upwelling analyses

$$p = \rho g (\eta - z) \qquad\qquad -h + \eta' < z < \eta$$

In the upper layer, and

$$p' = \rho g (\eta + h - \eta') + \rho' g (-h + \eta' - z) \qquad z < -h + \eta'$$

or,

$$p' = \rho g (\eta - z) + \Delta\rho g (-h + \eta' - z) \qquad z < -h + \eta'$$

In the lower layer (where $\Delta\rho \equiv \rho' - \rho \ll \rho$). Sea level atmospheric pressure has been set to zero. When differentiated with respect to y, the pressure gradient terms for the upper and lower layer become respectively,

$$\frac{1}{\rho} p_y = g \eta_y \qquad\qquad (6.5)$$

$$\frac{1}{\rho} p'_y = g \eta_y + g' \eta'_y \qquad\qquad (6.6)$$

where

$$g' = \frac{\Delta\rho}{\rho'} g \approx \frac{\Delta\rho}{\rho} g \qquad\qquad (6.7)$$

since $\Delta\rho \ll \rho$ (Boussinesq approximation).

Equations 6.5 and 6.6 are substituted into the horizontal momentum equations 6.1 and 6.3 to obtain,

$$f u_0 = -g \eta_{0_y} \qquad\qquad (6.8)$$

$$0 = g \eta_{0_y} + g' \eta'_{0_y} \qquad\qquad (6.9)$$

The subscript 0 refers to the undisturbed state of the Labrador Current.

Suppose that a short time after the wind impulse occurs, the sea surface is depressed impulsively by a factor $\bar{\eta}$, with $|\bar{\eta}_y| < |\eta_{0_y}|$. The character of the response is expected to be determined by the properties

of the waves generated on the sea surface and the interface. For time scales greater than $1/f$ after the impulse, the time derivatives of velocity may be ignored, and long waves will have traveled distances greater than the Rossby radii of deformation. Because the phase speed of long interfacial gravity waves is very much less than that of long surface gravity waves, it is reasonable to suppose that there is a time lag between the occurrence of maximum deformation of the sea surface and that of the interface in response to the impulse. Because the sea surface slope is expected to decrease in response to an upwelling favorable wind, this time lag implies an imbalanced pressure gradient in the lower layer. Assuming geostrophy, the resultant offshelf momentum balance for the lower layer becomes,

$$g\,\eta_y + g\,\eta_{0_y} + g'\,\eta'_{0_y} = -f_i\,\bar{u}' > 0$$

where $\bar{u}'$ is the current induced in the lower layer by the non-zero pressure gradient. Taking into account the signs in the last relation, $\bar{u}' < 0$. That is, a counter current forms in the lower layer, to the left of the shelf break. Similarly, the addition of $-g\,\eta_{0_y}$ on the right hand side of (6.8) reduces the velocity in the upper layer. Evidence for a reduction in the upper layer flow with a concurrent reversal in the lower layer at Carson Canyon were presented in Chapter 4 (see the discussion of the geostrophic velocity profiles in section 4.5.2). Baroclinic adjustment, and the associated upwelling of deep water, should then take place later, since the baroclinic response time is expected to be determined by the (slower) internal waves. Afterwards, the system will return to the pre-event equilibrium. Petley and O'Brien (1976) discuss theoretical and observational evidence that upwelling relaxation times are at least 2.5 d, consistent with

that observed here (Figure 4.15a).

6.2 Steady upwelling with a shelf break jet

A comprehensive model for the upwelling event of 1981 at Carson Canyon would require that topography, continuous stratification and the shear of the Labrador Current be considered. Killworth (1978), however, concludes that even the upwelling problem posed by a combination of the first two conditions will require a sophisticated numerical model. Wang (1980) has developed a numerical model of the very complex upwelling situation for a simple canyon geometry with stratification. That problem was simplified somewhat by the addition of a coastal boundary at the canyon head. Very localized upwelling may be induced at a canyon because of the increased along-canyon transport associated with those short waves which result from scattering of large scale continental shelf waves (for which the transport is predominantly cross-canyon) by the canyon. A solution for the problem of shelf break upwelling in the presence of a major, horizontally sheared current has not been previously addressed in the literature. Niiler (1969) investigated the upwelling response at the base of a free baroclinic jet (not coastally trapped) due to wind stress parallel to the jet axis. The principal feature was the role of the non-linear interaction of wind-induced velocities via the mean cross-stream shear. A similar formulation is considered below for the coastally trapped case.

An analytic, two-layer model of time-dependent upwelling in the presence of a horizontally sheared current is presented below. The model is based on a coastal upwelling scheme presented by Gill (1982, pp. 403 - 408), which uses the linearized momentum equations to describe the

baroclinic response to a continuous wind stress that is suddenly applied. The problem is made non-linear by the addition of a term involving the cross-stream shear of an upper layer jet. The continental slope is represented by a vertical wall at the shelf break, to the left of which lies the flat bottom (Figure 6.1). h is the thickness of the upper layer and h' is the thickness of the lower layer. Only the region within $\approx$ 30 km of the shelf break wall is considered, so that the contribution of the barotropic mode to the displacement of the interface (considered by Csanady, 1982, pp. 88-91) will be ignored. (The barotropic mode is only important at distances on the order of the Rossby deformation radius (Pedlosky 1979, p. 78) which is $\approx$ 300 km for the shelf break depth of 100 m at the eastern Grand Bank.)

The coordinate system is that defined in Figure 6.1, with u and v the positive southwestward $(+x)$, and off-shelf $(+y)$ velocity components respectively. z is positive vertically upwards. The wind stress at the sea surface, $-\tau^x$, acts in the x direction (i.e. northeastwards) and is spatially uniform. It is assumed that along-slope gradients are negligible compared to cross-slope gradients so that $\frac{\partial}{\partial x}$ terms may be taken as zero in all cases. The effects of the along-slope topography at Carson Canyon on the upwelling will be discussed qualitatively at a later point. Interfacial and bottom stress will be ignored. The set of horizontal momentum equations for the upper layer are.

$$u_t + v u_y - f v = \frac{1}{\rho} \tau^x_z \qquad (6.10)$$

$$v_t + f u = \frac{-1}{\rho} p_y \qquad (6.11)$$

The set of equations for the lower layer are.

$$u'_t - f v' = 0 \qquad (6.12)$$

$$v'_t + fu' = \frac{-1}{\rho'} p'_y \qquad (6.13)$$

The vertical momentum balance is assumed to be hydrostatic (e.g. equations 6.2 and 6.4). Therefore, equations 6.5 and 6.6 will be used for the pressure gradient terms.

The vertically integrated continuity equations are,

$$\frac{\partial}{\partial t}(\eta - \eta') + \frac{\partial}{\partial y}[(h + \eta - \eta')v] = 0 \qquad (6.14)$$

for the upper layer, and

$$\frac{\partial \eta'}{\partial t} + \frac{\partial}{\partial y}[(h' + \eta')v'] = 0 \qquad (6.15)$$

for the lower layer. In these and subsequent equations, the velocity components are vertically averaged over each layer.

After substituting 6.5 and 6.6 in equations 6.11 and 6.13, and making use of the rigid lid approximation, $|\eta'_t| \ll |\eta'_t|$ (which is expected to yield the baroclinic response), the vertically integrated equations become, for the upper layer,

$$u_t + vu_y - fv = \frac{\tau_0^x}{\rho(h - \eta')} \qquad (6.16)$$

$$v_t + fu = -g\eta_y \qquad (6.17)$$

$$\frac{\partial}{\partial y}[(h - \eta')v] = \eta'_t \qquad (6.18)$$

and for the lower layer,

$$u'_t - fv' = 0 \qquad (6.19)$$

$$v'_t + fu' = -g'\eta'_y - g\eta_y \qquad (6.20)$$

$$\frac{\partial}{\partial y}[(h' + \eta')v'] = -\eta'_t \qquad (6.21)$$

where it has been assumed that $|\eta| \ll h$. For brevity, scripts are dropped from τ_0^x with the understanding that τ refers to the wind stress.

Before the upwelling event begins, the undisturbed, horizontally sheared Labrador Current flows in the $+x$ direction with a velocity

$$u_0 = \frac{-g}{f}\eta_{0_y} \qquad (6.22)$$

(with $v_0 = 0$) in the upper layer. The velocity initially is zero in the lower layer (i.e., $u_0' = v_0' = 0$, so that η_0 and η_0' are related by equation 6.20 with the left hand side = 0. The momentum balance before the event is given by equations 6.8 and 6.9. Let

$$u = u_0 + \bar{u}$$
$$u' = \bar{u}'$$
$$v = \bar{v}$$
$$v' = \bar{v}'$$
$$\eta = \eta_0 + \bar{\eta}$$
$$\eta' = \eta'_0 + \bar{\eta}'$$

$\bar{u}, \bar{v}, \bar{v}', \bar{\eta}$, and $\bar{\eta}'$ are perturbations caused by the applied wind stress. These relations are substituted into equations (6.16) – (6.21) and the tildes are dropped. (With the assumption that $\bar{u}_y \ll u_{0_y}$, the only formal change occurs in equation (6.16), where u_y becomes u_{0_y}. The following operations are performed on the indicated equations:

$-f \times (6.16) + \frac{\partial}{\partial t}(6.17)$ for the upper layer,

and $-f \times (6.19) - \frac{\partial}{\partial t}(6.20)$ for the lower. The results are, for the upper and lower layers respectively,

$$v_{tt} - fu_{0_v} + f^2 v + \frac{f\tau}{\rho(h-\eta')} + g\eta_{yt} = 0 \qquad (6.23)$$

$$v'_{tt} + f^2 v' + g' \eta'_{yt} + g \eta_{yt} = 0 \qquad (6.24)$$

Equation (6.21) is used to eliminate the η' term in the last relation and the approximation $|\eta'_0| \gg |\bar{\eta}'|$ is made. This result, combined with equation 6.23, yields.

$$v'_{tt} + f^2 v' - g \frac{\partial}{\partial y} [(h' + \eta') v'] = v_{tt} - f v u_{0_y} + f^2 v + \frac{f \tau}{\rho (h - \eta'_0)} \qquad (6.25)$$

A boundary condition of no flow across the shelf break is determined by the vertical wall at the shelf break (Figure 6.1). This selection might be criticized, but it is not entirely unwarranted. Exchange of water across the shelf break in the real ocean is probably limited to the bottom Ekman layer. Some models (e.g. Johnson and Killworth, 1975, and Lill, 1979) explicitly result in a situation whereby most of the water upwelled along a bottom layer of the continental slope does not cross the shelf break, but instead recirculates back out over the continental slope and above the bottom layer. It has been found theoretically by Johnson and Killworth (1975) that no normal flow across the shelf break occurs in the interior, and that on-shelf flow, is restricted to the bottom Ekman layer. This layer is probably < 5 m thick at Carson Canyon (see section 5.2). On-shelf flow, restricted to a 5-10 m thick bottom layer, is reported by Janowitz and Pietrafesa (1980) for a wind-induced upwelling event at the New England shelf break. According to Huthnance (1981, pp. 202 - 215), upwelling, the effects of eddies or meanders, and mixing all seem to be restricted to within $\approx O(R_i)$ of the shelf break. Finally, the Ekman transport in the bottom boundary layer underlying the Labrador Current is to the left, which is offshelf. The restriction of negligible flow across the shelf break is therefore not purely arbitrary, and it provides a boundary condition at the shelf break in the absence of a canyon. Consequently,

eliminating η'_t from equations 6.18 and 6.21 and integrating with respect to y, the boundary conditions $v(y=0) = v'(y=0) = 0$, requires that.

$$(h - \eta'_0)\dot{v} = -(h' + \eta'_0)v'$$ (6.26)

A single equation for v' results when equation 6.26 is used to substitute for v in (6.25):

$$v'_{tt} + f^2 v' - f\frac{(h' + \eta'_0)}{D} v' u_{0_y} - g'\left[\frac{h - \eta'_0}{D}\right]\frac{\partial^2}{\partial y^2}[(h' + \eta'_0)v'] = \frac{\tau f}{\rho D}$$ (6.27)

where $D = h + h'$.

A steady solution is sought, so v_{tt} is taken equal to zero. This requirement again supposes that a time of at least $O(f^{-1})$ has passed since the beginning of the applied wind stress (Gill, 1982, p. 396). In this analysis, it is assumed that $D = 3000$ m is the depth at the top of the continental rise and that $h = O(100 \text{ m})$. Therefore, $D \approx h' \gg h$ leads to the possibility of assuming that $|\eta'_0| \ll h'$ in (6.27). Making all the above assumptions, equation 6.27 becomes.

$$(f^2 - fu_{0_y})v' - g'(h - \eta'_0)v'_{yy} = \frac{\tau f}{\rho D}$$ (6.28)

By making the substitution $g\eta_{0_y} = -g'\eta'_{0_y}$ and differentiating (6.22) with respect to y, the result,

$$u_{0_y} = \frac{g'}{f}\eta'_{0_{yy}}$$ (6.29)

gives a 2nd order differential equation in η'_0 and v' upon substitution in (6.28).

$$(f^2 - g'\eta'_{0_{yy}})v' - g'(h - \eta'_0)v'_{yy} = \frac{\tau f}{\rho D}$$ (6.30)

A relation for η'_0 in terms of y is now sought. In Chapter 5, the horizontal shear relation.

$$u = U_0 \, e^{-y/a} \qquad (5.12)$$

(where a = internal Rossby deformation radius) was shown to provide an approximate description of the Labrador Current. Similarly, an expression for η'_0 is,

$$\eta'_0 = -\hat{\eta}'_0 \, e^{-y/a} \qquad (6.31)$$

where $\hat{\eta}'_0$ is the initial separation between the interface (below) and the upper layer at $z = -h$ (above) at the shelf break. Substitution of (6.31) into (6.30) results in a 2nd order differential equation for v'.

$$v' \left[f^2 + \frac{g'}{a^2} \, \hat{\eta}'_0 \, e^{-y/a} \right] - g'(h + \hat{\eta}'_0 e^{-y/a}) v'_{yy} = \frac{\tau f}{\rho D} \qquad (6.32)$$

The solution to (6.32) is not known. However, a solution to (6.30) can be obtained if the exponential form of η'_0 (equation 6.31) is approximated by a parabolic shape.

$$\eta'_0 = -\frac{\hat{\eta}'_0}{L^2} (L-y)^2 \qquad (6.33)$$

where L is the distance from the shelf break at which η'_0 becomes equal to zero (Figure 6.1).

Putting (6.33) in (6.30) and dividing the combination by $-g'h$, the following differential equation is obtained,

$$\left[1 + \frac{\hat{\eta}'_0}{hL^2} (L-y)^2 \right] v'_{yy} - \left[\frac{f^2}{g'h} + \frac{2\hat{\eta}'_0}{hL^2} \right] v' = \frac{\tau f}{\rho Dhg'} \qquad (6.34)$$

The 'exterior' solution for $\eta'_0 = 0$ when $y \geqslant L$ is found from the reduction of (6.34),

$$v'_{yy} - \frac{f^2}{g'h} v' = -\frac{\tau f}{\rho Dhg'} \qquad (6.35)$$

One of the boundary conditions is $\lim_{y \gg L} v = a$ constant. Therefore, the exterior ("ex") solution is,

$$v'_{ex} = Ae^{-y/a} + \frac{\tau}{\rho f D} \qquad (6.36)$$

where A is a constant to be determined and $a = \frac{(g'h)^{1/2}}{f} \approx 7$-8 km is the internal Rossby deformation radius for $D \approx h' \gg h$ (see Chapter 5). By matching (6.36) with the "interior" solution of equation 6.34 for $\eta'_0 \neq 0$ when $0 \leq y \leq L$, the constant A may be determined. Before deriving the interior solution, however, a value for L must first be chosen. For $L = 3 \times a \approx 21$-24 km, (6.33) is a good approximation to the exponential form of the interface (Figure 6.2).
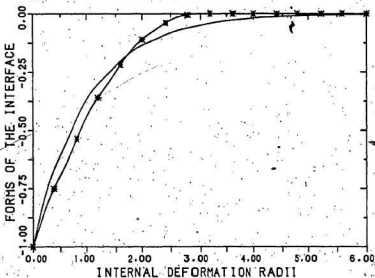
FIGURE 6.2: Comparison of the the exponential (line, see equation 6.31) and the parabolic (star, see equation 6.33) forms of the interface (normalized as η'_0 / η'_0).

The figure for L quoted above is used in Appendix C to compute the interior solution of (6.34) using the method of Frobenius for the special case $\frac{\hat{\eta}'_0}{h} = 0.9$, and to obtain the value of A in equation 6.36. Solutions from Appendix C are reproduced here: for the interior ("in").

$$v'_{in} = \frac{\tau}{\rho f D} \frac{1}{6} \left[0.2335(1+6\xi^2+5\xi^4) \right. \tag{6.37}$$
$$\left. - 2.403(\xi+2\xi^3+0.6\xi^5-0.11429\xi^7+0.047619\xi^9) + 5 \right]$$

$$0 < y < L$$

where,

$$\xi = \sqrt{\frac{\hat{\eta}'_0}{h}} \left(1 - \frac{y}{L}\right) \quad \text{or:} \quad \eta'_0 = -h\xi^2 \tag{6.38}$$

and for the exterior ("ex"),

$$v'_{ex} = \frac{\tau}{\rho f D} \left[1 - 2.55 e^{-y/a}\right], \quad L < y \tag{6.39}$$

In the absence of a sheared jet, (6.36) again results but A is determined solely by the boundary condition. $v' = 0$ at $y = 0$. In that case.

$$v' = \frac{\tau}{\rho f D} \left[1 - e^{-y/a}\right] \quad 0 < y \tag{6.40}$$

which is the usual result (see Csanady, 1982, p. 89). At the eastern Grand Bank (Figure 1.1 shows the bathymetry), where $\tau < 0$, (6.40) indicates that in the absence of a sheared jet, there would be shelfward flow in the lower layer which decays exponentially away from the shelf break. Note that the results for v' in (6.37) – (6.40) are independent of time. Solutions 6.37 – 6.40 have been normalized by $\frac{\tau}{f \rho D}$ and the results graphed in Figure 6.3 (bottom). Comparing the solution for v' when there is no preexisting current, to v'_{in} and v'_{ex} in Figure 6.3 (bottom), it is seen that the flow toward the coast in the lower layer is
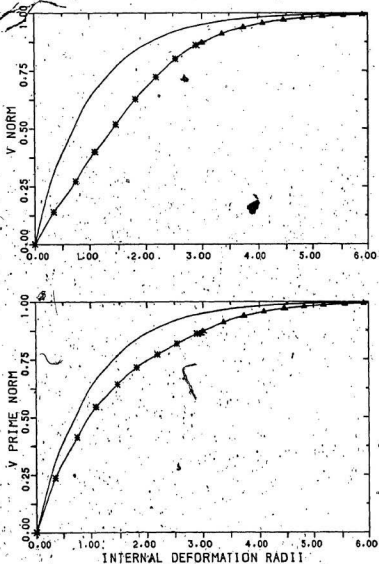
FIGURE 6.3: Top, normalized upper-layer velocities (+v norm is on-shelf). Bottom, normalized lower-layer velocities (+v' norm is off-shelf). Line = 'no jet', star = interior, and triangle = exterior solution in the presence of a jet.

reduced by the presence of a jet, and that the maximum reduction in the magnitude of v' is about 14% at $y = 2 s$. Therefore, on-shelf flow may be suppressed because of the Labrador Current. ✦

The velocity in the upper layer is simply found by using equation 6.26, which is rewritten as,

$$v = \frac{-(h' + \eta'_0)}{(h - \eta'_0)} v' \qquad (6.41)$$

Therefore, when $\eta'_0 \neq 0$, substitution of ξ from (6.38), and taking the limit $\frac{h'}{h} \gg 1 > \xi^2$ ($0 < y < L$), gives the interior solution for the upper layer.

$$v_{in} = \frac{-\tau}{\rho f D} \frac{h'}{h} \frac{1}{(1 + \xi^2)} \frac{1}{6} \qquad (6.42)$$

$$X \quad \left[0.239(1 + 6\xi^2 + 5\xi^4) \right.$$

$$\left. - 2.403(\xi + 2\xi^3 + 0.6\xi^5 - 0.11429\xi^7 + 0.047619\xi^9) + 5 \right]$$

$$0 < y < L$$

or,

$$v_{in} = \frac{-\tau}{\rho f D} \frac{h'}{h} \frac{1}{(1 + \xi^2)} v'_{in} \qquad 0 < y < L \qquad (6.43)$$

In the case where $\eta'_0 = 0$, the exterior solution for v using (6.39) and (6.41) is,

$$v_{ex} = \frac{-\tau}{\rho f D} \frac{h'}{h} \left[1 - 2.55 e^{-y/a} \right] \qquad L < y \qquad (6.44)$$

or,

$$v_{ex} = \frac{-h'}{h} v'_{ex} \qquad (6.45)$$

The solution for v in the absence of a jet is found by combining (6.41) and (6.40) so that,

$$v = \frac{-h'}{h} v' = \frac{-\tau}{\rho f D} \frac{h'}{h} \left[1 - e^{-y/a}\right] \qquad 0 < y < L \qquad (6.46)$$

which again is the usual result. As in the case for the lower layer, the upper layer, cross-slope velocities are independent of time. Note too that the velocities in the upper layer are opposite to those in the lower layer. Values normalized by $\frac{-\tau}{\rho f D} \frac{h'}{h}$ for the upper layer, cross-slope flow according to the interior solution (6.40), the exterior solution (6.42), and the solution in the absence of a jet (6.46) are shown in Figure 6.3 (top). The upper layer velocities are considerably reduced in the presence of the jet, as may be seen by the 42% reduction between $y = a$ and $y = 2\,a$ (about 7 – 14 km from the shelf break).

An expression for η'_t (also called $\tilde{\eta}'_t$ before dropping the tilde in equation 6.23), the perturbation of the interface from η'_0 at equilibrium for $0 < y < L$, is derived by solving equation 6.21. (or equivalently, 6.18). Here, equation 6.21 is expanded and the approximation $|\eta'_0| \gg |\eta'|$ (made earlier in equation 6.25) is assumed, so that.

$$-\eta'_t = \eta'_0 v' + (h' + \eta'_0) v'_y \qquad (6.47)$$

Equation 6.47 for the interior with η'_0 given by (6.33) is.

$$-\eta'_{in_t} = 2 \frac{\hat{\eta}'_0}{L} \left[1 - \frac{y}{L}\right] v'_{in} + \left[h' - \hat{\eta}'_0 \left[1 - \frac{y}{L}\right]^2\right] v'_{in_y} \qquad (6.48)$$

$$0 < y < L$$

Substitution of ξ (6.38) in the last equation and noting that

$$\frac{d}{dy} = \frac{-1}{L} \sqrt{\frac{\hat{\eta}'_0}{h'}} \frac{d}{d\xi} \text{ yields.}$$

The approximation $\frac{h'}{h} \gg 1 > \xi^2$ ($0 \leq y \leq L$) is made (also used earlier in connection with equation 6.41) which removes the ξ^2 term from equation 6.49, $\frac{\eta'_0}{\eta h}$ is replaced by 0.9 (see Appendix C). L by $3a$, and (6.49) rearranged so that,

$$\eta'_{\ln_t} = \frac{-\sqrt{0.9}}{3\ a} \frac{h'}{h} \left[2\xi \frac{h}{h'} v'_{\ln} - v'_{\ln_\xi} \right] \qquad (6.50)$$

Integration of (6.50) with respect to t with the boundary condition that $\eta'(t=0) = 0$, and substitution for $v'_{\ln}$ from (6.39) yield the interior solution for the perturbation of the interface,

$$\eta'_{\ln} = \frac{-\tau t}{\rho f a} \frac{h'}{D} \qquad (6.51)$$

$$\times \frac{\sqrt{0.9}}{18} \left\{ 2 \frac{h}{h'} \left[0.2335 (\xi + 6\xi^2 + 5\xi^5) \right. \right.$$

$$\left. - 2.424 (\xi^2 + 2\xi^4 + 0.6\xi^6 - 0.11429\xi^8 + 0.047619\xi^{10}) + 5 \right]$$

$$- \left[0.2335 (12\xi + 20\xi^3) \right.$$

$$\left. \left. - 2.424 (1 + 6\xi^2 + 3\xi^4 - 0.8\xi^6 + 0.42857\xi^8) \right] \right\}$$

$$0 \leq y \leq L$$

The exterior solution to the time integral of (6.47) with $\eta'_0 = 0$ and v'_{ex} given by (6.39), is,

$$\eta'_{ex} = \frac{-\tau t}{\rho f a} \frac{h'}{D} 2.55 e^{-y/a} \qquad L \leq y \qquad (6.52)$$

In the case where there is no pre-existing sheared jet, the solution to (6.47) using (6.40) for v' is simply,

$$\eta' = \frac{-\tau t}{\rho f a} \frac{h'}{D} e^{-y/a} \qquad 0 \leq y \qquad (6.53)$$

consistent with earlier work.

Note that η' is linearly dependent on time. η'_{in}, η'_{ex} and η' after having been normalized by $\frac{-\tau t}{\rho f s} \frac{h'}{D}$ are shown in Figure 6.4.

INTERNAL DEFORMATION RADII
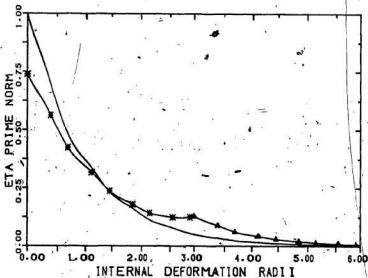
FIGURE 6.4:   Normalized η'. Positive η prime norm refers to upward deflections. Line = 'no jet', star = interior, and triangle = exterior solution in the presence of a jet.

It may be seen in Figure 6.4 that the elevation of the interface at the shelf break ($y = 0$) is reduced by 26% in the case where a jet is present. Interestingly, upwelling is enhanced at distances $\geqslant 1.5\,s$, or, $\geqslant 10$ km away from the shelf break. A peak is evident at $y = 3\,s$. Careful inspection of Figure 6.3 (bottom) shows that there is an inflection point at $y = 3\,s$. The flattening of the curve implies that the second derivative of this lower layer velocity is not continuous there. This inflection might be due to the assumption made in equation 6.28 that $h' \gg \eta'_0$ before taking the 2nd derivative with respect to y. The discontinuity does

not result from truncation of the polynomial equation. C.16b of Appendix C, used to solve for v'_{in}. Calculation of the derivative of C.16b (see Table C.2b) shows that the resultant series is convergent, and that the maximum error is only 2% because of truncation. At $y = 3a$, upwelling is greater by 30% when a jet is present.

6.3 Discussion

Figure 6.3 shows that velocities are reduced in both layers when a shelf break jet is present. Nevertheless, transports must remain the same in the upper and lower layers individually, because the cross-slope motion of water is ultimately driven by the Ekman transport in the open ocean. The decreased velocities are the result of an increase in the length scale, which is called the "effective internal deformation radius". To see how the increased length scale arises, consider equation 6.28 and what the absence of a sheared jet implies. With u_{0_y} and η'_0 equal to zero, then, equation 6.28 is given by (6.35) and the solution is as given by (6.40). The typical length scale is the internal deformation radius, $a = \dfrac{\sqrt{g'h}}{f} = 7$ km, which may be seen to arise from equation 6.35, and therefore, from equation 6.28. In an analogous fashion,

$$a' = \frac{\sqrt{g'\,(h-\eta'_0)}}{\sqrt{f^2 - tu_{0_y}}} \qquad (6.54)$$

is the effective internal deformation radius for the sheared jet case according to equation 6.28. By scaling η'_0 by $-\hat{\eta}'_0$ (found to be 90 m in Appendix C) and combining (6.29) and (6.31). for u_{0_y}, (6.54) becomes,

$$a' = \frac{\sqrt{g'h}}{f} \frac{\sqrt{1 + \frac{\hat{\eta}'_0}{h}}}{\sqrt{1 + \frac{2}{9}\frac{\hat{\eta}'_0}{h}}} \qquad (6.55)$$

Since $a = \frac{\sqrt{g'h}}{f}$, and with $a_* = \frac{\hat{\eta}'_0}{h} = 0.9$ (as determined in Appendix C), the new length scale is therefore,

$$a' = a \frac{\sqrt{1 + a_*}}{\sqrt{1 + \frac{2}{9}a_*}} = 1.26a \qquad (6.56)$$

Consequently, a' is 26% more than a, or, ≈ 8.8 km. Note that since the effect of shear (u_{0_y}) is a reduction of a, but that the effect of the initial deflection of the interface (η'_0) is an increase of a, the presence of a current (a linear slope for η'_0) is probably more important than shear in reducing the upwelling at the shelf break. At least this is so for the parameters chosen to represent the Labrador Current.

This model does not consider the shear on the right hand side of the Labrador Current looking downstream. The effects of bottom slope would have to be considered in that case and the path to a solution is not clear. Nevertheless, from previous discussion it seems that the downward sloping isopycnals associated with the Labrador Current are more important to the suppression of upwelling than is the shear. Also, this model does not take into account the change in sign of the shear at the axis of the Labrador Current. Niiler (1969) has examined the effects on upwelling of wind stress over a sheared jet through the non-linear term. His results suggest that downwelling could be produced along the axis of the Labrador Current by an upstream-directed wind stress.

8.4   Localized wind-driven upwelling at Carson Canyon?

In Chapter 4, a comparison of CTD data from 1980 and 1981 indicated that the vertical structure along Carson Canyon's central axis is strongly perturbed by the upwelling event close to the shelf break. The amplitude of the temperature and salinity changes at the central axis upper meter are lower than at the shelf break meters. These observations are consistent with the result that the magnitude of the disturbance (e.g. the upward motion of the interface given by equations 6.50 - 6.52) should decrease almost exponentially away from the shelf break. The question is whether this effect is more or less pronounced at the canyon.

Shaffer (1976) discusses data which were collected in a canyon of dimensions similar to Carson Canyon, but off the northwestern coast of Africa. Density sections drawn from CTD transects parallel to the canyon axis indicated that upwelling of intermediate layer ($\sim$ 300 m) water due to an along-shelf wind stress was most intense in a O(3 km) wide zone at the head. Mean vertical velocities of 10^{-2} to 10^{-1} cm s^{-1} were directly measured in the fixed upwelling center which formed at the head of the canyon using free floating, neutrally buoyant vertical current meters. Very much smaller velocities were found outside the zone.

No data are available in the far field during the Carson Canyon upwelling event of June, 1981, and therefore the extent to which this event might have been amplified at the canyon is not known. However, similar wind-induced upwelling events, but in the absence of a strong jet, have been observed at the shelf break off Nova Scotia (Petrie, 1983). Upwelling events associated with off-shelf Ekman surface transports were caused by along-slope winds of speed ≥ 10 m s^{-1} blowing for 2 or more days. At least 20 events occurred during the period October 1976 to March 1977

and October to December 1977. Vertical velocities of $0.05 - 0.2$ cm s^{-1} are estimated from the ascent of isotherms from intermediate depths. On-shelf bottom currents of about 1 m s^{-1} peak speed are reported. It is suggested that variations in the along-slope topography could amplify the cross-shelf currents.

CHAPTER 7   SUMMARY AND CONCLUSIONS

7.1   Summary

There are essentially three parts to this thesis: 1) analysis of the observations pertaining to the mean flow of the Labrador Current at Carson Canyon. 2) analysis of the observations of a time-dependent wind-induced upwelling event in the canyon in 1981. 3) a model of wind-induced steady coastal upwelling in the presence of a coastally trapped jet.

The mean flow characteristics at Carson Canyon were synthesized from data collected in 1980 and in 1981. The dynamic topography of the 5 dbar surface relative to 200 dbar. cross-slope CTD sections of temperature and salinity. and moored current meter measurements from both years were combined to produce a mean flow pattern. The principal charac-teristics of the pattern are: predominantly along-isobath flow in the far field up- and downstream of the canyon. cross-isobath and cross-canyon flow at the northeastern wall and central axis. along-isobath flow at the head and at the southwestern wall. wave-like features in the canyon lee. splitting of the cold (< -1 °C) temperature core downstream of the secondary head. and a deep return flow toward the secondary head at the central axis. The influence of stratification and topography on the mean flow was examined using a 2-layer conceptual model and arguments based on the conservation of potential vorticity. The mean flow models presented by Mayer et al. (1982) and Freeland and Denman (1982) are applied to Carson Canyon.

A wind-driven upwelling event of about 5 d duration occurred as a result of a storm with peak wind-speeds of 23 m s^{-1} directed parallel to

the shelf break in the vicinity of the canyon. The onset of the event was defined as a simultaneous reversal of the measured current on the southwestern side of the canyon and a near-reversal on the northeastern side near the shelf break at 145 m depth, 10 m above bottom on 8 June. Abrupt temperature (2.8 °C) and salinity (1.2 ppt) increases associated with brief periods of on-shelf flow occurred at these locations about 1 d after the start of variations in the velocity field as the result of upwelling of water from intermediate depths (≈ 300 m). Both the magnitude and rate of change of temperature and salinity decreased away from the shelf break toward the center of the canyon. Based on CTD data and moored current meter measurements from the central canyon region, peak and mean rates of ascent of isohalines of 0.5 cm s^{-1} and 0.2 cm s^{-1} were found for the initial phase of the event. The geostrophic current at 5 dbar relative to 200 dbar exhibited reduced speeds, but remained southwestward over the central axis during the upwelling event. At the same time, however, a 10 cm s^{-1} current in the opposite direction was measured at 167 m depth. This counter current was also present in a vertical profile of geostrophic velocity at the mooring location as a 4.4 cm s^{-1} flow centered at 130 m.

Because the phase speed of a long surface wave is much greater than that of a long interfacial wave, and the current reversal of June 8 preceded upwelling by about 1 d, the current reversal was explained as the transient, barotropic response to a sudden sea-surface depression caused by meteorological forcing. The possible effect of the Labrador Current on shelf break upwelling was studied by extending the usual linear, two-layer coastal model scheme (e.g. Gill 1982, pp. 403 – 408) by adding a coastally trapped upper-layer jet. This introduces a non-linear
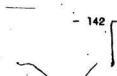
term which arises from the cross-stream advection of streamwise momentum by wind-induced motion. Cross-slope velocities in each layer were reduced compared to the case when no jet is present. A final expression for the interfacial deformation indicated a 26% reduction of upwelling at the coast and an enhancement of upwelling at greater distances off-shore due to the presence of the jet. The suppression of upwelling was traced to a 26% increase in the value of the internal Rossby deformation radius.

7.2 Conclusions

Investigation of the circulation in submarine canyons is a recent development in physical oceanography. This is the first study of any of the eastern Grand Bank canyons. The dynamics at Carson Canyon are different from those of other canyons discussed in the literature because of the presence of the Labrador Current. This current is a narrow 50 cm s^{-1} jet trapped at the shelf break and continental slope which flows across the canyon with shallow water on the right, and so isopycnals slope downward toward the shelf. Transport in the bottom Ekman layer is expected to be off-shelf.

The mean flow interaction with the canyon changes with off-shelf distance due to changes in stratification, and due to an abrupt reduction of the radii of curvature of the isobaths seaward of the secondary head on the upstream side of the canyon. Horizontal divergence and steady upwelling at the secondary head are hypothesized, and may account for the observed upcanyon residual near-bottom flow. An alternate explanation based on the Mayer et al. (1982) and Freeland and Denman (1982) models is given, and illustrates the importance of the direction of the cross flow above the canyon relative to the direction of increasing axial

depth.

A wind-induced upwelling event within Carson Canyon was amplified at the shelf break and on the downstream side. It is not known to what extent the effects were localized to the canyon. However, model results indicate that the Labrador Current inhibits wind-induced upwelling at the shelf break outside canyon regions.

The results indicate that topographically controlled upwelling may occur at the secondary head, wind-driven, upwelling occurs near the shelf break at the canyon, and that this latter type of upwelling may be suppressed by the Labrador Current outside canyon regions. These processes affect the local circulation and cross-slope material fluxes, which are expected to be important to problems related to biological production and environmental problems related to the oil industry.

Future studies at Carson Canyon should be based on better navigation than has been available, and should include measurements of local winds. CTD surveys should be more closely spaced to resolve the cross-stream velocity structure and should be uninterrupted and repeated to reduce tidal aliasing, and more and longer term current measurements both in the vertical and in the near and far field are required.

- 143 -

References

Armi, L. and R. C. Millard. Jr. (1976) The bottom boundary layer of the deep ocean. Journal of Geophysical Research, 81, 4983–4990.

Baines, P. G. (1983) Tidal motion in submarine canyons–a laboratory experiment. Journal of Physical Oceanography, 13, 310–328.

Batchelor, G. K. (1967) An introduction to fluid dynamics. Cambridge University Press, 615 pp.

Bennett, (1976) Conversion of in situ measurements of conductivity to salinity. Deep-Sea Research, 23A, 157–165.

Blanton, J. O., L. P. Atkinson, L. J. Pietrafesa and T. N. Lee (1981) The intrusion of Gulf Stream water across the continental shelf due to topographically-induced upwelling. Deep-Sea Research, 28A, 393–405.

Cannon, G. A. (1972) Wind effects on currents observed in Juan De Fuca Submarine Canyon. Journal of Phyical Oceanography, 2, 281–285.

Coachman, L. K. and C. A. Barnes (1962) Surace water in the Eurasian Basin of the Arctic Ocean. Arctic, 15, 251–277.

Csanady, G. T. (1982) Circulation in the coastal ocean. D. Reidel Publishing Co., 279 pp.

DeYoung, B. (1983) Deep-water exchange in Fortune Bay Newfoundland. M. Sc. Thesis. Memorial University, St. John's, Newfoundland, 146 pp.

Forrester, W. D. and J. R. Benoit (1981) Physical oceanography of waters over the Grand Banks of Newfoundland. Prepared for Mobil Oil Canada Ltd., confidential (unpublished) manuscript, 61 pp.

Freeland, H. J. and K. L. Denman (1982) A topographically controlled upwelling center off southern Vancouver island. Journal of Marine Research, 40, 1069–1093.

Gill, A. E. (1982) Atmosphere–ocean dynamics. In: International Geophysics Series, Vol. 30, William L. Donn, editor, Academic Press, 662 pp.

Godin, G. (1972) The analysis of tides. University of Toronto Press, 264 pp.

Gordon, R. L. (1982) Internal modes in a submarine canyon. Journal of Geophysical Research, 87C, 582–584.

Hayes, R. M. (1984) On the flow through Flemish Pass. Unpublished manuscript, 27 pp.

Hayes, S. P. and D. Halpern (1976) Variability of the semidiurnal internal tide during coastal upwelling. Memoires Societe Royal des Sciences de Liege, 6° serie, tome X, 175-186.

Hildebrand, F. B. (1962) Advanced Calculus for Applications. Prentice-Hall of Canada, Ltd., 646 pp.

Hill, H. W., P. G. W. Jones, J. W. Ramster and A. R. Folkard (1973) A note on the Labrador and Atlantic Currents to the east of Newfoundland Grand Bank. ICNAF resource Document 73/116 (Serial No. 3082), 34 pp.

Hogg, N. G. (1980) Effects of bottom topography on ocean currents. GARP Publication Series, 23, 167-205.

Hotchkiss, F. S. and C. Wunsch (1982) Internal waves in Hudson Canyon with possible geological implications. Deep-Sea Research. 29A, 415-442.

Hsueh, Y. (1980) On the theory of deep flow in the Hudson Shelf Valley. Journal of Geophysical Research, 85C, 4913-4918.

Huthnance, J. M. (1981) Waves and currents near the continental shelf edge. Progress in Oceanography, 10, 193-226.

Inman, D. L., C. E. Nordstrom and R. E. Flick (1976) Currents in submarine canyons: An air-sea-land interaction. Annual Review of Fluid Mechanics, 8, 275-310.

Janowitz, G. S. and L. J. Pietrafesa (1980) A model and observations of time-dependent upwelling over the mid-shelf and slope. Journal of Physical Oceanography, 10, 1574-1583.

Johnson, J. A. and Killworth P.D. (1975) A bottom current along the shelf break. Journal of Physical Oceanography, 5, 185-188.

Kanasewich, E. R. (1975) Time sequence analysis in geophysics. The University of Alberta Press, 364 pp.

Keenan, P. V. (1979) Sources of compass error within the Aanderaa recording current meter: revised 1979. Bedford Institute of Oceanography Report Series B1-R-79-6, 70 pp.

Keenan, P. V. (1981) Aanderaa recording current meter compass error caused by mooring system components. Bedford Institute of Oceanography Report Series B1-R-81-6, 27 pp.

Killworth, P. D. (1978) Coastal upwelling and Kelvin waves with small longshore topography. Journal of Physical Oceanography, 8, 188-205.

Knauss, J. A. (1978) Introduction to physical oceanography. Prentice Hall of Canada Ltd., 328 pp.

Kudlo, B.P., V.P. Boystov (1978) Dynamics and salinity of waters in the Newfoundland area in 1976-77. Internal Communication of the Northwest Atlantic Fisheries. Redbook 1972. Part III.

Kudlo, B.P., V. V. Burmakin, and U. S. Sterkhov (1979) Geostrophic circulation of the Northwest Atlantic waters according to long-term dates. Internal Communication of the Northwest Atlantic Fisheries Resources Document No. 5469.

Lill, C. C. (1979) Upwelling over the shelf break. Journal of Physical Oceanography, 9, 1044-1047.

Mayer, D. A., H. O. Mofjeld and K. D. Leeman (1981) Near-inertial internal waves observed on the outer shelf in the Middle Atlantic Bight in the wake of hurricane Belle. Journal of Physical Oceanography, 11, 87-106.

Mayer, D. A., G. C. Han and D. V. Hansen (1982) Circulation in the Hudson Shelf Valley: MESA physical oceanographic studies in New York Bight, 1. Journal of Geophysical Research, 87C, 9563-9578.

Mountain, D. G., L. K. Coachman and Knut Aagaard (1976) On the flow through Barrow Canyon. Journal of Geophysical Research, 85C, 4097-4100.

Mountain, D. G. (1980) Direct measurements in the Labrador Current. Journal of Geophysical Research, 85C, 4097-4100.

Neumann, G. and W. J. Pierson, Jr. (1966) Principles of physical oceanography. Prentice-Hall, 545 pp.

Niller, P. P. (1969) On the Ekman divergence in an oceanic jet. Journal of Geophysical Research, 74, 7048-7052.

Pedlosky, J. (1979) Geophysical fluid dynamics. Springer-Verlag, 624 pp.

Peffley, M. B. and J. J. O'Brien (1976) A three-dimensional simulation of coastal upwelling off Oregon. Journal of Physical Oceanography, 6, 164-180.

Petrie, B. (1982) Aspects of the circulation on the Newfoundland Continental Shelf. Canadian Technical Report of Hydrography and Ocean Sciences, No. 11, 78 pp.

Petrie, B. and C. Anderson (1983) Circulation on the Newfoundland Continental Shelf. Atmosphere-Ocean. 21, 207-226.

Reid, J. L. and A. W. Mantyla (1976) The effect of the geostrophic flow upon coastal sea elevations in the Northern North Pacific Ocean. Journal of Geophysical Research. 81, 3100-3110.

Robe, R. Q. (1975) Circulation East of the Grand Banks, 1973. ICNAF resource Document 73/116 (Serial No. 3082). 7 pp.

Seaconsult, Marine Research Ltd. (1978) Analysis of ocean currents. Flemish Pass. 1603 - 740 West Pender St., Vancouver, Canada, V6C 2B8. 164 pp.

Scoble, Lt. R. W. (1975) International Ice Patrol Operations 1972 - Why so many icebergs. ICNAF resource Document 7/118 (Serial No. 3082). 34 pp.

Shaffer, G. (1976) A Mesoscale Study of Coastal Upwelling Variability off NW-Africa. Meteor Forschungsergebnisse A. 17, 21-72.

Stommel, H. (1965) The Gulf Stream. University of California Press. 248 pp.

Smith, R. B. (1979) The influence of mountains on the atmosphere. Advances in Geophysics. 21, 87-230.

Smith, E. H., F. M. Soule and O. Mosby (1937) The Marion and General Greene expeditions to Davis Strait and Labrador Sea. Bulletin of the U.S. Coast Guard. No. 19. 259 pp.

Stansell, T. A. (1978) The transit navigation satellite system. Magnavox Co., 83 pp.

Walters, R. A. and C. Heston (1982) Removing tidal-period variations from time-series data using low-pass digital filters. Journal of Physical Oceanography. 12, 112-115.

Wang, D.-P. (1980) Diffraction of continental shelf waves by irregular alongshore geometry. Journal of Physical Oceanography. 10, 1187-1199.

Appendix A

TABLE A1: Statistics for the 1980 current meters

COMPONENT	SOUTHWESTERN				NORTHEASTERN			
	MIN	MAX	MEAN	σ	MIN	MAX	MEAN	σ
I (cm/s)								
Despiked	-15.8	26.1	3.7	8.3	-20.1	32.6	3.9	7.9
FLP	-13.9	22.1	3.8	8.1	-18.3	25.6	3.9	7.6
SLP	2.0	6.4	4.2	1.2	0.7	9.2	4.4	2.1
BP	-13.5	17.8	0.2	7.7	-18.8	16.1	-0.1	6.8
J (cm/s)								
Despiked	-0.1	36.3	18.2	7.7	-1.7	40.9	19.0	8.3
FLP	3.9	34.8	18.3	7.6	1.1	38.5	18.9	8.1
SLP	9.8	24.1	16.8	4.5	12.5	26.0	19.0	4.4
BP	-9.7	12.8	-0.1	4.7	-11.6	13.3	0.1	6.2
T (°C)								
Despiked	-0.96	-0.02	-0.59	0.21				
FLP	-0.96	-0.06	-0.59	0.21				
SLP	-0.71	-0.38	-0.54	0.10				
BP	-0.28	+0.43	0.00	0.15				

TABLE A2: CTD Cast Information for June, 1980

| Station Number	Time/Date GMT/June	Latitude deg. min. N	Longitude deg. min. W	Depth of Cast (m)
1	0528/4	45 40.00	48 40.40	85
2	0654/4	45 36.22	48 35.10	86
3	2110/1	45 33.00	48 33.50	129
4	2252/1	45 29.12	49 26.16	490
5	0045/2	45 25.02	48 21.45	531
6	0218/2	45 21.38	49 16.69	503
7	1640/2	45 21.25	48 16.73	499
8	1513/2	45 24.96	48 25.43	504
9	2319/4	45 30.61	48 38.19	388
10	1655/1	45 26.97	48 32.27	370
11	23 hourly casts	45 29.	48 38.	500
12	0006/3	45 27.66	48 38.75	499
13	0552/6	45 27.56	48 37.82	500
14	1705/4	45 23.49	48 33.79	502
15	0829/2	45 23.26	48 33.94	504
16	2237/2	45 22.88	48 33.71	499
17A	2110/2	45 19.10	48 29.12	501
17B	1635/3	45 19.92	48 29.33	502
18	0358/2	45 16.18	48 24.25	498
19	1810/2	45 16.12	48 24.73	501
20	0400/4	45 35.00	48 48.00	85
21	0059/5	45 32.56	48 46.50	127
22	1249/1	45 31.50	48 44.89	179
23A	0250/3	45 31.26	48 43.45	252
23B	0013/5	45 31.18	48 43.31	243
24	2235/4	45 27.52	48 38.96	405
25	1835/4	45 25.34	48 37.77	402
26	1805/5	45 22.05	48 36.56	500
27	0600/3	45 15.76	48 29.61	500
28	0204/5	45 28.06	48 44.96	128
29	0143/6	45 24.86	48 43.22	152
30	0240/5	45 23.72	48 42.44	280
31	1935/5	45 23.79	48 40.37	412
32	0034/6	45 23.30	48 41.01	389
33	1547/4	45 19.87	48 37.94	502
34	0148/4	45 30.05	48 55.98	66
35	0010/4	45 26.00	48 51.50	79
36	2335/5	45 22.44	48 47.51	104
37	2306/3	45 22.50	48 46.70	131
38	2112/3	45 18.53	48 42.20	399
39	1927/3	45 15.07	48 37.21	499
40	1751/3	45 11.20	48 32.68	499
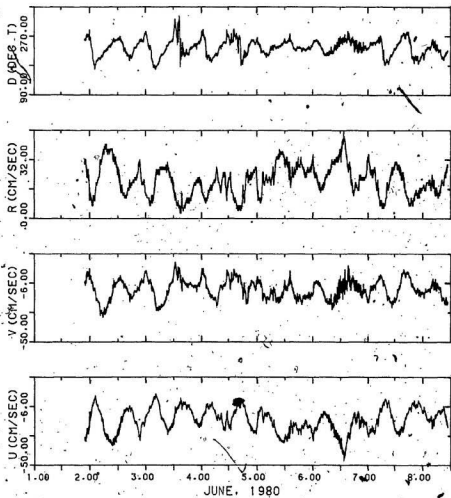
FIGURE A1: Despiked time-series of direction, rate and the U and V components of velocity for the 1980 northeastern meter (mooring 80-2)
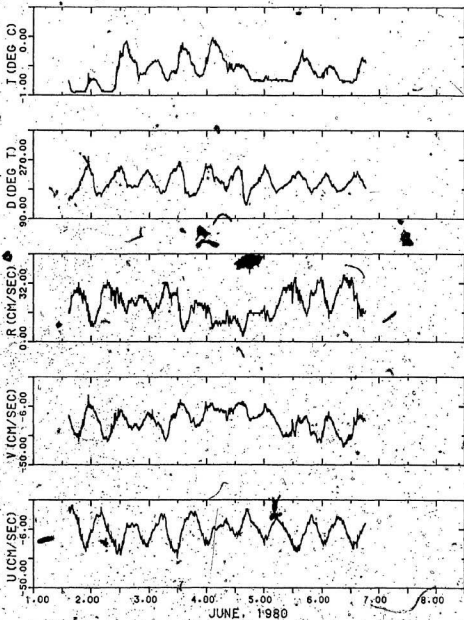
FIGURE A2: Despiked time-series of temperature, direction, rate and the U and V components of velocity for the 1980 southwestern meter (mooring 80-1)
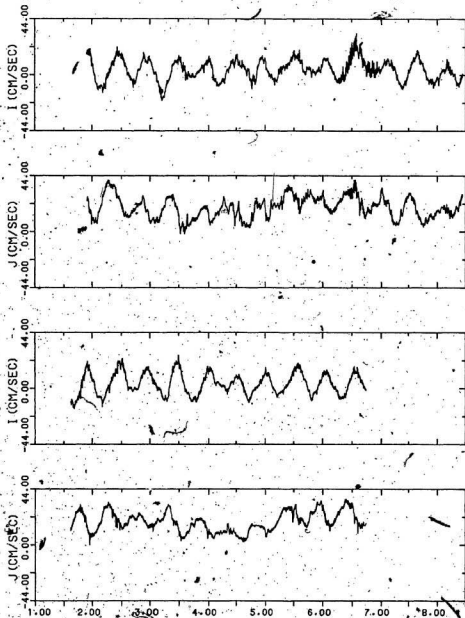
FIGURE A3: Despiked I and J velocity components for the 1980 northeastern (mooring 80-2), top, and southwestern meter (mooring 80-1), bottom.
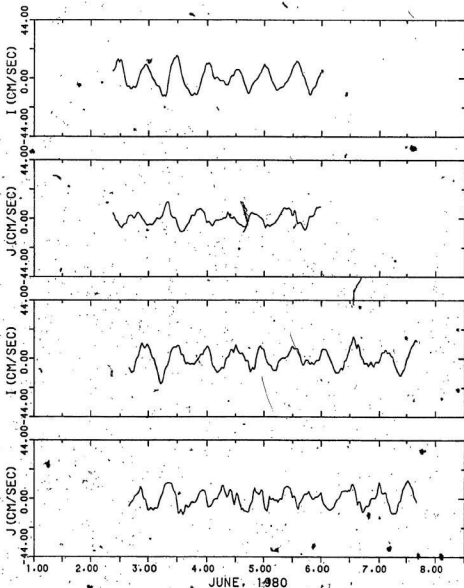
FIGURE A4: BP time-series of the I and J components of velocity for the 1980 southwestern meter (mooring 80-1) -(top) and the 1980 northeastern meter (mooring 80-2) -(bottom)
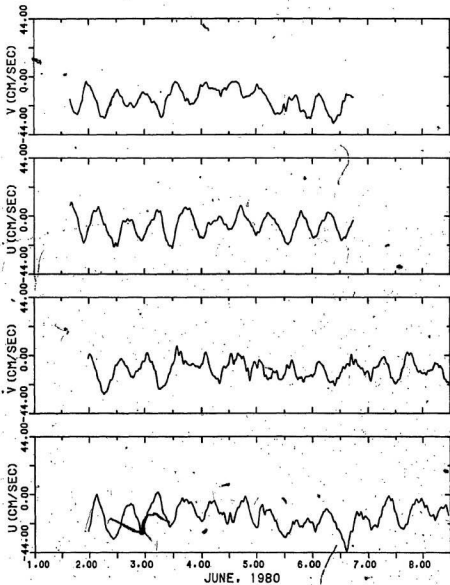
FIGURE A5: FLP time-series of the U (+ eastward) and V (+ northward)
            components of velocity for the 1980 southwestern meter
            (mooring 80-1) -(top) and the 1980 northeastern meter
   (mooring 80-2) -(bottom)
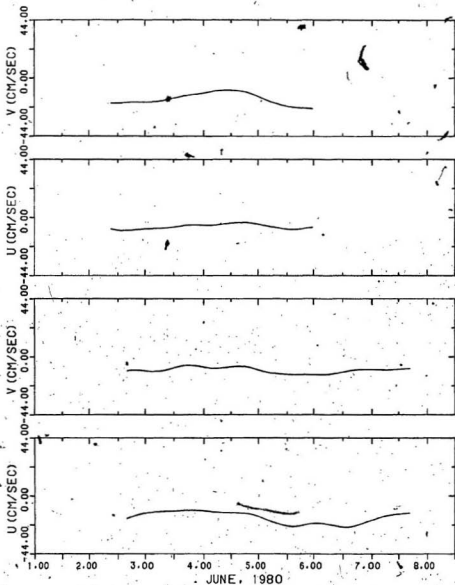
FIGURE A8: SLP time-series of the U (+ eastward) and V (+ northward)
components of velocity, for the 1980 southwestern meter
(mooring 80-1) – (top) and the 1980 northeastern meter
(mooring 80-2) – (bottom).
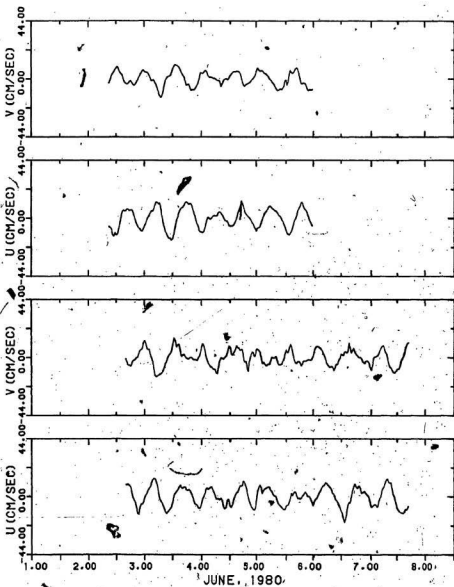
FIGURE A7: BP time-series of the U (+ eastward) and V (+ northward)
components of velocity for the 1980 southwestern meter
(mooring 80-1) -(top) and the 1980 northeastern meter
(mooring 80-2) -(bottom)
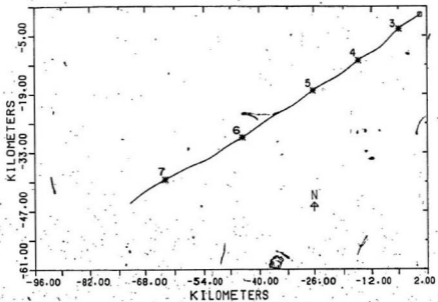
FIGURE A8: FLP PVD's for
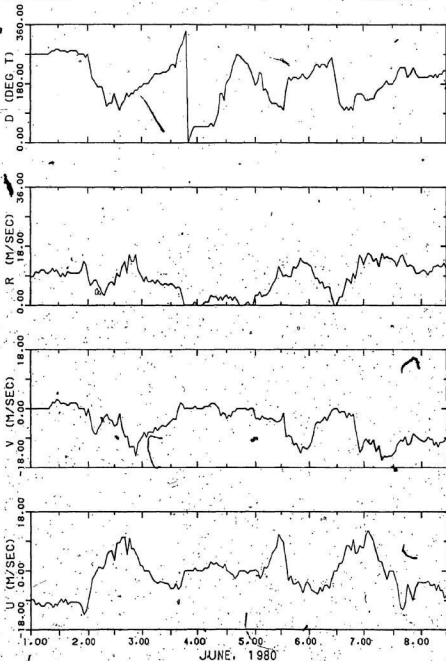the 1980 northeastern (top)
and southwestern (bottom)
current meters
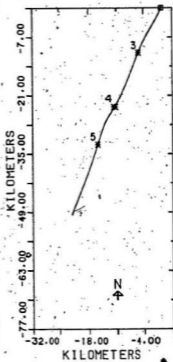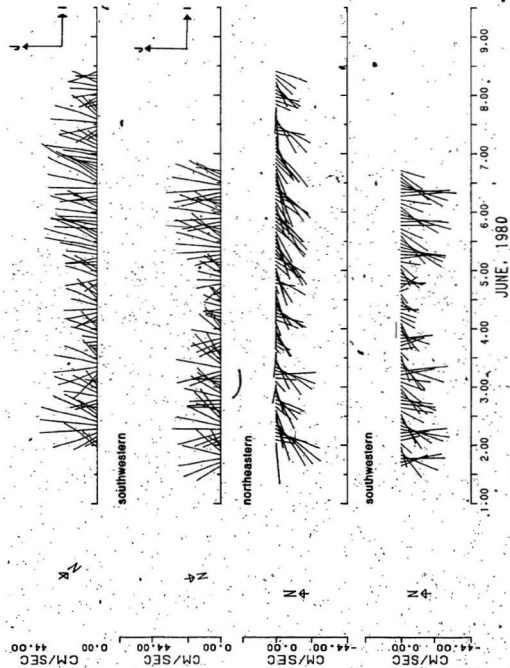
FIGURE A9: 1980 FLP stick plots: sampled every 90 min. Upper panel pair, I and J; lower pair, U and V.

JUNE, 1980

WINDS, ZAPATA UGLAND, 1980, MET. CONVENTION

FIGURE A10: Direction, rate, V (+ northerly) and -U (+ easterly) components of the wind data from Hibernia for 1980.
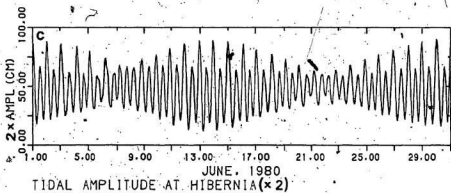
JUNE, 1980
TIDAL AMPLITUDE AT HIBERNIA(× 2)

FIGURE A11:   Tidal heights from Hibernia for June, 1980.

Appendix B

TABLE B1a: Statistics for the 1981 southwestern meter

COMPONENT	MINIMUM	MAXIMUM	MEAN	σ
I (cm/s)				
Despiked	-28.2	18.2	0.3	5.9
FLP	-25.4	14.8	0.3	5.7
SLP	-7.4	6.0	0.2	3.4
BP	-18.9	10.8	0.0	3.9
J (cm/s)				
Despiked	-20.5	41.5	6.3	10.6
FLP	-19.2	39.8	6.4	10.5
SLP	-9.4	25.8	6.7	8.6
BP	-11.7	15.7	0.1	5.6
T (°C)				
Despiked	-0.85	1.93	0.00	0.95
FLP	-0.83	1.93	0.00	0.95
SLP	-0.79	1.79	0.10	0.94
BP	-0.76	-0.40	0.00	0.14
S (ppt)				
Despiked	33.02	34.26	33.45	0.40
FLP	33.03	34.21	33.45	0.39
SLP	33.07	34.16	33.49	0.39
BP	-0.30	0.19	0.01	0.06

TABLE B1b: Statistics for the 1981 central axis upper meter

COMPONENT	MINIMUM	MAXIMUM	MEAN	σ
I (cm/s)				
Despiked	-23.7	27.7	1.1	9.8
FLP	-22.8	26.9	1.1	9.7
SLP	-12.7	12.0	1.1	5.5
BP	-16.5	17.4	0.0	7.3
J (cm/s)				
Despiked	-23.2	26.1	4.2	11.2
FLP	-21.1	26.7	4.2	11.1
SLP	-15.6	19.1	3.8	9.9
BP	-14.3	17.1	0.0	5.0
T (°C)				
Despiked	-0.44	1.81	0.38	0.58
FLP	-0.42	1.77	0.38	0.58
SLP	-0.26	1.43	0.43	0.55
BP	-0.58	0.53	0.00	0.18
S (ppt)				
Despiked	33.16	34.34	33.70	0.26
FLP	33.35	34.29	33.71	0.25
SLP	33.43	34.16	33.73	0.24
BP	-0.24	0.22	0.00	0.08

TABLE B1c: Statistics for the 1981 central axis lower meter

COMPONENT	MINIMUM	MAXIMUM	MEAN	σ
I (cm/s)				
Despiked	-17.2	20.1	-0.4	5.4
FLP	-16.5	16.2	-0.4	5.2
SLP	-3.3	3.0	-0.3	1.8
BP	-16.2	13.6	0.0	4.6
J (cm/s)				
Despiked	-9.8	9.3	-0.4	2.5
FLP	-8.2	7.0	-0.3	2.2
SLP	-1.8	1.1	-0.3	0.8
BP	-4.5	6.2	0.0	1.9
T (°C)				
Despiked	3.28	3.66	3.57	0.09
FLP	3.30	3.66	3.58	0.09
SLP	3.45	3.66	3.58	0.07
BP	-0.14	0.09	0.00	0.02
S (ppt)				
Despiked	34.79	34.99	34.90	0.03
FLP	34.82	34.96	34.90	0.02
SLP	34.87	34.92	34.89	0.02
BP	-0.05	0.06	0.01	0.02

TABLE B1d: Statistics for the 1981 northeastern meter

COMPONENT	MINIMUM	MAXIMUM	MEAN	σ
I (cm/s)				
Despiked	-37.4	21.4	-4.7	11.6
FLP	-36.0	20.5	-4.7	11.4
SLP	-16.7	12.8	-4.7	6.9
BP	-21.8	20.0	0.1	8.3
J (cm/s)				
Despiked	-21.5	24.8	-1.3	7.2
FLP	-19.6	22.1	-1.4	6.9
SLP	-8.2	3.7	-1.2	3.0
BP	-13.9	19.3	-0.1	6.0
T (°C)				
Despiked	-0.86	1.78	-0.02	0.80
FLP	-0.86	1.73	-0.02	0.80
SLP	-0.72	1.40	0.06	0.75
BP	-1.10	0.90	0.00	0.30
S (ppt)				
Despiked	33.06	34.31	33.53	0.35
FLP	33.12	34.28	33.53	0.35
SLP	33.21	34.13	33.56	0.32
BP	-0.49	0.36	0.00	0.13

Table B2: CTD cast information for June, 1981

Station Number	Time/Date GMT/June	Latitude degree N	Longitude degree W	Depth of cast(m)
1A	1256/10	45° 35.3'	48° 48.5'	76
1B	1600/11	45°. 35.3'	48° 48.5'	75
2A	1519/10	45° 31.4'	48° 43.3'	180
2B	1447/11	45° 31.7'	48° 43.5'	220
81-2	1354/6	45°. 29.0'	48° 40.0'	500
3	1544/11	45° 27.3'	48° 38.3'	300
4	1643/11	45° 21.6'	48° 36.2'	500
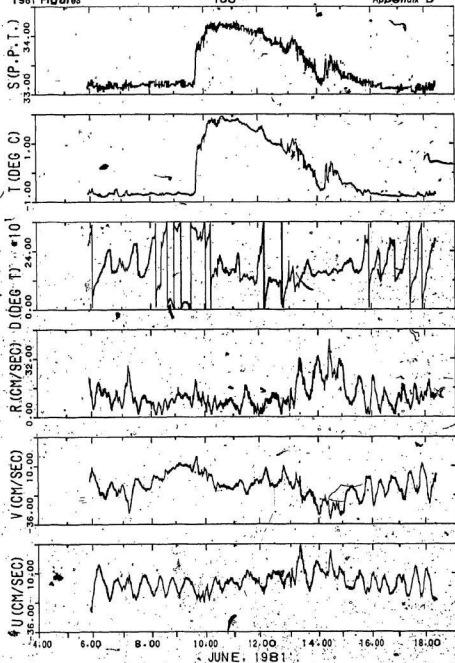
FIGURE B1: Despiked time—series of salinity, temperature, direction, rate, and the U and V velocity components: 1981 southwestern meter.
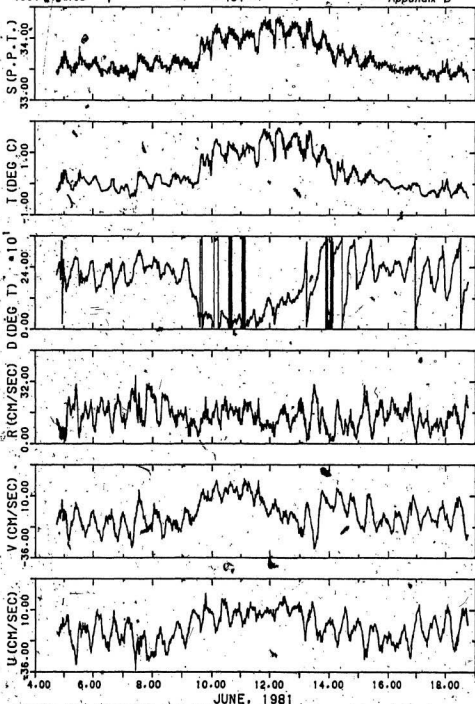
FIGURE. B2: Despiked time-series of salinity, temperature, direction, rate, and the U and V velocity components; 1981 central axis upper meter.
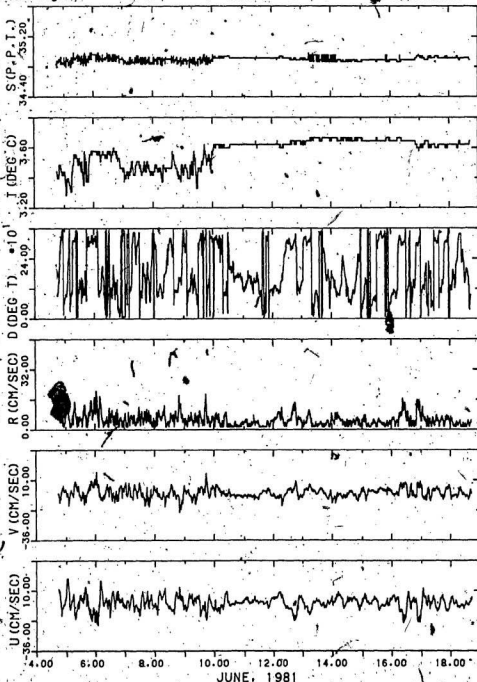
FIGURE B3: Despiked time-series of salinity, temperature, direction, rate, and the U and V velocity components; 1981 central axis lower meter.
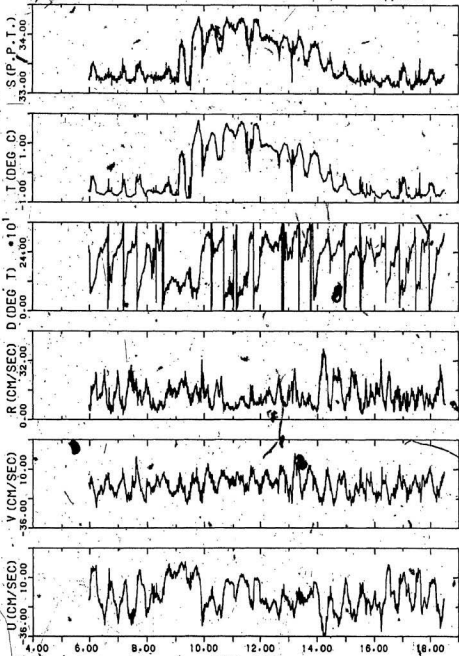
FIGURE B4: Despiked time-series of salinity, temperature, direction, rate, and the U and V velocity components; 1981 northeastern meter.
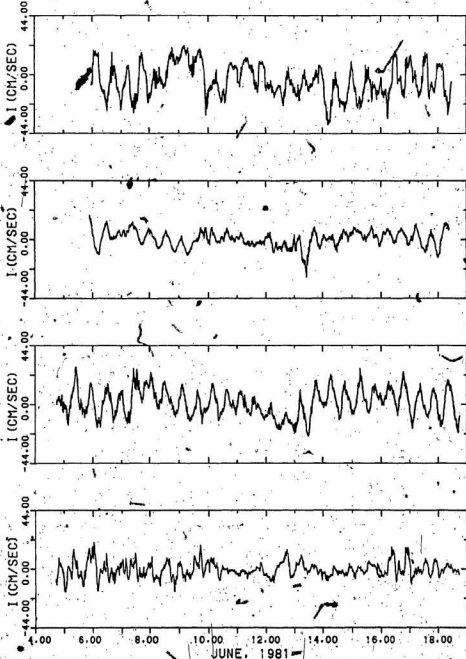
FIGURE B5: Despiked time-series of the I (cross-isobath) component of velocity for the 1981 (from top to bottom); northeastern, southwestern, central axis upper, and central axis lower meters.
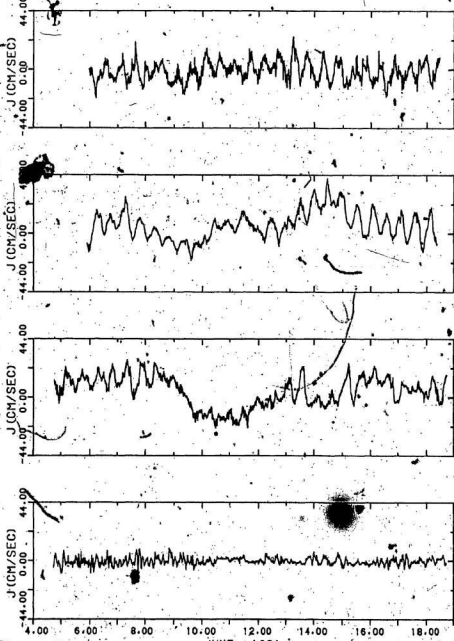
FIGURE B6: Despiked time-series of the J (along-isobath) component of velocity for the 1981 (from top to bottom): northeastern, southwestern, central axis upper, and central axis lower meters.
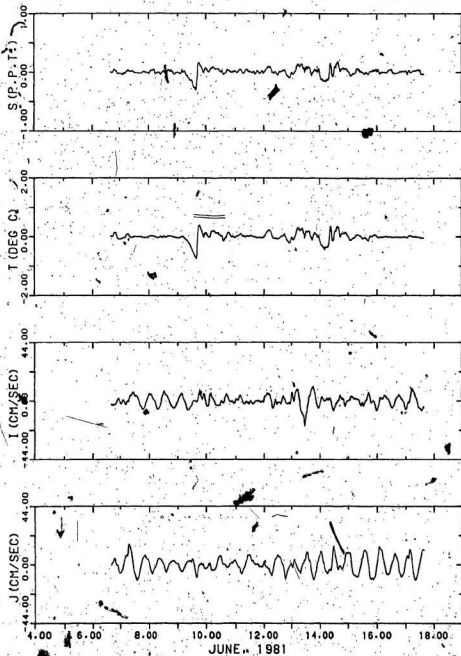
FIGURE B7: BP time-series of temperature, salinity, and the I and J velocity components; 1981 southwestern meter (mooring 81-1).
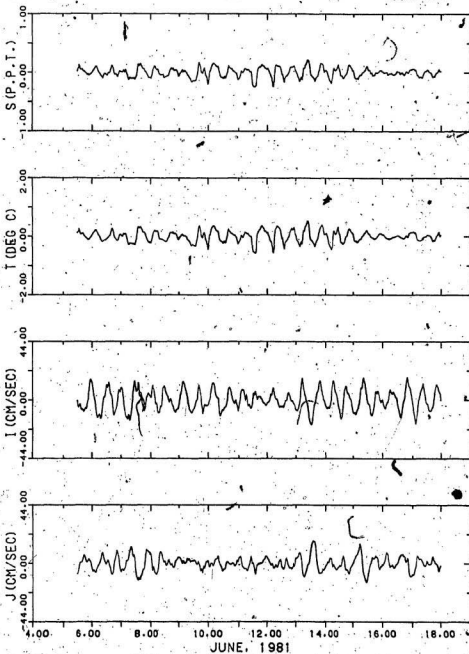
FIGURE B8: BP time-series of temperature, salinity, and the I and J velocity components; 1981 central axis upper meter (mooring 81-2).
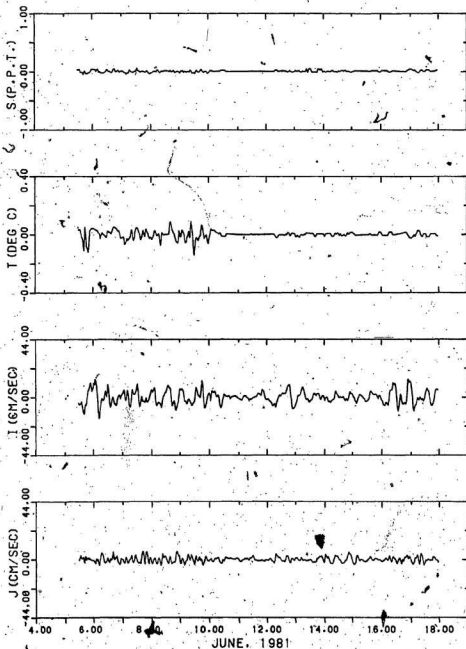
FIGURE. B9:   BP time-series of temperature, salinity, and the I and J
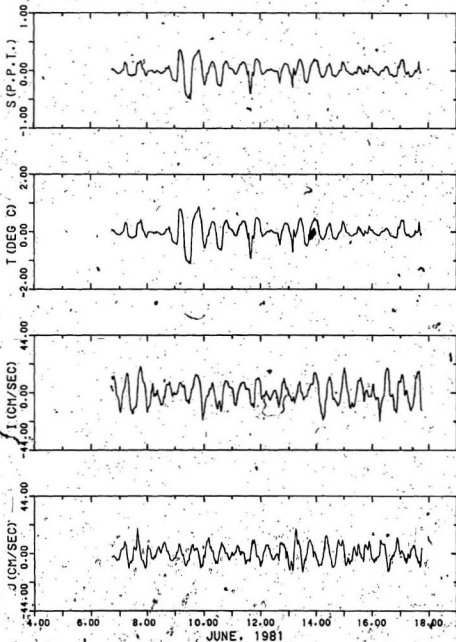velocity components; 1981 central axis lower meter (mooring 81-2).

FIGURE B10:   BP time-series of temperature, salinity, and the I and J
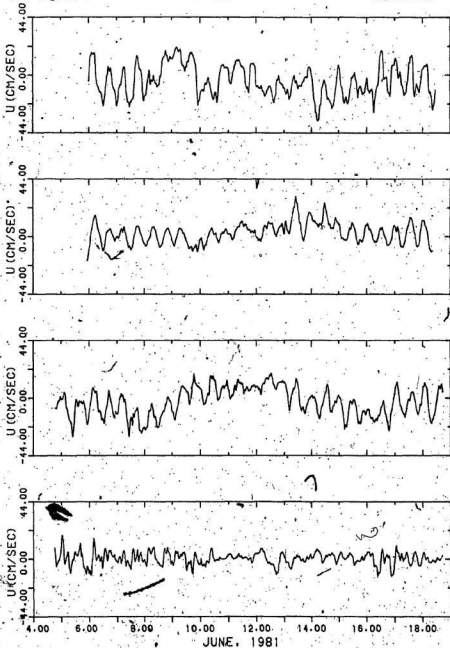velocity components; 1981 northeastern meter (mooring 85-3).

FIGURE B11: FLP time-series of the U (+, eastward) velocity component for the 1981 (from top to bottom): northeastern, southwestern, central axis upper, and central axis lower meters.
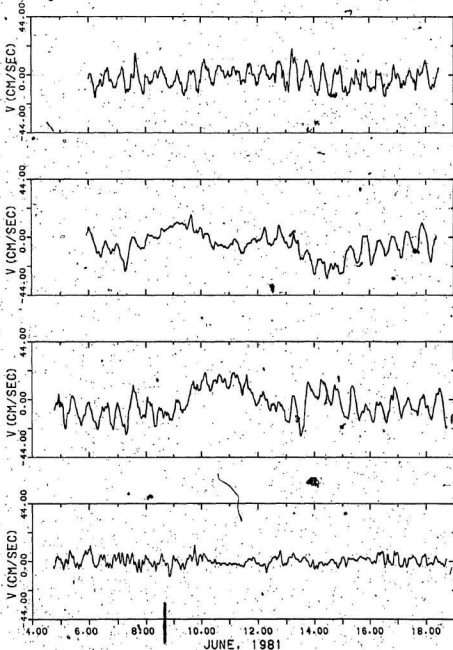
FIGURE B12: FLP time-series of the V (+ northward) velocity component for the 1981 (from top to bottom): northeastern, southwestern, central axis upper, and central axis lower meters.
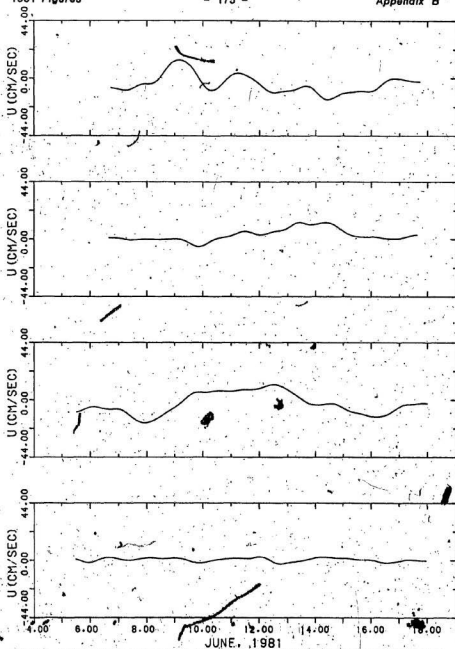
FIGURE B13: SLP time-series of the U (+ eastward) velocity component for the 1981 (from top to bottom): northeastern, southwestern, central axis upper, and central axis lower meters.
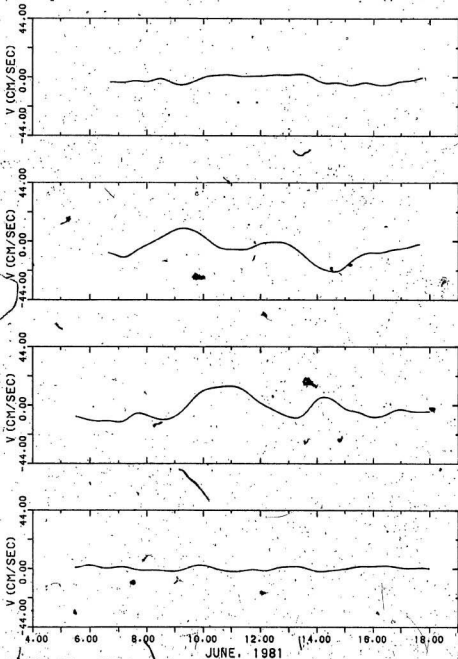
FIGURE B14: SLP time series of the V (+ northward) velocity component for the 1981 (from top to bottom): northeastern, southwestern, central axis upper, and central axis lower meters

FIGURE B15: BP time-series of the U (+ eastward) velocity component for the 1981 (from top to bottom): northeastern, southwestern, central axis upper, and central axis lower meters.

FIGURE B16: BP time-series of the V (+ northward) velocity component for the 1981 (from top to bottom): northeastern, southwestern, central axis upper, and central axis lower meters.
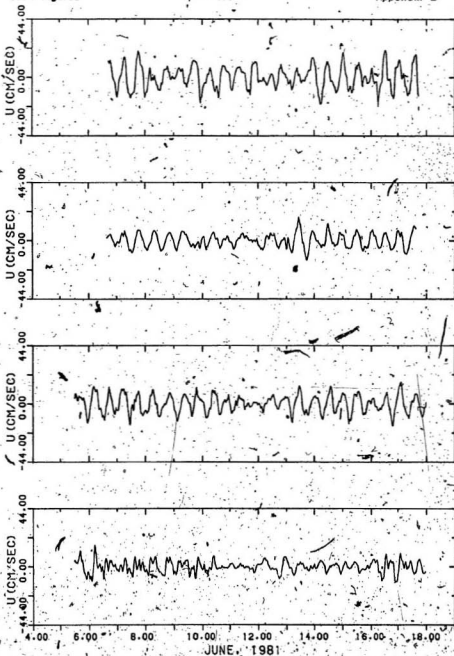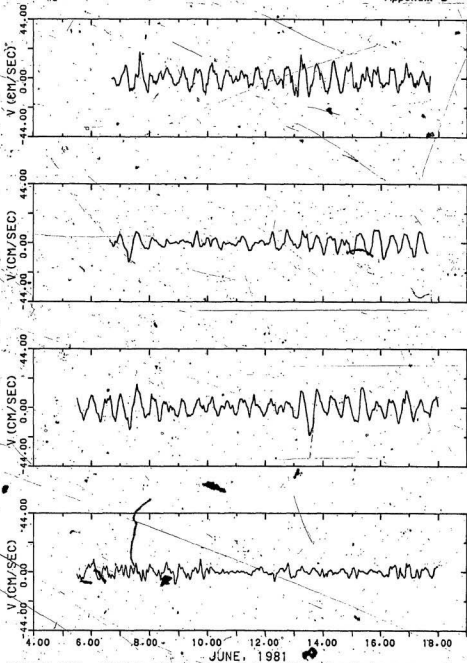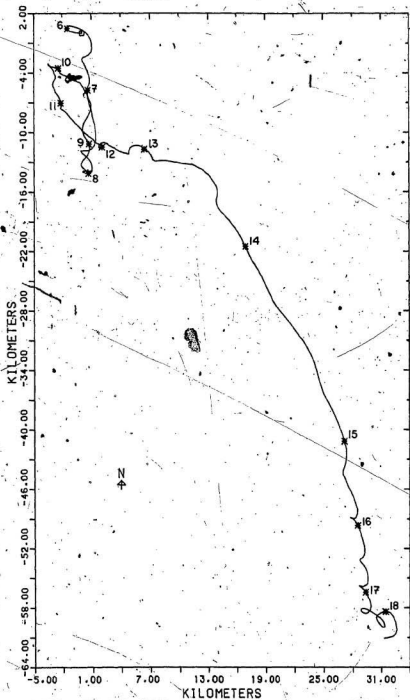
FIGURE B17: FLP PVD; 1981 southwestern meter, mooring (81-1).

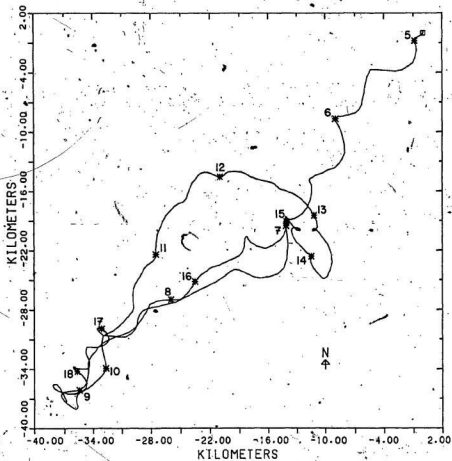FIGURE B18: FLP PVD: 1981 central axis upper meter, mooring (81-2).
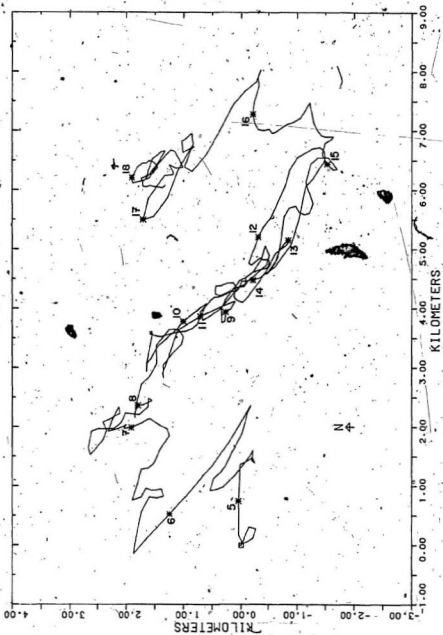
FIGURE B19: FLP PVD: 1981 central axis lower meter, mooring (81-2). Note the change in scale from Figures B17, B18 and B20.
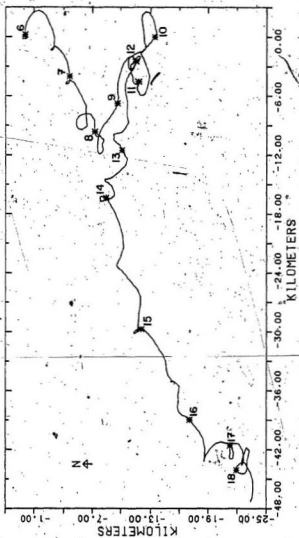
FIGURE B20: FLP PVD: 1981 northeastern meter. mooring (81-9).
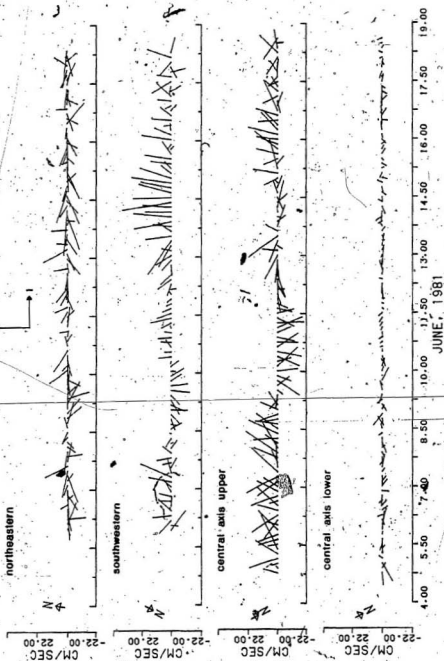
FIGURE B21: 1981 FLP I and J velocity component stick plots: sampled at 180 min.
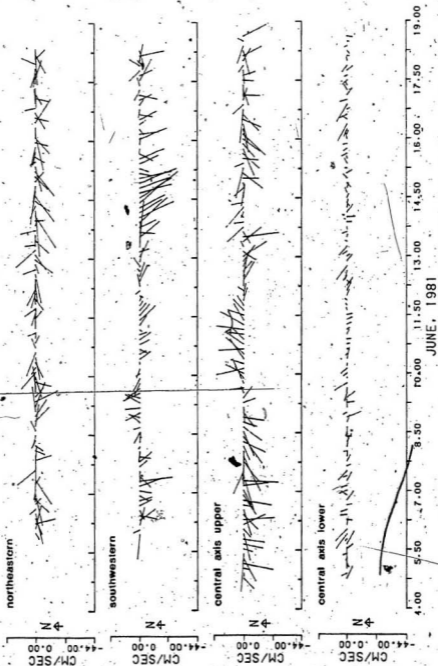
FIGURE B22: 1981 FLP U and V velocity component stick plots; sampled at 180 min.
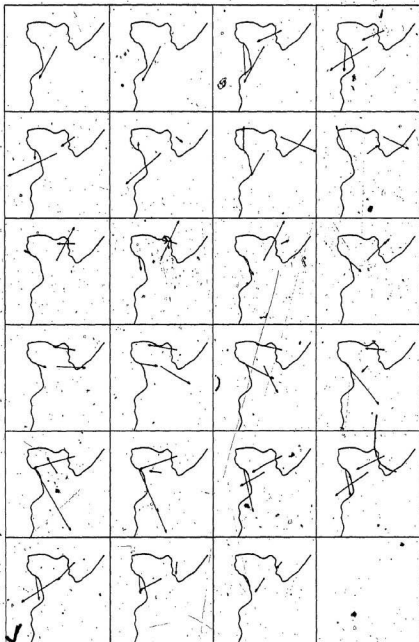
12 HR. START 23:30Z 5/06/81. 1CM=10CM/SEC
FIGURE B23: 12-hour segment-averaged vector plots for 1981
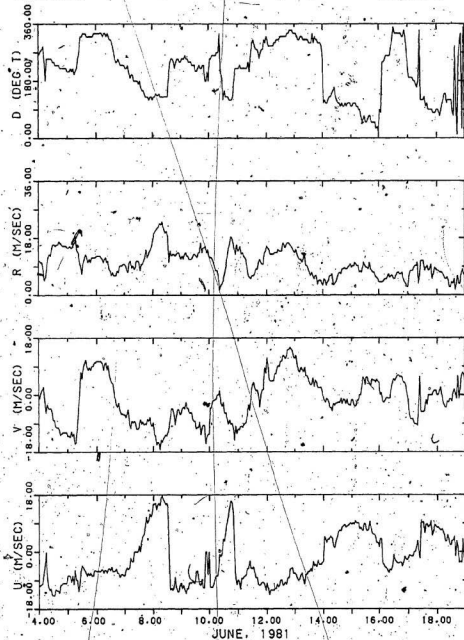
WINDS, SEDCO 706, 1981, MET. CONVENTION

FIGURE B24: Direction, rate, V (+ northerly) and U (+ easterly) components of the wind data from Hibernia for 1981.

TIDAL AMPLITUDE AT HIBERNIA (**× 2**)
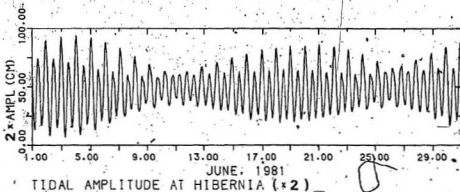
FIGURE B25: Tidal heights from Hibernia for June, 1981.

APPENDIX C   THE INTERIOR SOLUTION FOR THE LOWER LAYER

The solution to the differential equation 6.34 (reproduced below from Chapter 6) for the lower layer, cross-slope interior velocity is derived in this appendix using Jacobi poynomials and the method of Frobenius.

$$\left[1 + \frac{\hat{\eta}'_0}{hL^2}(L-y)^2\right] v'_{yy} - \left[\frac{f^2}{g'h} + \frac{2\,\eta'_0}{hL^2}\right] v' = \frac{-\tau f}{\rho D h g'} \qquad (6.34)$$

is to be rewritten using the following substitutions:

$$\theta_* = \frac{\hat{\eta}'_0}{h} \qquad (C.1)$$

$$\xi = \sqrt{a_*}\left[1 - \frac{y}{L}\right] \qquad (C.2)$$

$$\frac{d\xi}{dy} = \frac{-\sqrt{a_*}}{L} \qquad (C.3a)$$

$$\frac{d}{dy} = \frac{-\sqrt{a_*}}{L} \cdot \frac{d}{d\xi} \qquad (C.3b)$$

$$\frac{d^2}{dy^2} = \frac{a_*}{L^2} \cdot \frac{d^2}{d\xi^2} \qquad (C.3c)$$

The choice for L was made in Chapter 6 such that,

$$L = 3\,a = \frac{3}{f}\sqrt{g'\frac{hh'}{h+h}} \approx 3\frac{\sqrt{g'h}}{f} \quad \text{for} \quad h' >> h \qquad (C.4)$$

Therefore, the result for $v'(\xi)$ using (C.1) - (C.4) is,

$$\frac{a_*}{L^2}(1+\xi^2)\,v'_{\xi\xi} - \frac{f^2}{g'h}\left[1 + \frac{2}{9}a_*\right]\,v' = \frac{-\tau f}{\rho D h g'} \qquad (C.5)$$

The right hand side of equation C.5 is set = 0, and the following substitution,

$$b_x = (9 + 2a_x)$$ (C.6)

is introduced to give the homogeneous equation for the interior.

$$(T+\xi^2) v'_{in_{\xi\xi}} - \frac{b_x}{a_x} v'_{in} = 0 \qquad 0 \leqslant y \leqslant L$$ (C.7)

(Until stated otherwise, the subscript "in" is dropped with the understanding that only the interior solution is being discussed.) The following substitutions are made in (C.7).

$$x = -\xi^2$$ (C.8)

$$\frac{dx}{d\xi} = -2x$$ (C.9a)

$$\frac{d}{d\xi} = -2x \frac{d}{dx}$$ (C.9b)

$$\frac{d^2}{d\xi^2} = -2\frac{d}{dx} - 4x \frac{d^2}{dx^2}$$ (C.9c)

Consequently, (C.7) becomes,

$$x(1-x)v'_{xx} + \left[\frac{1}{2} - \frac{x}{2}\right]v'_x + \frac{b_x}{4a_x} = 0$$ (C.10)

A standard solution to (C.10) in terms of Jacobi polynomials (Hildebrand 1962, p. 142) exists when

$$\frac{b_x}{2a_x} = \frac{9}{2a_x} + 1 = n(2n-1) = N$$ (C.11)

where n and N are positive integers. Therefore,

$$a_x = \frac{\hat{\eta}_0}{h} = \frac{9}{2(N-1)}$$ (C.12)

Possible values for a_x are given below in Table C.1.

n	N	a_*
1	1	∞
2	6	0.9
3	15	0.32
4	56	0.08

TABLE C.1: Parameters determining a_*

A thickness for the upper layer of $h = 100$ m and the depth for the interface of $\hat{\eta}'_0 = 90$ m below h are suggested by the structure of the 33.4 – 33.8 ppt isohalines in the central axis salinity section (Figure 3.11) and by the 100 m depth of the shelf break which seems to be a natural choice for h. The near equivalence of $\hat{\eta}'$ and h in the 1980 central axis salinity section clearly suggests the choice of 0.9 for a_* by Table C.1. (Gill 1982, p. 404, suggests $h = 100$ for the "no-jet" model.) The following relation was determined in Chapter 6.

$$u_0 = \frac{-g'}{f} \eta'_{0_y} \qquad (6.9)$$

(6.9) is used here to relate the speed of the shelf break jet to a_*. By (6.33) of Chapter 6, $\eta'_{0_y} = -2 \dfrac{\hat{\eta}'_0}{L}\left[1 - \dfrac{y}{L}\right]$, and so, the maximum speed of the jet at $y = 0$ is.

$$u_0\,(y=0) = 2 \frac{g'\hat{\eta}'_0}{f\,L} \qquad (C.13)$$

By substituting $L = 3 \times \dfrac{\sqrt{g'h}}{f}$ (e.g. equation C.4), a final result is obtained

$$u_0\,(y=0) = \frac{2}{3}\sqrt{g'h}\,\frac{\hat{\eta}'_0}{h} = \frac{2}{3}\sqrt{g'h}\,a_* \qquad (C.14)$$

With $h = 10^5$ cm, $\hat{\eta}'_0 = 9 \times 10^4$ cm and $g' = 0.49$ cm s^{-2}. (g' is given

by equation 6.7 with $\Delta\rho = 5 \times 10^{-4}$ by Table 5.1), then, $u_0'(y=0) = 42$ cm s^{-1}. Therefore, the value of 46 cm s^{-1} which was determined by geostrophic calculations in section 3.6 of Chapter 3 for the velocity axis of the Labrador Current agrees reasonably well with $u_0(y=0)$ calculated here for $a_* = 0.9$.

Returning now to equation C.10, the solution for n = 2 $\left[\dfrac{b_*}{a_*} = 6\right]$ is the second order Jacobi polynomial given by (Hildebrand 1962, p. 184).

$$J_{n=2}\left[\frac{1}{2}, \frac{-1}{2}; -x\right] = 1 + 6x + 5x^2 \qquad |x| < 1 \qquad (C.15a)$$

or, in terms of y by (C.2) and (C.8) as,

$$J_2\left[\frac{1}{2}, \frac{-1}{2}; -a_*\left[1 - \frac{y}{L}\right]^2\right] = 1 - 6a_*\left[1 - \frac{y}{L}\right]^2 + 5a_*{}^2\left[1 - \frac{y}{L}\right]^4 \quad (C.15b)$$

$$0 < y < L \qquad \text{and} \qquad a_* = 0.9$$

However, (C.15) is only one solution to (C.7). Now that the value of $\dfrac{b_*}{a_*}$ is known, (C.7) may be solved by the method of Frobenius (e.g. Hildebrand 1962, p. 140 - 141) and (C.15) recovered as one of two independent solutions. Using values from above, (C.7) is written as

$$(\tfrac{1}{3} + \xi^2) \, v'_{\xi\xi} + \frac{1}{\xi^2}(-12\xi^2) \, v' = 0 \qquad (C.16)$$

The assumption that $v' = \displaystyle\sum_{k=0}^{\infty} A_k \, \xi^{k+s}$ is introduced into the last relation resulting in the following condition.

$$
\begin{aligned}
0 = &\; s(s-1)A_0 \, \xi^{s-2} + s(s+1)A_1 \, \xi^{s-1} \\
&+ \left[(s+1)(s+2)A_2 - 12A_0\right] \xi^{s-1} \\
&+ \left[(s+k)(s-k+1)A_k + \left[(s-2+k)(s-3+k) - 12\right]A_{k-2}\right] \xi^{s+k-2}
\end{aligned}
\qquad (C.17)
$$

Recursion relations for the A's are found for $s = 0$ by setting the coefficients to each of the terms in ξ equal to zero. A_0 and A_1 are set equal to unity. The A_k for $k > 6$ and k even go to zero. There are two independent solutions depending on whether k is even or odd. These two solutions are,

$$v'_1 = A_0 + A_2 \xi^2 + A_4 \xi^4 \qquad\qquad (C.18a)$$

and

$$v'_2 = A_1 \xi + A_3 \xi^3 + A_5 \xi^5 + A_7 \xi^7 + \ldots \qquad (C.18b)$$

The polynomial coefficients A_n have been determined, and are given below in Table C.2a up to $n = 15$, for n odd. The values; $A_0 = 1$, $A_2 = 6$, $A_4 = 5$, and $A_{n > 6} = 0$ (for even n), are the same as the coefficients of $J_2 \left[\frac{1}{2}, \frac{-1}{2}, -x \right]$.

The fact that $\lim\limits_{n \to \infty} \xi < \lim\limits_{n \to \infty} \left[a_n \right]^{\frac{n}{2}} = 0$ insures that the nth order term of the polynomial converges to zero. A maximum error of 0.5% is introduced by setting the coefficients $> A_{11} = 0$ (Table C.2a). Also shown in Table C.2a and b are the first and second derivatives of the polynomial (not including constant factors of L). Note that both these series converge as well.

TABLE C.2a: The coefficients A_n, the sum of terms and the sum of the first derivative terms for equation C.18b at $y = 0$ ($\xi = 0.9$).

n	A_n	$\sum\limits_{n=1} A_n\, \xi^n\,(y=0)$	$-\sum\limits_{n=2} A_n\, n\, \sqrt{a_x}\ \xi^{n-1}\,(y=0)$
1	1	0.94868	-0.94868
3	2	2.6563	-6.07157
5	0.6	3.1174	-8.37687
7	-0.11429	3.0383	-7.82358
9	0.047619	3.0680	-8.09034
11	-0.025974	3.0534	-7.93028
13	0.016317	3.0616	-8.03723
15	-0.011189	3.0566	-7.96107

TABLE C.2b: The the sum of the second derivative terms for equation C.16b at $y = 0$ ($\xi = 0.9$).

n	A_n	$\sum\limits_{n=3} A_n\, n\,(n-1)\, a_x\, \xi^{n-2}\,(y=0)$
3	2	10.246
5	0.6	19.467
7	-0.11429	15.778
9	0.047619	17.912
11	-0.025974	16.312
13	0.016317	17.595
15	-0.011189	16.529

Now, the particular solution for the interior is found simply by taking $Y'_{\xi\xi} = 0$ in (C.5),

$$Y'_p = \frac{\tau}{\rho f D} \frac{1}{(1 + 2a_x/9)} \qquad 0 \leq y \leq L \qquad (C.19)$$

is the particular solution.

The solution of (C.5) is a combination of equations C.18 and C.19 with $a_x = 0.9$ and with the A_n truncated at $n = 9$ as given by Table C.2a.

$$v'_{in} = Bv'_1 + Cv'_2 + v'_p$$

or,

$$v'_{in} = B(1 + 6\xi^2 + 5\xi^4) \tag{C.20}$$

$$+ C(\xi + 2\xi^3 + 0.6\xi^5 - 0.11429\xi^7 + 0.047619\xi^9) + \frac{5}{6} \frac{\tau}{\rho f D}$$

for $0 \leqslant y$, where A, B, and C are integration constants. These constants will now be determined.

Since $v'_{in} = 0$ and $\xi = \sqrt{0.9}$ at $y = 0$.

$$v'_{in}(y=0) = 0 = 10.45B + 3.06797C + \frac{5}{6} \frac{\tau}{\rho f D} \tag{C.21}$$

The exterior solution was found earlier in Chapter 6 and is rewritten here for convenience.

$$v'_{ex} = Ae^{-y/a} + \frac{\tau}{\rho f D} \tag{6.36}$$

At $y = L = 3a$, (6.36) is,

$$v'_{ex} = Ae^{-3} + \frac{\tau}{\rho f D} \tag{C.22}$$

Therefore, at $y = L$, $v'_{in} = B + \frac{5}{6} \frac{\tau}{\rho f D}$ by (C.20) matches (C.22), and

$$B = Ae^{-3} + \frac{1}{6} \frac{\tau}{\rho f D} \tag{C.23}$$

The y derivatives of v'_{in} and v'_{ex} must be continuous because η' is also continuous and $\eta'_t = \frac{\partial v'}{\partial y}$ by equations 6.18 and 6.21 of Chapter 6. Setting $\frac{dv'_{in}}{dy} = \frac{dv'_{ex}}{dy}$ at $y = L$, equations 6.36 and C.20 give.

$$\frac{\sqrt{a_a}}{L} C = \frac{A}{a} e^{-3}$$

or, since $L = 3a$,

$$C = \frac{3A}{\sqrt{a_a}} e^{-3} \tag{C.24}$$

Equation C.23 for B and (C.24) for C are substituted in (C.21) to obtain.

$$A = -2.586 \frac{\tau}{\rho f D} \qquad (C.25)$$

From (C.23) and (C.25),

$$B = \frac{0.2335}{6} \frac{\tau}{\rho f D} \qquad (C.26)$$

From equation C.24 (or equation C.21),

$$C = \frac{-2.424}{6} \frac{\tau}{\rho f D} \qquad (C.27)$$

Therefore, (6.36) and (C.25) yield the exterior solution, which is.

$$v'_{ex} = \frac{\tau}{\rho f D} \left[1 - 2.586 e^{-y/a} \right] \qquad y > L \qquad (C.28)$$

and by (C.20), (C.26) and (C.27) the interior solution is.

$$v'_{in} = \frac{\tau}{\rho f D 6} \left[0.2335 (1 + 6\xi^2 + 5\xi^4) \right.$$

$$\left. - 2.424 (\xi + 2\xi^3 + 0.6\xi^5 - 0.11429\xi^7 + 0.047619\xi^9) + 5 \right] \qquad (C.29)$$

where $\xi = \sqrt{a_*} \left[1 - \frac{y}{L} \right]$. $L = 3a$. and $a = \sqrt{\frac{a'h}{f}}$.